Torsional and Flexural Control of Sandwich Composite Beams with Piezoelectric Actuators

by

Ayako Koike

Thesis submitted to the Faculty of the

Virginia Polytechnic Institute and State University

in partial fulfillment of the requirements for the degree of

Master of Science

in

Aerospace Engineering

Approved:

Eric. R. Johnson, Co-chairman

Rakesh. K. Kapania, Co-chairman

Zaffir. Chaudhry

Raphael. T. Haftka

September, 1994
Blacksburg, Virginia

c. 2

LD
S655
V855
1994
K655
c. 2

Torsional and Flexural Control of Sandwich Composite Beams with Piezoelectric Actuators

by
Ayako Koike
Co-chairmen: Eric R. Johnson and Rakesh K. Kapania
Aerospace and Ocean Engineering

(ABSTRACT)

A mathematically one-dimensional model was developed to predict the static response of composite sandwich beams subjected to loads induced by piezoelectric (PZT) actuators. The model was derived using Reddy's (1984) displacement field for a laminated plate which consisits of cubic variation of the in-plane displacement through the thickness.

In this model, beam deformations include extension, bending, transverse shear, St. Venant torsion, and torsion due to warping of the cross section out of its plane. The PZT actuators can be configurated to induce a bimoment, resulting in twist of the beam through the warping of the cross section. Hence directionally attached PZT (DAP) actuator elements, which cause twist by inducing tensile and compressive strains at 45° to the longitudinal axis of the beams, are not necessary to actuate twist. For an aluminum beam example, it is shown that the PZT bimoment control produced about 2.7 times more twist than the conventional DAP control.

Acknowledgments

I would like to thank my co-advisors Dr. Eric R. Johnson and Dr. Rakesh K. Kapania for their advice and guidance through out my graduate study at Virginia Tech. Dr. Johnson, thank you for your exceptional patience and your dedication toward making sure students really understand the concepts. Your careful review of this manuscript was invaluable and I appreciate it greatly. I would also like to thank my committee members, Dr. Zaffir Chaurdhry and Dr. Raphael T. Haftka, for their positive inputs and providing their valuable time to help improving my thesis. Dr. Chaudhry, I also thank you for your discussions and help with smart materials.

My appreciation to Evangelos Hytopoulos for all his technical help and the extraordinary support toward my academic career. His drive to make himself a better researcher and a valuable person has set a great example for me. Marco Lombardi, I thank you for your help with *NASTRAN*. Also, I thank you for all the encouragement you have given me to get through those days and showing me the excellent model of mankind. Yes, I realized that "It does not always end like this." Alessandra Sermoneta, thank you for being a good friend and a good influence. I will see you in Rome. Amy Gefferth, I send you my special gratitude for your great friendship and all the emotional support you have given me over all the years, especially during my crisis. Someday, I hope to reach the strength you have.

Eric Flint, thank you for making the last part of my graduate school life so much more fun. Without your supports and those vacations, I would have been demolished by the stresses. I sincerely appreciate all the encouragement you have given me through out the course of finishing up my thesis. My very special thanks goes to you for believing in my ability and never doubting it.

Finally, I would like to thank my parents, Yasuyoshi and Junko Koike. Without their consistent love and support, I would have not been where I am now. Even though I have been far away for a long time, many terrific qualities I have learned over the years from you two have been always with me. This thesis is dedicated to you both.

Table of Contents

Chapter 1: Introduction 1
1.1 Composite and intelligent materials 1
1.2 Sandwich structures 3
1.2.1 Analytical modeling 4
1.2.2 Higher-order transverse shear deformation theory 6
1.2.3 Finite element modeling 7
1.3 Piezoelectric ceramics 8
1.3.1 Piezoelectric material 8
1.3.2 Modeling of structures with piezoelectric ceramics 10
1.3.3 Finite element modeling of structures with piezoelectric ceramic 11
1.3.4 Torsional control by piezoelectric ceramics 12
1.4 Objectives and approaches 13
1.5 Outline 14

Chapter 2: Higher-order transverse shear deformation plate theory 15
2.1 Approximate displacements and conjugate forces 15
2.2 Electroelastic constitutive equation 21
2.3 Laminate constitutive equations 25
2.4 The configurations of PZT and induced forces 28

Chapter 3: Beam Theory 30
3.1 Approximate displacement and conjugate forces 31
3.2 Constitutive equation 35
3.3 Stiffness matrix 38
3.4 Induced force by PZT 43
3.5 Governing equations and boundary conditions 45

Chapter 4: Finite element formulations 48

4.1 Equation of motion....49
4.2 Modeling of bonded PZT....54
4.3 Minimum length of the PZT patch....57
4.4 Computer code - SANDB....59

Chapter 5: Results and discussions....61
5.1 Verifications of structural model....61
5.1.1 Comparison with exact solution....61
5.1.1.1 Axial displacement....62
5.1.1.2 Transverse deflection....62
5.1.1.3 Angle of twist due to a torque....63
5.1.2 Angle of twist by bending & torsional coupling configuration....64
5.1.2.1 I-DEAS....64
5.1.2.2 Comparison....65
5.2 Static analysis of a sandwich beam....66
5.2.1 Simply supported beam....66
5.2.1.1 NASTRAN Model....67
5.2.1.2 Sharma and Rao solution....68
5.2.1.3 Holt and Webber solution....68
5.2.1.4 Comparison between the solutions....69
5.2.1.5 A cantilever sandwich beam....70
5.2.1.6 A sandwich beam with transversely flexible core....72
5.3 Verifications of theory with PZT....73
5.3.1 Transverse Deflection....73
5.3.1.1 DAISA....74
5.3.1.2 Comparison....74
5.3.2 Axial displacement....75
5.3.2.1 Robbins and Reddy's model....76
5.3.2.2 Comparison....76
5.3.3 Angle of twist induced by bimoment....77
5.3.3.1 NASTRAN model....78
5.3.3.2 Comparison....78
5.4 Convergence study....78
5.4.1 Induced bending deformation....80
5.4.2 Induced bimoment deformation....81
5.4.3 Distance between distributed PZT Patches....84
5.5 Torsional problems....88
5.5.1 Bimoment resistance....89

5.5.1.1 Different facing materials and thickness 89
5.5.1.2 Orientation of the fibers 91
5.5.1.3 Decay length 92
5.5.1.4 Effectiveness of control by bimoment 94

Chapter 6: Concluding remarks 96
6.1 Summary 96
6.2 Discussions and conclusions 97
6.2.1 Numerical study 97
6.2.1.1 Verification without piezoelectric effects 97
6.2.1.2 Effectiveness of using the higher-order theory for sandwich beam 98
6.2.1.3 Verification with piezoelectric effects 98
6.2.1.4 Convergence study 99
6.2.1.5 Torsional problem 99
6.2.1.6 Bimoment torsional control 100
6.2.2 Conclusions 100
6.3 Future work 101

References 102

Vitas 106

List of Figures

FIg. 1.1 Sandwich beam with piezoelectric actuators. 2
Fig. 1.2 Configuration of a simple sandwich structure. 3
Fig. 1.3 Electro-mechanical response of typical PZT[23] 9
FIg. 2.1 The coordinate system of a plate. 16
Fig. 2.2 Plate resultants in Reddy's[15] theory. 21
Fig. 2.3 The coordinate system of a PZT patch. 21
Fig. 2.4 A laminate with PZT actuators. 25
Fig. 2.5 The coordinate system of a plate and a PZT patch in this study. 28
Fig. 2.6 The coordinate system of a plate and an off axis PZT patch. 28
FIg. 3.1 The coordinate system and dimensions of a beam. 30
Fig. 3.2 Resultant forces and moments of a beam. 34
Fig. 3.3 The cross-section of a beam which induce the axial force only. 43
Fig. 3.4 The cross-section of a beam which induces the bending only. 44
Fig. 3.5 The cross-section of a beam which induces the bimoment only. 44
Fig. 3.6 The prescribed tractions, p_x, p_y, and p_z on a beam. 45
FIg. 4.1 The coordinate system of a beam element. 48
Fig. 4.2 Piezoelectric and substructure strains for various value of G.[24] 55
Fig. 4.3 Comparison of the transverse displacements. 56
Fig. 4.4 A reinforcement configuration and shear transfer in the adhesive 58
Fig. 4.5 The flow chart of SANDB. 60
FIg. 5.1 The dimension and material properties of an isotropic cantilever beam. 61
Fig. 5.2 I-DEAS model of the beam 65
Fig. 5.3 The coordinate system and geometry of a simply supported sandwich beam. 66
Fig. 5.4 The NASTRAN model of the beam. 67
Fig. 5.5 Comparison of the transverse deflection of the beam for case 1: soft core 69

Fig. 5.6 Comparison of the transverse deflection of the beam for case 2: stiff core. 70
Fig. 5.7 The coordinate system of a cantilever beam. 71
Fig. 5.8 The coordinate system of the beam with transversely flexible core. 72
Fig. 5.9 The beam with PZT actuators. 73
Fig. 5.10 The dimension & the coordinate system of the beam from Robbin and Reddy.[28] 75
Fig. 5.11 An aluminum beam with four PZT actuators. 77
Fig. 5.12 The beam dimensions and different meshing. 79
Fig. 5.13 Distribution of the transverse deflection of the beam subject to induced bending 80
Fig. 5.14 Distribution of the angle of twist for the beam subject to induced bimoment. 81
Fig. 5.15 Distribution of the derivative of the twist angle for the beam subject to induced bimoment. 82
Fig. 5.16 Distribution of the angle of twist for the beam subject to induced bimoment. 83
Fig. 5.17 Distribution of the derivative of the twist angle for the beam subject to induced bimoment. 84
Fig. 5.18 Comparison of angle of twists for a beam with distributed actuators 85
Fig. 5.19 Comparison of t' for a beam with distributed actuators. 86
Fig. 5.20 Comparison of angle of twists for a beam with distributed actuators 87
Fig. 5.21 Comparison of t' a beam with distributed actuators. 88
Fig. 5.22 The dimension of a sandwich beam. 89
Fig. 5.23 Bimoment resistance vs. fiber orientation in facings. 91
Fig. 5.24 Decay of bimoment. 92
Fig. 5.25 Close up of Fig. 5.23. 93
Fig. 5.26 A cantilever beam of Park et al. 94
Fig. 5.27 The configurations of PZT patches for SANDB. 95

List of Tables

Table 1.1 Definition of the facing thickness by Allen. 6
Table 4.1 Typical material values.[41] 58
Table 5.1 Axial displacement verification. 62
Table 5.2 Transverse deflection verification. 62
Table 5.3 Twist of angle comparison. 63
Table 5.4 The material properties and the dimensions of the beam. 64
Table 5.5 Comparison of transverse deflection and the angle of twist. 65
Table 5.6 The material properties and dimension of the beam. 66
Table 5.7 The dimension of the cantilever beam. 71
Table 5.8 The tip deflection of the cantilever beam (m) subjected to self weight 71
Table 5.9 Material properties and beam dimensions fro Ref. 14. 72
Table 5.10 Comparison of mid-span beam displacement from SANDB and Ref. 14 73
Table 5.11 Material properties and dimensions of PZT beam examples 74
Table 5.12 Tip deflection comparison for case 1. 74
Table 5.13 Tip deflection comparison for case 2. 75
Table 5.14 Material properties and dimensions for the beam from Ref. 28 76
Table 5.15 Comparison of nondimensionalized displacement from Ref. 28 and SANDB 77
Table 5.16 Angle of twist from SANDB and NASTRAN for bimoment actuation 78
Table 5.17 The material properties of a sandwich beam. 90
Table 5.18 Bimoment resistance of sandwich composite beams with foam core 90
Table 5.19 The dimension of DAP elements. 94
Table 5.20 Comparison between bimoment control and DAP element control. 95

1. Introduction

1.1 Composite and intelligent materials

The selection of the materials is one of the most important steps in the construction of any structure. The choice has been broadened greatly with the introduction of advanced fiber-reinforced resin composite materials. To quote Jones[1],

> *"The advent of advanced fiber-reinforced composite materials has been called the biggest technical revolution since the jet engine."*

These materials possess great advantages over traditional materials in this modern society where there are needs for stronger materials with less weight such as in aerospace structures. The fiber-reinforced composite materials can be tailored to suit the loading condition of the structure by laminating them in various orientations. In this way, a minimum amount of material is used to meet stiffness requirements.

One of the recent advances in the materials field is the development of the intelligent materials, which utilize the interaction between mechanical and some other fields, electric, magnetic, and so on. Intelligent materials have been the subject of great interest because

of their abilities to control and sense the response of structures. A number of intelligent material systems are available: piezoelectric, magnetostrictive, electrostrictive, shape memory alloys, conductive polymers, and others. These materials, as actuators, are capable of inducing strains in the structures by certain external stimuli. The desire to reduce structural weight led to the advancement of these material, which ultimately can replace the controlling devices. The application of intelligent materials to the advanced fiber-reinforced composite structures could improve the performance of aircraft and space vehicles.

The aim of this study is to use an intelligent material to control the deformation of a laminated composite structure. In particular, control of a sandwich beam by piezoelectric actuators bonded to the external surface of the beam as shown in Fig. 1.1 is considered. In the remaining sections of this chapter, sandwich beams (Section 1.2) and piezoelectric actuators (Section 1.3) are discussed along with some pertinent literature review. Objectives for this study are presented in Section 1.4.

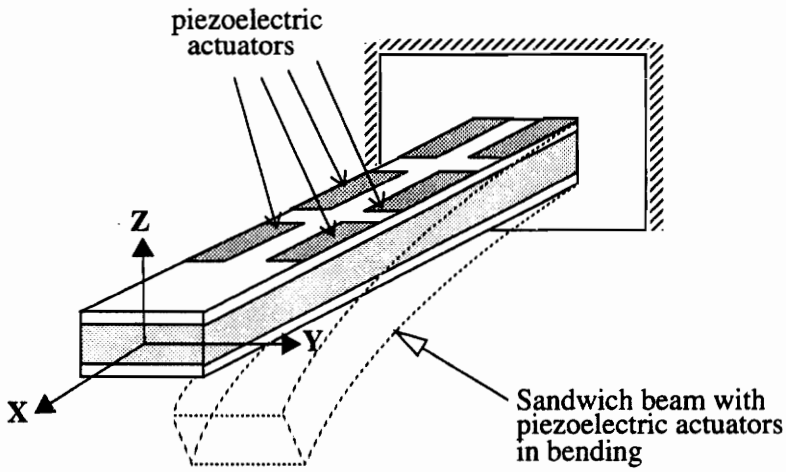

Fig. 1.1 Sandwich beam with piezoelectric actuators.

1.2 Sandwich structures

One of the important class of laminated structures is the sandwich configuration. The simplest form of a sandwich structure consists of two thin and strong facings usually of high density and a low density core which separates the facings. (See Fig. 1.2) The core is thicker and more flexible than the outer layers of facings. Typically, various types and shapes of honeycombs or foam cores are used. The main advantage of this configuration is that the core separates the two stiff facings and thereby increases the bending stiffness

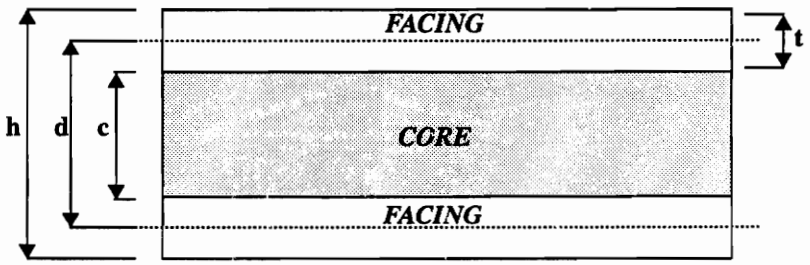

Fig. 1.2 Configuration of a simple sandwich structure.

of the structure without much weight penalty. There are some disadvantages of the sandwich construction, the main one being that the core material characteristics can become nonuniform under hygrothermal environment.

Sandwich configurations using traditional materials have been used in aerospace and other branches of engineering for a long time. The Second World War aircraft named "Mosquito" is known as the first to make extensive use of sandwich panels. The advent of advanced composite materials and their application in sandwich construction contributed to an even greater reduction in the structural weight. Radomes are made from glass-reinforced plastics facings and core so that radar waves can penetrate the dome. The Voyager aircraft, which flew around the world without refueling, consists extensively of sandwich

structures.[2] Its vertical stabilizer is made of nomex aramid honeycomb core and facings of woven fiberglass impregnated with epoxy. The wings and bulkheads are nomex aramid honeycomb core and facings of two-ply graphite tape. Polymide/glass honeycomb core and ceramic cloth impregnated with polymide resin are used in the firewalls. The fuselage is made of nomex aramid honeycomb core and woven aramid fiber or woven graphite fiber impregnated with epoxy as facings. Similarly, engine cowlings are made of nomex aramid honeycomb core with facings of woven aramid fiber impregnated with self-adhesive epoxy resin system.

1.2.1 Analytical modeling

The modeling approach taken hinges on whether the effect of the core stiffness is significant or negligible. Allen[3] has summarized the analysis of sandwich structures through the 1960's. He presented a guideline to determine the significance of the core stiffness. According to Allen, core stiffness does not need to be included in the analysis if

$$\frac{E_f}{E_c}\frac{t}{c}\left(\frac{d}{c}\right)^2 > 16.7 \tag{1.1}$$

where E_f is the Young's moduli of the facings, E_c is the Young's moduli of the core, and the other variables are shown in Fig. 1.2. The critical variables according to Eq. (1.1) are the ratio of stiffness of the facings to the core, and ratio of the thickness of the facings to the core. In many studies the stiffness of the core is considered to be negligible, Implying the core is much softer and much thicker than the facing.

Cheng[6] treated the facings as membranes thus ignoring their transverse shear stiffness in the analysis of sandwich plates with composite facings and an orthotropic honeycomb core. The core was treated as a shear carrying layer while applying the Euler-Bernoulli

beam theory to the outer layers by Di Taranto.[7] These analysis have their limitations since they ignored some stiffness effects. Rao[8] pointed out that the bending and extensional stiffness of the core can not be ignored for the thick or stiff core and unsymmetrical sandwich beams. In his analysis, the metallic facings were treated as Bernoulli-Euler beams and the core was treated as a Timoshenko beam. The errors in maximum deflections were found to be up to 17% if the bending and extensional stiffnesses of the core were ignored. This results in large errors in the stresses.

Sharma and Rao[9] solved deflections and stresses of sandwich beams for different boundary conditions. The weak core assumption was employed in this analysis, thus the extensional and bending stiffnesses of the core were neglected. The facings bend according to Euler hypothesis in their analysis. The analysis showed the significant effect of riveting of an edge of the soft cored sandwich beam. Contrasting to this finding, the effect of riveting of an edge was found to be negligible for stiff cored sandwich beams. Sandwich structures with composite facings were investigated by Holt and Webber.[10] In their analysis, the face plates are treated as membranes and the thin shell equations of Sanders[11] and Koiter[12] are applied. The thick sandwich shell equations in Webber's work[13] are used for the core. Holt and Webber[10] provided analytical solutions that can be used for evaluation of finite element models. The sandwich beams with transversely flexible core were analyzed by Frostig and Baruch.[14] This analysis focused on the localized effects under the general loadings. The model was based on the superposition of two beam substructures, one with a core which resists shear and transverse normal stresses and the other with vertically flexible core. Thickness stretching of the core was allowed to be changed and the plane section did not remain plane. Thus the higher order deformation effects of the core were considered, and the peeling and the shear stresses at the interfaces of the core and facings can be computed in their analysis.

Allen[3] categorized the thickness of the facings as . This categorization has taken to the

consideration when thick core or thin core sandwich beams are mentioned in this writing. Under bending, the sandwich structure is the most efficient when the weight Allen's definition of the facing thickness is

Table 1.1 Definition of the facing thickness by Allen.

Definition	Cut-off line
Very Thin facings	$(d / t) > 100$
Thin facings	$100 > (d / t) > 5.77$
Thick facings	$(d / t) < 5.77$

of the core is about the same as the total weight of the facings. Under buckling, it is the most efficient when the weight of the core is about twice of the total of the facings. These derivation can be found in Peery[4]. The outline of the basic design formulas for optimum design of sandwich structures for the least weight and the cost can be found in Johnson and Sims[5]. In order to achieve further weight reduction, the core must be thicker and the facings must be thinner while keeping the high bending stiffness. Thus, the analysis of thick core sandwich composite material becomes essential.

1.2.2 Higher-order transverse shear deformation theory

Higher order shear deformation theory for laminated plates has been introduced by Reddy[15]. He derived the theory based on a cubic distribution through the thickness of the in-plane displacement field. This higher shear deformation theory takes account of the parabolic distribution of the transverse shear strain through the thickness, thus it is claimed that there is no need for a shear correction factor. This is an advantage over the first-order shear deformation theory, which usually requires shear correction factors depending on the beam geometry. Obst[16] used the displacement field of Reddy[15] to ana-

lyze laminated beams. He reduced the two-dimensional theory of plates to a one-dimensional theory of beams by equating the lateral forces to zero after finding the laminate resultant forces for the two-dimensional case. With this method, the lateral strains and curvatures are retained in terms of the axial and transverse strains and curvatures. Thus, the shear-stretch and bend-twist couplings remains in the analysis but the torsional analysis of this model is limited.

"A layer wise higher-order zig-zag model" was applied to the thick cored unsymmetrical sandwich beams by Lee et al[17]. This model used a cubic variation in the thickness coordinate of the axial displacements in each layer, and the transverse shear stress distribution through the thickness of the beam was parabolic. This model was compared with Rao[8] and Di Sciuva[18] and found to predict quite different axial displacement and bending stress distributions through the thickness. However, verification by comparison with an exact elasticity solution was not done in this analysis.

1.2.3 Finite element modeling

Kant et al.[19] developed a finite element model for the transient analysis of sandwich plates using a refined theory. Nine-noded Lagrangian elements were used in this model. The superiority of using higher order theory was revealed for sandwich plates in their study. The flexural behavior of a rotating sandwich beams was studied by Ko.[20] The governing equations were derived from the variational principle and the numerically analyzed. Timoshenko beam model and Euler-Bernoulli beam model were compared in this study.

An extensive overview of the finite element models of sandwich plates can be found in Ha.[21] According to Ha[21], fields which have not gotten much attention in the numerical scheme are local instability, delamination caused by temperature and moisture conditions, creep, and so on. In his review, emphasis was placed on the models that are displacement-

based and hybrid stress- based. The diversity of the different mathematical models for sandwich structures are apparent in his review.

1.3 Piezoelectric ceramics

1.3.1 Piezoelectric material

A piezoelectric material, one of the most widely used intelligent materials, produces an electric polarization when subjected to a mechanical stress and conversely, it strains under the applied electric field. The microscopic physics of these materials, including crystal physics and solid-state physics, are well explained in Ikeda.[22] The microscopic aspects of these materials are beyond the scope of present research. The primary interest here is the macroscopic electro-mechanical aspects of the material.

Piezoelectric material can be used as sensors or actuators because of their unique characteristics previously mentioned. They have been used in many transducers such as strain gages, pressure transducers, and so on. One of the piezoelectric materials is a piezoelectric ceramic, primarily based on lead ziconate titanate, which is abbreviated as PZT. PZT, an isotropic material before being polarized can be fabricated into a variety of shapes. Piezoelectric properties are established by polarization. In the manufacturing process, after PZT's are fabricated into shapes, electrodes are applied. The PZT is then heated in a strong DC electric field environment resulting in the polarization of the PZT, meaning the molecular dipoles of the ceramic are aligned in the direction of the applied field, known as the poling direction. The poling direction is defined as the x_3-axis in the material, and after poling the PZT behaves as a transversely isotropic material with the x_1-x_2 plane as the plane of isotropy.

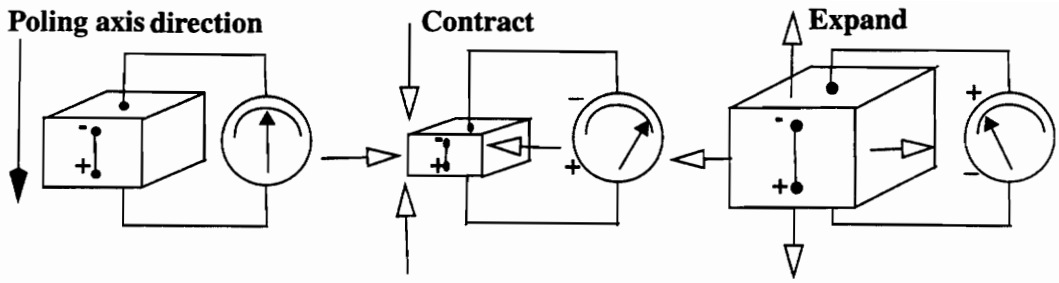

Fig. 1.3 Electro-mechanical response of typical PZT[23]

A PZT material with positive piezoelectric strain coefficient expands when an electric field is applied in the poling direction and contracts if the electric field is in the opposite direction from the poling direction as shown in Fig. 1.3. In Fig. 1.3, the thickness of PZT, the contracting force, and the expanding force are highly exaggerated for the purpose of illustration. The magnitude of the electric field, E, depends on the applied voltage, V, and the thickness of PZT, t, as

$$E = \frac{V}{t} \tag{1.2}$$

The relationship between the induced strains, Λ, and the applied electric field, E, is

$$\Lambda = dE \tag{1.3}$$

where d is piezoelectric strain coefficient, and is a material property. The piezoelectric strain coefficient is determined experimentally. For a given voltage, the deformation can be measured, and from these measurements the electric strain coefficient can be computed from

$$d = \frac{\Lambda}{E} = \frac{\Delta L}{L}\frac{t}{V} \tag{1.4}$$

where ΔL is the elongation, and L the gage length. Since the electric field depends on the thickness of PZT, as shown in Eq. (1.2), so do the induced strains. Thus, for a given voltage, a thinner PZT produces larger induced strains.

Generally, PZT material is fabricated into a thin layer of various shapes. The primary interest of using this flat configurations is to induce strains in the x_1 and x_2 directions, which are normal to the poling axis. The elongation induced in the x_3 direction is negligible compared to elongations induced in x_1 and x_2 direction since the thickness is very small compare to the length and width. There is a so-called "stack actuator" configuration, which consists of many PZT's stacked on top of one another. This stacked configuration was developed in order to induce appreciable elongation in x_3 direction. Since there are so many PZT's in a stack, the accumulation of x_3-direction elongations of each PZT can be larger than that in the x_1 and x_2 directions.

1.3.2 Modeling of structures with piezoelectric ceramics

Crawley and De Luis[24] developed static analytical models of the piezoelectric actuators coupled to structures. Their models were one-dimensional having PZT patches bonded on the surfaces or embedded into beams. They accounted for a finite thickness adhesive layer between the patches and the beam for the bonded PZT case. It was shown that under the assumption of perfect bonding the induced strains in substrate result from load transfer occurring in a narrow edge zone of the actuators. The static models of Crawley and De Luis[24] were generalized by Im and Atluri[25], to include a general loading in addition to the induced strains from piezoelectric actuators. Im and Atluri[25] considered axial force and a transverse shear force acting on the beam and found these forces significantly effect the shear stress distribution in the adhesive layer.

Crawley and Lazarus[26] treated the induced strain actuator as integral plies of lami-

nated plate without the adhesive layer in their "consistent plate model." Their model was based on the classical laminated plate theory. They obtained exact solutions for free boundary conditions and used the Ritz method to approximate the solution for more complicated boundary conditions. By comparing the analytical solutions with the experimental results, they revealed the dependency of the actuation strains on the induced strain under constrained boundary conditions. A "conservation of strain-energy" model for laminated beams and plates with spatially distributed induced strain actuators was developed by Wang and Rogers[27]. For a thin laminate, their model produced results that were very close to the so-called pin-force model. A pin-force model treats the substrate and actuators as separate bodies, and the forces from the actuators are transferred to the substrate by "pins" located at the edges of the actuators. As mentioned previously, the assumption of perfect bonding results in the load transfer at the edge zones of actuators and in the pin-force model, this load transfer is modeled at the edge of actuators by "pins."

1.3.3 Finite element modeling of structures with piezoelctric ceramic

Robbins and Reddy[28] developed and compared four finite element models of actuated beams. "The second multi-layer beam theory" was found to satisfy all the traction boundary conditions of the problems. The importance of including transverse shear deformation in the analysis was emphasized. A finite element analysis of a composite plate with distributed PZT sensors and actuators was investigated by Ha et al.[29] An eight-node three-dimensional element was used and incompatible modes were taken into account to the model the global behavior due to the local deformations. The model was verified with experiments. Hwang and Park[30] used four-noded 12 degrees of freedom quadrilateral plate bending elements with 1 electrical dof in their analysis. They investigsted the con-

trolling of vibration of a laminated plate with PZT sensors/actuators. This model was verified with experiments and the efficiency of the model was validated. Suleman and Venkayya[31] used four-noded 24 degrees of freedom quadrilateral shell elements for their finite element formulation of a composite panel with piezoelectric sensors and actuator. They included one electrical degree of freedom for each piezoelectric layer. Their model was compared to the experimental and analytical results and a good agreement was obtained.

1.3.4 Torsional control by piezoelectric ceramics

Park et al.[32] developed one-dimensional models of isotropic beams with induced actuators. These models account for the shear lag effects by including a finite thickness adhesive layer, similar to the analysis by Crawley and De Luis.[24] Torsion was induced by having the actuator axis skewed from the beam axis. They developed a coupled extension, bending, and torsional model but its predictions did not agree with their experiments. It could predict the torsional trend. Chen and Chopra[33] used "a simplified uniform strain theory" to predict the static torsional response of rotor blades. Their experiments showed their static analytical model is not suitable. Park and Chopra[34] developed a one-dimensional beam model under piezoceramic actuation. The model included coupled extension, bending, and torsion. The effects of the cross-sectional warping and shear lag were studied. The significant effects of shear lag to torsion were revealed. Barrett[35] presented three directionally attached piezoelectric elements, or DAP elements, which are capable of inducing pure extension, bending or twist. DAP elements were treated as one of the layers in a perfectly bonded laminated plate in their analysis. The analytical model for the twist rate was verified through good correlation with experiments. Kawiecki and Smith[36] studied a PZT configuration which can induce torsional and bending deformations without

structural coupling. They arranged the DAP elements in a way that the extensional and torsional displacements decoupled. This concept was verified as sufficient to control torsional and bending vibrations simultaneously, by numerical, experimental, and analytical methods. Multiaxial beam deformation was investigated by Shieh.[37] Extensional, biaxial bending and torsional twisting were considered. "The four sectored, collocated sensor/ actuator pair design" was introduced. The Euler-Bernoulli beam assumption was taken in this analysis. The transient response study was done by finite element model using this new structural model. The efficiency of the model to control various deformations of the beam was verified by a numerical study only.

1.4 Objectives and approaches

The objectives of this study are:

1. To develop a one-dimensional structural model for the static response of sandwich composite beams in extension, bi-axial bending, and torsion with and without the presence of bonded PZT actuators.
2. To formulate a finite element from the structural model and evaluate the analytical method.
3. To study the effects of PZT actuator configurations on the response of the beam.

The structural model is developed from the displacement field suggested by Reddy.[15] A plate model with bonded PZT actuators is formulated first and then is reduced to a one dimensional beam model by additional assumptions on the displacements. All the structural models previously mentioned in the literature review use the effects of directionally attached piezoelectric actuators or DAP elements to induce twist. This new model is capable of inducing a twist without using a DAP element since a higher order resultant, bimo-

ment, is integrated into the model. The finite element model is developed with one dimensional, two noded elements. An element with PZT actuators and one without PZT actuators are constructed and assembled in ways to model different configurations. The PZT actuator is assumed to be perfectly bonded to the beam.

1.5 Outline

Chapter 2 describe the formulation of a plate theory with PZT layers based on the Reddy's higher shear deformation theory. In Chapter 3, the reduction of the plate theory to the beam theory is explained. The finite element formulation is presented in Chapter 4. The results from numerical studies are discussed in Chapter 5. Finally, Chapter 6 contains the conclusion and future work.

2. *Higher-order transverse shear deformation plate theory*

A higher-order transverse shear deformation theory is developed for a plate with bonded PZT actuators. PZT actuators are assumed to be perfectly bonded on the top and the bottom of the plate; i.e., the bonding layer is assumed to be very thin and the adhesive is very stiff.

2.1 Approximate displacements and conjugate forces

The model is based on the consistent strain third order theory for laminated plates developed by Reddy[15]. It accounts for a parabolic distribution of the shear strain through the thickness and enforces the transverse shear stresses to vanish at the external surface. To satisfy these conditions, cubic functions in thickness coordinate are required for the inplane displacements expansion. The transverse displacement is treated as a constant through the thickness.

Let a rectangular plate of thickness h be referenced to a cartesian coordinate system x, y, z as shown in Fig. 2.1. The x-axis is parallel to what is termed the longitudinal dimen-

sion, the y-axis is parallel to the width dimension, and the z-axis is parallel to the thickness

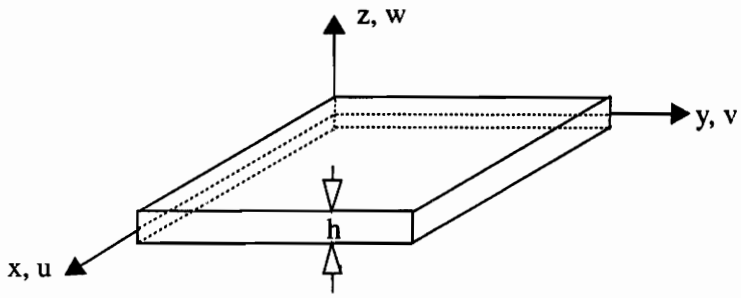

Fig. 2.1 The coordinate system of a plate.

dimension. Coordinate z=0 is at the middle surface of the plate; $-h/2 \le z \le h/2$. Displacements in the x-, y-, and z-coordinate directions are designated by u, v, and w, respectively. These displacements are assumed to be continuous functions, along with any necessary derivatives, of the coordinates x, y, and z defining the original position of material points in the plate. The displacement field given by Reddy[15] is

$$u(x,y,z) = u_0(x,y) + z\left[\psi_x - \frac{4}{3}\left(\frac{z}{h}\right)^2\left(\psi_x + \frac{\partial w}{\partial x}\right)\right]$$

$$v(x,y,z) = v_0(x,y) + z\left[\psi_y - \frac{4}{3}\left(\frac{z}{h}\right)^2\left(\psi_y + \frac{\partial w}{\partial y}\right)\right]$$

$$w(x,y,z) = w_0(x,y) \tag{2.1}$$

in which $\psi_x(x,y)$ and $\psi_y(x,y)$ are the rotations of the normal to the middle plane in the x-direction and y-direction, respectively, and $u_0(x,y)$, $v_0(x,y)$, and $w_0(x,y)$ are the displacements of points on the middle surface. Senthilnathan et al.[38] suggests the transformations

$$w(x,y,z) = w_b + w_s$$

$$\psi_x = -\frac{\partial w_b}{\partial x} \qquad \psi_y = -\frac{\partial w_b}{\partial y} \tag{2.2}$$

in which the transverse displacement w_b is the component due to bending and w_s is the component due to shear. Using Eq. (2.2), Eq. (2.1) can be written as

$$
\begin{aligned}
u(x, y, z) &= u_0 - z\frac{\partial w_b}{\partial x} - \frac{4}{3}\frac{z^3}{h^2}\frac{\partial w_s}{\partial x} \\
v(x, y, z) &= v_0 - z\frac{\partial w_b}{\partial y} - \frac{4}{3}\frac{z^3}{h^2}\frac{\partial w_s}{\partial y} \\
w(x, y, z) &= w_b + w_s
\end{aligned}
\tag{2.3}
$$

The strain components based on the proposed displacement field of Eq. (2.3) are determined from the linear strain displacement equations of elasticity in cartesian coordinates. The strain components are

$$
\begin{aligned}
\varepsilon_x &= \varepsilon_1^0 + z\varepsilon_1^1 + \frac{4}{3}\frac{z^3}{h^2}\varepsilon_1^2 & \varepsilon_{yz} &= \left(1 - 4\frac{z^2}{h^2}\right)\varepsilon_4^0 \\
\varepsilon_y &= \varepsilon_2^0 + z\varepsilon_2^1 + \frac{4}{3}\frac{z^3}{h^2}\varepsilon_2^2 & \varepsilon_{xz} &= \left(1 - 4\frac{z^2}{h^2}\right)\varepsilon_5^0 \\
\varepsilon_z &= 0 & \varepsilon_{xy} &= \varepsilon_6^0 + z\varepsilon_6^1 + \frac{4}{6}\frac{z^3}{h^2}\varepsilon_6^2
\end{aligned}
\tag{2.4}
$$

where

$$
\begin{aligned}
\varepsilon_1^0 &= \frac{\partial u_0}{\partial x} & \varepsilon_1^1 &= -\frac{\partial^2 w_b}{\partial x^2} & \varepsilon_1^2 &= -\frac{\partial^2 w_s}{\partial x^2} \\
\varepsilon_2^0 &= \frac{\partial v_0}{\partial y} & \varepsilon_2^1 &= -\frac{\partial^2 w_b}{\partial y^2} & \varepsilon_2^2 &= -\frac{\partial^2 w_s}{\partial y^2} \\
\varepsilon_6^0 &= \frac{\partial u_0}{\partial y} + \frac{\partial v_0}{\partial x} & \varepsilon_6^1 &= -2\frac{\partial^2 w_b}{\partial x \partial y} & \varepsilon_6^2 &= -2\frac{\partial^2 w_s}{\partial x \partial y} \\
\varepsilon_4^0 &= \frac{\partial w_s}{\partial y} & \varepsilon_5^0 &= \frac{\partial w_s}{\partial x}
\end{aligned}
\tag{2.5}
$$

The internal virtual work per unit middle surface area for the plate is

$$\delta \overline{W}_{int} = \int_h (\sigma_x \delta\varepsilon_x + \sigma_y \delta\varepsilon_y + \sigma_z \delta\varepsilon_z + \tau_{yz}\delta\varepsilon_{yz} + \tau_{zx}\delta\varepsilon_{zx} + \tau_{xy}\delta\varepsilon_{xy})\, dz \tag{2.6}$$

where σ_i is the normal stress on the i surface and τ_{ij} is the shear stress on the i surface in the j direction. By substituting Eq. (2.5) into Eq. (2.6) for the virtual strains, the virtual work for the plate can be integrated through the thickness. For clarity, each term of Eq. (2.6) will be expanded and integrated separately. In the process, plate stress resultants are defined.

The first term is

$$\int_h \sigma_x \delta\varepsilon_x dz = \int_{-\frac{h}{2}}^{\frac{h}{2}} \sigma_x \left(\delta\varepsilon_1^0 - z\delta\varepsilon_1^1 - \frac{4}{3}\frac{z^3}{h^2}\delta\varepsilon_1^2 \right) dz$$

$$= \delta\varepsilon_1^0 \int_{-\frac{h}{2}}^{\frac{h}{2}} \sigma_x dz + \delta\varepsilon_1^1 \int_{-\frac{h}{2}}^{\frac{h}{2}} z\sigma_x dz + \delta\varepsilon_1^2 \int_{-\frac{h}{2}}^{\frac{h}{2}} \frac{4}{3}\frac{z^3}{h^2}\sigma_x dz = N_x \delta\varepsilon_1^0 + M_x \delta\varepsilon_1^1 + P_x \delta\varepsilon_1^2 \tag{2.7}$$

in which the resultants are defined as

$$N_x = \int_{-\frac{h}{2}}^{\frac{h}{2}} \sigma_x dz \qquad M_x = \int_{-\frac{h}{2}}^{\frac{h}{2}} z\sigma_x dZ \qquad P_x = \int_{-\frac{h}{2}}^{\frac{h}{2}} \frac{4}{3}\frac{z^3}{h^2}\sigma_x dZ \tag{2.8}$$

The second term in Eq. (2.6) expands as follows;

$$\int_{-\frac{h}{2}}^{\frac{h}{2}} \sigma_y \delta\varepsilon_y dz = \int_{-\frac{h}{2}}^{\frac{h}{2}} \sigma_y \left(\delta\varepsilon_2^0 + z\delta\varepsilon_2^1 + \frac{4}{3}\frac{z^3}{h^2}\delta\varepsilon_2^2 \right) dz$$

$$= \delta\varepsilon_2^0 \int_{-\frac{h}{2}}^{\frac{h}{2}} \sigma_y dz + \delta\varepsilon_2^1 \int_{-\frac{h}{2}}^{\frac{h}{2}} z\sigma_y dz + \delta\varepsilon_2^2 \int_{-\frac{h}{2}}^{\frac{h}{2}} \frac{4}{3}\frac{z^3}{h^2}\sigma_y dz = N_y \delta\varepsilon_2^0 + M_y \delta\varepsilon_2^1 + P_y \delta\varepsilon_2^2 \tag{2.9}$$

in which

$$N_y = \int_{-\frac{h}{2}}^{\frac{h}{2}} \sigma_y dz \qquad M_y = \int_{-\frac{h}{2}}^{\frac{h}{2}} z\sigma_y dZ \qquad P_y = \int_{-\frac{h}{2}}^{\frac{h}{2}} \frac{4}{3}\frac{z^3}{h^2}\sigma_y dZ \tag{2.10}$$

Since ε_z is zero, and $\delta\varepsilon_z$ is zero, the third term vanishes; i.e.

$$\int_{-\frac{h}{2}}^{\frac{h}{2}} \sigma_z \delta\varepsilon_z dz = 0 \tag{2.11}$$

The fourth term in Eq. (2.6) expands as

$$\int_{-\frac{h}{2}}^{\frac{h}{2}} \tau_{yz} \delta\varepsilon_{yz} dz = \int_{-\frac{h}{2}}^{\frac{h}{2}} \tau_{yz} \left(1 - 4\frac{z^2}{h^2} \right) \delta\varepsilon_4^0 dz = Q_y \delta\varepsilon_4^0 \tag{2.12}$$

where

$$Q_y = \int_{-\frac{h}{2}}^{\frac{h}{2}} \tau_{yz}\left(1 - 4\frac{z^2}{h^2}\right)dz \tag{2.13}$$

The fifth term is

$$\int_{-\frac{h}{2}}^{\frac{h}{2}} \tau_{zx}\delta\varepsilon_{zx}dz = \int_{-\frac{h}{2}}^{\frac{h}{2}} \tau_{zx}\left(1 - 4\frac{z^2}{h^2}\right)\delta\varepsilon_5^0 dz = Q_x\delta\varepsilon_5^0 \tag{2.14}$$

where

$$Q_x = \int_{-\frac{h}{2}}^{\frac{h}{2}} \tau_{zx}\left(1 - 4\frac{z^2}{h^2}\right)dz \tag{2.15}$$

The last term in Eq. (2.6) is

$$\int_{-\frac{h}{2}}^{\frac{h}{2}} \tau_{xy}\delta\varepsilon_{xy}dz = \int_{-\frac{h}{2}}^{\frac{h}{2}} \tau_{xy}\left(\delta\varepsilon_6^0 + z\delta\varepsilon_6^1 + \frac{4}{3}\frac{Z^3}{h^2}\delta\varepsilon_6^2\right)dz$$

$$= \delta\varepsilon_6^0\int_{-\frac{h}{2}}^{\frac{h}{2}} \tau_{xy}dz + \delta\varepsilon_6^1\int_{-\frac{h}{2}}^{\frac{h}{2}} z\tau_{xy}dz + \delta\varepsilon_6^2\int_{-\frac{h}{2}}^{\frac{h}{2}} \frac{4}{3}\frac{z^3}{h^2}\tau_{xy}dz = N_{xy}\delta\varepsilon_6^0 + M_{xy}\delta\varepsilon_6^1 + P_{xy}\delta\varepsilon_6^2 \tag{2.16}$$

where

$$N_{xy} = \int_{-\frac{h}{2}}^{\frac{h}{2}} \tau_{xy}dz \qquad M_{xy} = \int_{-\frac{h}{2}}^{\frac{h}{2}} z\tau_{xy}dz \qquad P_{xy} = \int_{-\frac{h}{2}}^{\frac{h}{2}} \frac{4}{3}\frac{z^3}{h^2}\tau_{xy}dz \tag{2.17}$$

The stress resultants N_x, N_y, and N_{xy}, the moment resultants M_x, M_y, and M_{xy}, the transverse shear resultants Q_x and Q_y, and the higher order resultants P_x, P_y, and P_{xy} are shown in their positive senses acting on the positive x and y faces in Fig. 2.2.

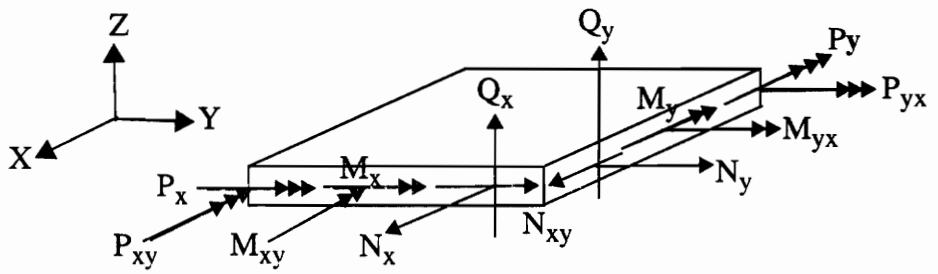

Fig. 2.2 Plate resultants in Reddy's[15] theory.

Summarizing, the internal virtual work per unit middle surface area is

$$\delta \overline{W}_{int} = N_x \delta\varepsilon_1^0 + M_x \delta\varepsilon_1^1 + P_x \delta\varepsilon_1^2 + N_y \delta\varepsilon_2^0 + M_y \delta\varepsilon_2^1 + P_y \delta\varepsilon_2^2$$
$$+ Q_y \delta\varepsilon_4^0 + Q_x \delta\varepsilon_5^0 + N_{xy} \delta\varepsilon_6^0 + M_{xy} \delta\varepsilon_6^1 + P_{xy} \delta\varepsilon_6^2 \qquad (2.18)$$

and the strains are given in terms of the displacements by Eq. (2.5).

2.2 *Electroelastic constitutive equation*

Consider a PZT patch like that shown in Fig. 2.3. Piezoceramics materials are isotropic originally but behaves as transversely isotropic after the poling direction is defined as

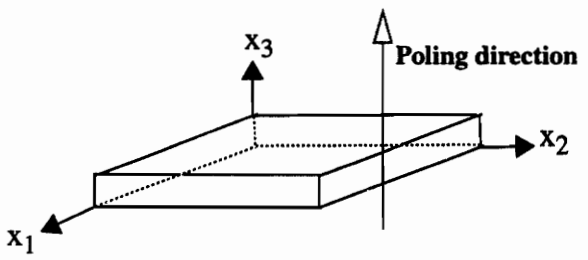

Fig. 2.3 The coordinate system of a PZT patch.

explained in Chapter 1. There are five independent elastic constants for transversely isotropic materials and in addition, two more independent electric constants for the piezoelectric materials. The shear strain in the plane perpendicular to the poling direction x_3 can not be induced in the piezoelectric material. Therefore, in plane shear strain in x_1-x_2 plane depends only on the mechanical contribution. There are three independent piezoelectric constants and thus a total of ten independent constants in the strain-stress relation. The constitutive law[39] is

$$\begin{bmatrix} D_1 \\ D_2 \\ D_3 \\ \varepsilon_{11} \\ \varepsilon_{22} \\ \varepsilon_{33} \\ \varepsilon_{23} \\ \varepsilon_{31} \\ \varepsilon_{12} \end{bmatrix} = \begin{bmatrix} e_1^T & 0 & 0 & 0 & 0 & 0 & 0 & d_{15} & 0 \\ 0 & e_1^T & 0 & 0 & 0 & 0 & d_{15} & 0 & 0 \\ 0 & 0 & e_3^T & d_{31} & d_{31} & d_{33} & 0 & 0 & 0 \\ 0 & 0 & d_{31} & S_{11}^E & S_{12}^E & S_{13}^E & 0 & 0 & 0 \\ 0 & 0 & d_{31} & S_{12}^E & S_{11}^E & S_{13}^E & 0 & 0 & 0 \\ 0 & 0 & d_{33} & S_{13}^E & S_{13}^E & S_{33}^E & 0 & 0 & 0 \\ 0 & d_{15} & 0 & 0 & 0 & 0 & S_{55}^E & 0 & 0 \\ d_{15} & 0 & 0 & 0 & 0 & 0 & 0 & S_{55}^E & 0 \\ 0 & 0 & 0 & 0 & 0 & 0 & 0 & 0 & S_{66}^E \end{bmatrix} \begin{bmatrix} E_1 \\ E_2 \\ E_3 \\ \sigma_{11} \\ \sigma_{22} \\ \sigma_{33} \\ \sigma_{23} \\ \sigma_{31} \\ \sigma_{12} \end{bmatrix} \tag{2.19}$$

where

D_i.....Electrical displacement (Coulomb/m^2) --- defined below
e_i.....Permittivity (Farad/m) --- defined below
d_{ij}.....Piezoelectric strain coefficient (m/V)
E_i.....Electric field (V/m)
ε_{ij}.....Strain
S_{ij}.....Compliance
σ_i.....Stress (N/m^2)

The superscript "T" in Eq. (2.19) denotes the values at constant or zero stress (free stress) and the superscript "E" denotes values at constant or zero field (short circuit). The electrical displacement, D_i, is the charge density in the material under the given electrical field and the given stresses. Permittivity, e_i, is the ratio of the amount of charge that the electroded material, here PZT, can store to the amount of charge that would be stored by electrodes separated in a vacuum at the same voltage and distance.

In practical cases there is only one poling direction in the material, thus the electric field can be applied only in the one direction. Generally, electrodes are applied across the poling direction, or the x_3 direction, for PZT patches. Thus the only component of the applied electric field in use is E_3, then

$$E_1 = E_2 = 0 \tag{2.20}$$

In this study, the PZT is treated as a perfectly bonded layer of a laminated plate and so through the thickness normal stress is assumed to be negligible; i.e,

$$\sigma_{33} = 0 \tag{2.21}$$

Also, we assume the electric field applied is maintained at the constant level, using a DC voltage source, which is the usual situation in the laboratory. This results in the decoupling of electrical and the mechanical problems. Then, for plane stress conditions with only electric field in the x_3-direction produced by DC voltage source, Eq. (2.19) reduces to

$$D_3 = e_3^T E_3 + d_{31}\sigma_{11} + d_{31}\sigma_{22}$$

$$\begin{bmatrix} \varepsilon_{11} \\ \varepsilon_{22} \\ \varepsilon_{12} \end{bmatrix} = \begin{bmatrix} S_{11}^E & S_{12}^E & 0 \\ S_{12}^E & S_{11}^E & 0 \\ 0 & 0 & S_{66}^E \end{bmatrix} \begin{bmatrix} \sigma_{11} \\ \sigma_{22} \\ \sigma_{12} \end{bmatrix} + \begin{bmatrix} d_{31} \\ d_{31} \\ d_{33} \end{bmatrix} E_3 \qquad \begin{bmatrix} \varepsilon_{23} \\ \varepsilon_{31} \end{bmatrix} = \begin{bmatrix} S_{55}^E & 0 \\ 0 & S_{55}^E \end{bmatrix} \begin{bmatrix} \sigma_4 \\ \sigma_5 \end{bmatrix} \tag{2.22}$$

Patches of the PZT material are used as actuators, not as sensors, in this analysis, so only the mechanical problem associated with Eq. (2.22) is developed here. Thus the first equation in Eq. (2.22), which represents the electrical displacement in the case where PZT is used as sensors, is of no concern here. For PZT materials used as sensors refer Ha et. al,[29] Hwang and Park,[30] Shieh,[37] and Dosch et al.[40] The rest of Eq. (2.22) can be inverted to give

$$\begin{bmatrix}\sigma_{11}\\ \sigma_{22}\\ \tau_{12}\end{bmatrix} = \begin{bmatrix}Q_{11} & Q_{12} & 0\\ Q_{12} & Q_{11} & 0\\ 0 & 0 & Q_{66}\end{bmatrix}\left(\begin{bmatrix}\varepsilon_{11}\\ \varepsilon_{22}\\ \varepsilon_{12}\end{bmatrix} - \begin{bmatrix}\Lambda\\ \Lambda\\ 0\end{bmatrix}\right) \qquad \begin{bmatrix}\tau_{23}\\ \tau_{31}\end{bmatrix} = \begin{bmatrix}Q_{55} & 0\\ 0 & Q_{55}\end{bmatrix}\begin{bmatrix}\varepsilon_{23}\\ \varepsilon_{31}\end{bmatrix} \tag{2.23}$$

where induced strains are

$$\begin{bmatrix}\Lambda\\ \Lambda\\ 0\end{bmatrix} = \begin{bmatrix}d_{31}\\ d_{31}\\ 0\end{bmatrix}E_3 \tag{2.24}$$

In this study we limit the orientation of the PZT material. That is, let the material coordinates of the PZT patches coincide with the coordinates of the plate, meaning x_1, x_2, and x_3 directions in Fig. 2.3 coincide with x, y, and z in Fig. 2.1, respectively. Then Eq. (2.23) can be expressed in more general way as

$$\begin{bmatrix}\sigma_x\\ \sigma_y\\ \tau_{xy}\end{bmatrix} = \begin{bmatrix}\overline{Q}_{11} & \overline{Q}_{12} & \overline{Q}_{16}\\ \overline{Q}_{12} & \overline{Q}_{22} & \overline{Q}_{26}\\ \overline{Q}_{16} & \overline{Q}_{26} & \overline{Q}_{66}\end{bmatrix}\left(\begin{bmatrix}\varepsilon_x\\ \varepsilon_y\\ \varepsilon_{xy}\end{bmatrix} - \begin{bmatrix}\Lambda\\ \Lambda\\ 0\end{bmatrix}\right) \qquad \begin{bmatrix}\tau_{yz}\\ \tau_{zx}\end{bmatrix} = \begin{bmatrix}\overline{Q}_{44} & \overline{Q}_{45}\\ \overline{Q}_{45} & \overline{Q}_{55}\end{bmatrix}\begin{bmatrix}\varepsilon_{yz}\\ \varepsilon_{zx}\end{bmatrix} \tag{2.25}$$

where $\overline{Q}_{ij}$'s are transformed reduced stiffness at zero field. For the structural layers,

$$\Lambda = 0 \tag{2.26}$$

and for the PZT layers,

$$\overline{Q}_{16} = \overline{Q}_{26} = \overline{Q}_{45} = 0 \qquad \overline{Q}_{11} = \overline{Q}_{22} = \frac{E_a}{1-\nu_a^2}$$

$$\overline{Q}_{12} = \frac{\nu_a E_a}{1-\nu_a^2} \qquad \overline{Q}_{66} = \frac{E_a}{2(1+\nu_a)} \tag{2.27}$$

in which E_a is the modulus of elasticity and ν_a is the Poisson's ratio for the actuator.

2.3 *Laminate constitutive equations*

Consider a laminate composed of two PZT actuators bonded to a substrate as shown in Fig. 2.4 with one actuator on the top and an identical one on the bottom of the substrate.

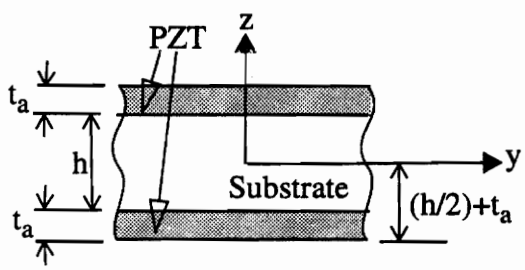

Fig. 2.4 A laminate with PZT actuators.

The thickness of the actuators is t_a. To obtain the constitutive law for this laminate, first substitute the stress strain law, Eq. (2.25), into the definitions of the resultants, Eqs. (2.8), (2.10), (2.13), (2.15), and (2.17), where the limits of integration are from -((h/2)+ta) to +((h/2)+ta). Second, substitute Eq. (2.4) for the strains, and carry out the integration through the thickness.

The final result of this process is

$$\begin{bmatrix} N_x \\ N_y \\ N_{xy} \\ M_x \\ M_y \\ M_{xy} \\ P_x \\ P_y \\ P_{xy} \end{bmatrix} = \begin{bmatrix} A_{11} & A_{12} & A_{16} & B_{11} & B_{12} & B_{16} & E_{11} & E_{12} & E_{16} \\ A_{12} & A_{22} & A_{26} & B_{12} & B_{22} & B_{26} & E_{12} & E_{22} & E_{26} \\ A_{16} & A_{26} & A_{66} & B_{16} & B_{26} & B_{66} & E_{16} & E_{26} & E_{66} \\ B_{11} & B_{12} & B_{16} & D_{11} & D_{12} & D_{16} & F_{11} & F_{12} & F_{16} \\ B_{12} & B_{22} & B_{26} & D_{12} & D_{22} & D_{26} & F_{12} & F_{22} & F_{26} \\ B_{16} & B_{26} & B_{66} & D_{16} & D_{26} & D_{66} & F_{16} & F_{26} & F_{66} \\ E_{11} & E_{12} & E_{16} & F_{11} & F_{12} & F_{16} & H_{11} & H_{12} & H_{16} \\ E_{12} & E_{22} & E_{26} & F_{12} & F_{22} & F_{26} & H_{12} & H_{22} & H_{26} \\ E_{16} & E_{26} & E_{66} & F_{16} & F_{26} & F_{66} & H_{16} & H_{26} & H_{66} \end{bmatrix} \begin{bmatrix} \varepsilon_1^0 \\ \varepsilon_2^0 \\ \varepsilon_6^0 \\ \varepsilon_1^1 \\ \varepsilon_2^1 \\ \varepsilon_6^1 \\ \varepsilon_1^2 \\ \varepsilon_2^2 \\ \varepsilon_6^2 \end{bmatrix} - \begin{bmatrix} N_x^\Lambda \\ N_y^\Lambda \\ N_{xy}^\Lambda \\ M_x^\Lambda \\ M_y^\Lambda \\ M_{xy}^\Lambda \\ P_x^\Lambda \\ P_y^\Lambda \\ P_{xy}^\Lambda \end{bmatrix}$$

$$\begin{bmatrix} Q_y \\ Q_x \end{bmatrix} = \begin{bmatrix} D_{44} & D_{45} \\ D_{45} & D_{55} \end{bmatrix} \begin{bmatrix} \varepsilon_4^0 \\ \varepsilon_5^0 \end{bmatrix} \tag{2.28}$$

where

$$(A_{ij}, B_{ij}, D_{ij}, E_{ij}, F_{ij}, H_{ij}) = \int_{-(\frac{h}{2}+t_a)}^{(\frac{h}{2}+t_a)} (\overline{Q}_{ij}) \left(1, z, z^2, \left(\frac{4}{3}\frac{z^3}{h^2}\right), \left(\frac{4}{3}\frac{z^4}{h^2}\right), \left(\frac{16}{9}\frac{z^6}{h^4}\right)\right) dz$$

$$(D_{ij}) = \int_{-(\frac{h}{2}+t_a)}^{(\frac{h}{2}+t_a)} \left(1 - \frac{4}{3}\frac{z^2}{h^2}\right) (\overline{Q}_{ij})\, dz \qquad i, j = 4, 5 \tag{2.29}$$

and the induced resultants are

$$N_x^\Lambda = N_y^\Lambda = \int_{-(\frac{h}{2}+t_a)}^{-\frac{h}{2}} \left(\frac{E_a}{1-\nu_a^2} + \frac{\nu_a E_a}{1-\nu_a^2}\right)\Lambda_{ba}dz + \int_{\frac{h}{2}}^{\frac{h}{2}+t_a} \left(\frac{E_a}{1-\nu_a^2} + \frac{\nu_a E_a}{1-\nu_a^2}\right)\Lambda_{ta}dz$$

$$N_{xy}^\Lambda = 0$$

$$M_x^\Lambda = M_y^\Lambda = \int_{-(\frac{h}{2}+t_a)}^{-\frac{h}{2}} \left(\frac{E_a}{1-\nu_a^2} + \frac{\nu_a E_a}{1-\nu_a^2}\right)z\Lambda_{ba}dz + \int_{\frac{h}{2}}^{\frac{h}{2}+t_a} \left(\frac{E_a}{1-\nu_a^2} + \frac{\nu_a E_a}{1-\nu_a^2}\right)z\Lambda_{ta}dz$$

$$M_{xy}^\Lambda = 0$$

$$P_x^\Lambda = P_y^\Lambda = \int_{-(\frac{h}{2}+t_a)}^{-\frac{h}{2}} \left(\frac{E_a}{1-\nu_a^2} + \frac{\nu_a E_a}{1-\nu_a^2}\right)\left(\frac{4}{3}\frac{z^3}{t_a^2}\right)\Lambda_{ba}dz$$

$$+ \int_{\frac{h}{2}}^{\frac{h}{2}+t_a} \left(\frac{E_a}{1-\nu_a^2} + \frac{\nu_a E_a}{1-\nu_a^2}\right)\left(\frac{4}{3}\frac{z^3}{t_a^2}\right)\Lambda_{ta}dz$$

$$P_{xy}^\Lambda = 0 \tag{2.30}$$

where superscript Λ and subscript "a" denote the induced strains and the PZT patches, respectively. The subscript "ba" denotes the actuators on the bottom surface and "ta" is the actuators on the top surface.

2.4 The configurations of PZT and induced forces

Induced resultants given by Eqs. (2.30) can not be activated simultaneously for some configurations of PZT. The actions induced depend on the configurations of the patches and the polarity and magnitude of the applied field. In this study, the patches are restricted to a rectangular planform with their x_1-, x_2-, and x_3-axes aligned with the x-, y-, and z-axes of the plate, respectively, as shown in Fig. 2.5. With this configuration, actions N^{Λ}_{xy}, M^{Λ}_{xy}, and P^{Λ}_{xy} in Eq. (2.30)

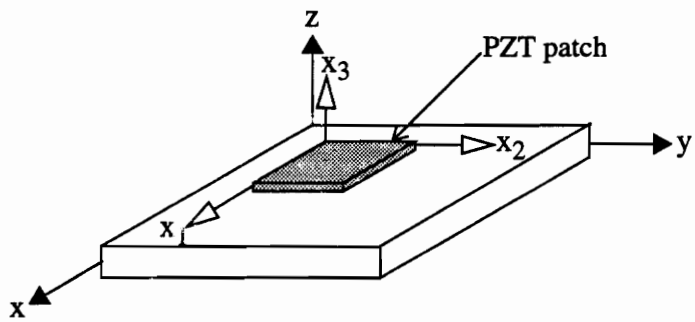

Fig. 2.5 The coordinate system of a plate and a PZT patch in this study.

can not be induced as shown by Eqs. (2.30). The patches have to be bonded off-axis on the plate, as shown in Fig. 2.6, in order to induce shear type actions. The PZT material does not have coupling between in-plane shear and E_3 component of the electric field,

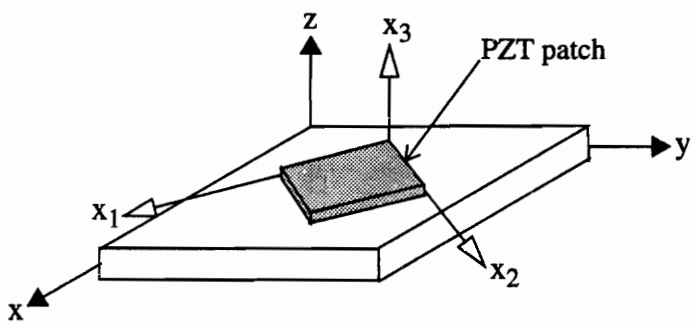

Fig. 2.6 The coordinate system of a plate and an off axis PZT patch.

since PZT is transversely isotropic in xy plane. For an off-axis patch, induced extensional

and compressive strains in the x_1- and x_2-directions results in an induced shear in the plate.

The applied voltage generates the induced forces through the induced strain Λ. If the same voltage magnitude and polarities are imposed on the top and bottom actuators, only the normal membrane resultants N_x^{Λ} and N_y^{Λ} of Eq. (2.30) can be induced, and extension results. This happens because of the symmetry of the top and bottom actuators and integrals of them through the thickness. To induce bending and no extension, voltages of the same magnitude but of opposite polarities are imposed on the top and bottom actuators. If the magnitudes of voltages on the top and the bottom actuators are different, independent of the voltage signs, all the forces can be induced at the same time.

3. *Beam Theory*

In order to derive a beam theory from the laminated plate theory of the previous chapter, certain assumptions to reduce the two-dimensional plate problem to a one-dimensional beam problem must be made. These assumptions are given in this chapter along with the derivation that results from their implementation. In the development of the beam theory the locations of the PZT patches across the width of the beam needs to be specified. An identical top and bottom pair are located between $y_4 < y < y_3$, and a second identical top and bottom pair are located between $y_2 < y < y_1$, where $y_4 < y_3 < y_2 < y_1$. See Fig. 3.1.

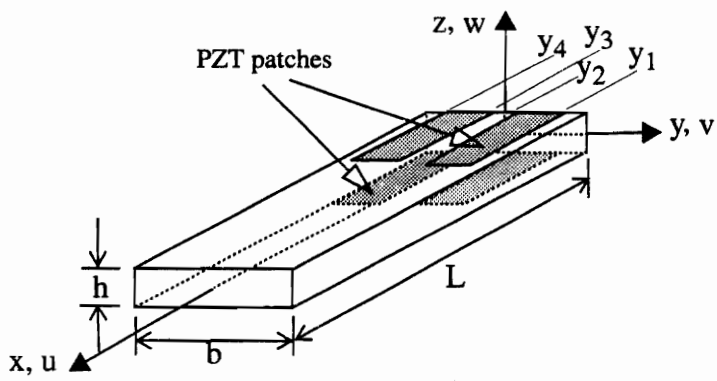

Fig. 3.1 The coordinate system and dimensions of a beam.

3.1 Approximate displacement and conjugate forces

To reduce to a beam theory, the plate displacements $u_0(x, y)$, $v_0(x, y)$, $w_b(x, y)$, and $w_s(x, y)$ are assumed to have an explicit dependence on the width-wise coordinate y. Consider two possible assumptions

Assumption 1:

$$\begin{aligned} u_0(x,y) &= \beta(x)\,y + \bar{u}_0(x) & w_b(x,y) &= \tau_b(x)\,y + w_{b0}(x) \\ v_0(x,y) &= \bar{v}_0(x) & w_s(x,y) &= \tau_s(x)\,y + w_{s0}(x) \end{aligned} \tag{3.1}$$

Assumption 2:

$$\begin{aligned} u_0(x,y) &= \beta(x)\,y + \bar{u}_0(x) & w_b(x,y) &= \tau(x)\,y + w_{b0}(x) \\ v_0(x,y) &= \bar{v}_0(x) & w_s(x,y) &= w_{s0}(x) \end{aligned} \tag{3.2}$$

The unknown coefficient functions β, τ_b, and τ_s are related to the plate displacements by

$$\beta(x) = \left.\frac{\partial u_0}{\partial y}\right|_{y=0} \quad \tau_b(x) = \tau(x) = \left.\frac{\partial w_b}{\partial y}\right|_{y=0} \quad \tau_s(x) = \left.\frac{\partial w_s}{\partial y}\right|_{y=0} \tag{3.3}$$

In assumption 2 $\tau_s(x)$ is neglected, and the inclusion of τ_s in assumption 1 leads to

$$\gamma_{yz} = \frac{\partial w_s}{\partial y}\left(1 - 4\frac{z^2}{h^2}\right) \tag{3.4}$$

From previous assumptions, we have the normal strains $\varepsilon_y=\varepsilon_z=0$. The additional condition of $\gamma_{yz} = 0$ for assumption 2 indicates that the cross section remains rigid in its plane. This is a general assumption of most of the thin-walled beam theories, so assumption 2 is adapted in the sequel.

From assumption 2 and the plate theory, the three-dimensional displacement field is approximated by

$$
\begin{aligned}
u(x,y,z) &= \bar{u}_0(x) - z\left(w_{b0}'(x) + \frac{4}{3}\frac{z^2}{h^2}w_{s0}'(x)\right) + y\beta(x) - yz\tau'(x) \\
v(x,y,z) &= \bar{v}_0(x) - z(\tau(x)) \\
w(x,y,z) &= \tau(x)y + w_{b0}(x) + w_{s0}(x)
\end{aligned}
\tag{3.5}
$$

in which primes denote derivatives with respect to x. The four terms on the right hand side of longitudinal displacement in the first of Eqs. (3.5) are interpreted as an extensional part, a part due to bending in the x-z plane, a part due to bending in the x-y plane, and a warping term due to torsion. Note that the distribution of the longitudinal displacement in the cross section due to warping is 'y z', which is the distribution for free warping of a homogeneous thin-walled rectangular bar subjected to uniform torque. Hence, our assumptions represented by Eqs. (3.2) require that the width b be at least an order of magnitude larger that thickness h for the torsion results to be reasonably accurate. The v and w displacements in the second and third of Eqs. (3.5) are composed of a translational term due to bending and a second term due to rotation of the cross section in torsion about the x-axis. All rotations are assumed to be small.

The strains field determined from Eqs. (3.5) are

$$
\begin{aligned}
\varepsilon_{xx} &= \bar{u}_0' - z\left(w_{b0}'' + \frac{4}{3}\frac{z^2}{h^2}w_{s0}''\right) + y\beta' + yz(-\tau'') \\
\varepsilon_{yy} &= \varepsilon_{zz} = 0 & \gamma_{yz} &= 0 \\
\gamma_{xy} &= \beta + (\bar{v}_0' - 2z\tau') & \gamma_{xz} &= w_{s0}'\left(1 - 4\frac{z^2}{h^2}\right)
\end{aligned}
\tag{3.6}
$$

The two-dimensional strains for the plate theory are

$$\varepsilon_1^0 = \bar{u}_0' + \beta' y \qquad \varepsilon_1^1 = -\tau'' y + w_{b0}'' \qquad \varepsilon_1^2 = -w_{s0}'' \qquad \varepsilon_5^0 = w_{s0}'$$
$$\varepsilon_6^0 = \beta + \bar{v}_0' \qquad \varepsilon_6^1 = -2\tau' \qquad \varepsilon_6^2 = \varepsilon_2^0 = \varepsilon_2^1 = \varepsilon_2^2 = 0 \tag{3.7}$$

The internal virtual work for the beam is obtained by integrating Eq. (2.18) over the area of the plate. Since strains $\varepsilon_{yy}=\gamma_{yz}=0$, the virtual strains $\delta\varepsilon_2{}^0=\delta\varepsilon_2{}^1=\delta\varepsilon_2{}^2=\delta\varepsilon_4{}^0=0$ in Eq. (2.18). In addition the kinematic assumptions result in $\delta\varepsilon_6{}^2=0$ (Eq. (3.7)). Thus the internal virtual work for the beam becomes

$$\delta W_{int} = \int_0^L \left(\int_0^b \left(N_x (\delta\bar{u}_0' + y\delta\beta') + N_{xy}(\delta\beta + \delta\bar{v}_0') + M_x(-y\delta\tau'' - \delta w_{b0}'') \right.\right.$$
$$\left.\left. + M_{xy}(-2\delta\tau') + P_x(-\delta w_{s0}'') + Q_x(\delta w_{s0}') \right) dy \right) dx \tag{3.8}$$

Integration of the plate resultants across the width gives the internal virtual work as

$$\delta W_{int} = \int_0^L \left(P(\delta\bar{u}_0') + V_y(\delta\beta + \delta\bar{v}_0') + V_z(\delta w_{s0}') + M_{yb}(-\delta w_{b0}'') \right.$$
$$\left. + M_{ys}(-\delta w_{s0}'') + M_z(\delta\beta') + B(-\delta\tau'') - T_s(\delta\tau') \right) dx \tag{3.9}$$

in which the following beam resultants are defined

P.....Axial force
V_y.....Shear force in y-direction
V_z.....Shear force in z-direction
M_{yb}.....Bending moment about y-axis due to transverse displacement w_b
M_{ys}.....Bending moment about y-axis due to the transverse displacement w_s
M_z.....Bending moment about z-axis
B.....Bimoment
T_s.....Saint Venant torque

The mathematical definitions of the beam resultants in terms of plate resultants and in

terms of x-face stresses are

$$P = \int_{-\frac{b}{2}}^{\frac{b}{2}} N_x dy = \iint_A \sigma_x dydz \qquad M_{ys} = \int_{-\frac{b}{2}}^{\frac{b}{2}} P_x dy = \iint_A \frac{4}{3}\frac{z^3}{h^2}\sigma_x dydz$$

$$V_y = \int_{-\frac{b}{2}}^{\frac{b}{2}} N_{xy} dy = \iint_A \tau_{xy} dydz \qquad M_z = \int_{-\frac{b}{2}}^{\frac{b}{2}} yN_x dy = \iint_A y\sigma_x dydz$$

$$V_z = \int_{-\frac{b}{2}}^{\frac{b}{2}} Q_x dy = \iint_A \tau_{xz}\left(1 - 4\frac{z^2}{h^2}\right) dydz \qquad B = \int_{-\frac{b}{2}}^{\frac{b}{2}} yM_x dy = \iint_A yz\sigma_x dydz$$

$$M_{yb} = \int_{-\frac{b}{2}}^{\frac{b}{2}} M_x dy = \iint_A z\sigma_x dydz \qquad T_s = 2\int_{-\frac{b}{2}}^{\frac{b}{2}} M_{xy} dy = 2\iint_A z\tau_{xy} dydz \tag{3.10}$$

The conjugate forces are shown in Fig. 3.2 in the positive directions.

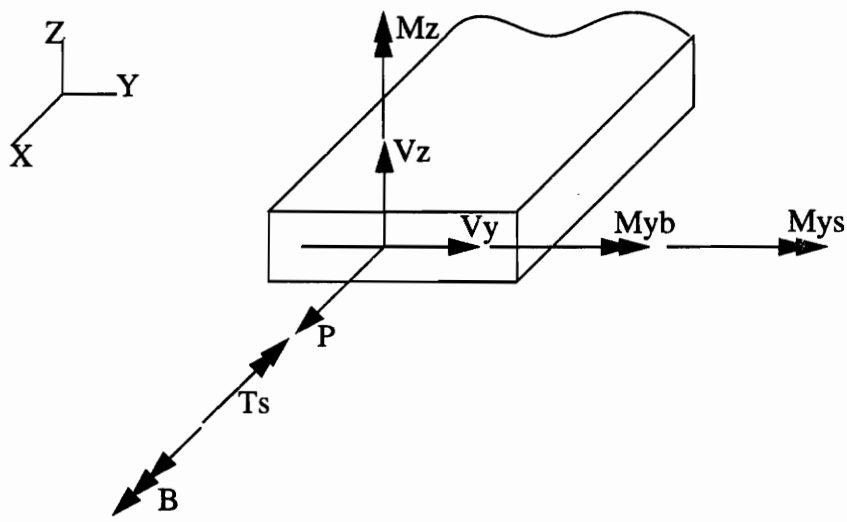

Fig. 3.2 Resultant forces and moments of a beam.

3.2 Constitutive equation

A second assumption for the beam theory is to neglect lateral resultants with respect to longitudinal resultants in the constitutive law, because the beam is much longer than its largest cross sectional dimension. That is, in the material law take

$$N_y = M_y = P_y = Q_y = 0 \tag{3.11}$$

To impose this conditions on the constitutive equation, Eq. (2.28), this equation is partitioned as follows

$$\begin{bmatrix} \{N^x\} \\ \{N^y\} \end{bmatrix} = \begin{bmatrix} [D^{xx}] & [D^{xy}] \\ [D^{yx}] & [D^{yy}] \end{bmatrix} \begin{bmatrix} \{\varepsilon^x\} \\ \{\varepsilon^y\} \end{bmatrix} - \begin{bmatrix} \{N^x_\Lambda\} \\ \{N^y_\Lambda\} \end{bmatrix} \tag{3.12}$$

where

$$\begin{aligned}
\{N^x\}^T &= \{N_x, N_{xy}, M_x, M_{xy}, P_x, P_{xy}\} \\
\{N^y\}^T &= \{N_y, M_y, P_y\} \\
\{\varepsilon^x\}^T &= \{\varepsilon^0_1, \varepsilon^0_6, \varepsilon^1_1, \varepsilon^1_6, \varepsilon^2_1, \varepsilon^2_6\} \\
\{\varepsilon^y\}^T &= \{\varepsilon^0_2, \varepsilon^1_2, \varepsilon^2_2\} \\
\{N^x_\Lambda\}^T &= \{N^\Lambda_x, N^\Lambda_{xy}, M^\Lambda_x, M^\Lambda_{xy}, P^\Lambda_x, P^\Lambda_{xy}\} \\
\{N^y_\Lambda\}^T &= \{N^\Lambda_y, M^\Lambda_y, P^\Lambda_y\}
\end{aligned} \tag{3.13}$$

and

$$\left[D^{xx}\right] = \begin{bmatrix} A_{11}\,A_{16} & B_{11}\,B_{16} & E_{11}\,E_{16} \\ A_{16}\,A_{66} & B_{16}\,B_{66} & E_{16}\,E_{66} \\ B_{11}\,B_{16} & D_{11}\,D_{16} & F_{11}\,F_{16} \\ B_{16}\,B_{66} & D_{16}\,D_{66} & F_{16}\,F_{66} \\ E_{11}\,E_{16} & F_{11}\,F_{16} & H_{11}\,H_{16} \\ E_{16}\,E_{66} & F_{16}\,F_{66} & H_{16}\,H_{66} \end{bmatrix} \qquad \left[D^{xy}\right] = \begin{bmatrix} A_{12} & B_{12} & E_{12} \\ A_{26} & B_{26} & E_{26} \\ B_{12} & D_{12} & F_{12} \\ B_{26} & D_{26} & F_{26} \\ E_{12} & F_{12} & H_{12} \\ E_{26} & F_{26} & H_{26} \end{bmatrix}$$

$$\left[D^{yx}\right] = \left[D^{xy}\right]^T \qquad \left[D^{yy}\right] = \begin{bmatrix} A_{22}\,B_{22}\,E_{22} \\ B_{22}\,D_{22}\,F_{22} \\ E_{22}\,F_{22}\,H_{22} \end{bmatrix} \tag{3.14}$$

Setting $\{N^y\}$ in Eq. (3.12) equal to zero gives

$$\{N^y\} = \{0\} = \left[D^{yx}\right]\{\varepsilon^x\} + \left[D^{yy}\right]\{\varepsilon^y\} - \{N^y_\Lambda\} \tag{3.15}$$

Thus the lateral strain vector $\{\varepsilon_y\}$ can be solved in terms of axial strain and the lateral induced stress;

$$\{\varepsilon^y\} = -\left[D^{yy}\right]^{-1}\left[D^{yx}\right]\{\varepsilon^x\} + \left[D^{yy}\right]^{-1}\{N^y_\Lambda\} \tag{3.16}$$

By substituting Eq. (3.16) into Eq. (3.12), $\{N^x\}$ can be expressed as

$$\begin{aligned} \{N^x\} &= \left[\left[D^{xx}\right] - \left[D^{xy}\right]\left[D^{yy}\right]^{-1}\left[D^{yx}\right]\right]\{\varepsilon^x\} + \left[D^{xy}\right]\left[D^{yy}\right]^{-1}\{N^y_\Lambda\} - \{N^x_\Lambda\} \\ &= \left[\bar{D}\right]\{\varepsilon^x\} + \left[\tilde{D}\right]\{N^y_\Lambda\} - \{N^x_\Lambda\} \end{aligned} \tag{3.17}$$

Such the transverse shear resultant Q_y in Eq. (2.28) is zero from Eq. (3.11), the transverse shear strain can be solved for and eliminated in the material law. That is,

$$Q_y = D_{44}\varepsilon_4^0 + D_{45}\varepsilon_5^0 = 0 \tag{3.18}$$

so

$$\varepsilon_4^0 = -\frac{D_{45}\varepsilon_5^0}{D_{44}} \tag{3.19}$$

and the material law for transverse shear resultant Q_x becomes

$$Q_x = \left(D_{55} - \frac{(D_{45})^2}{D_{44}}\right)\varepsilon_5^0 \tag{3.20}$$

After these manipulations the constitutive law is

$$\{N\} = [D]\{\hat{\varepsilon}\} + \{N_\Lambda\} \tag{3.21}$$

where

$$\{N\} = \begin{Bmatrix} \{N^x\} \\ Q_x \end{Bmatrix} \qquad [D] = \begin{bmatrix} [\bar{D}] & \{0\} \\ \{0\}^T & \overset{\circ}{D}_{55} \end{bmatrix} \qquad \{\hat{\varepsilon}\} = \begin{Bmatrix} \{\varepsilon^x\} \\ \varepsilon_5^0 \end{Bmatrix}$$

$$\{N_\Lambda\} = \begin{Bmatrix} [\tilde{D}]\{N_\Lambda^y\} \\ 0 \end{Bmatrix} - \begin{Bmatrix} \{N_\Lambda^x\} \\ 0 \end{Bmatrix} \qquad \overset{\circ}{D}_{55} = D_{55} - \frac{(D_{45})^2}{D_{44}} \tag{3.22}$$

3.3 Stiffness matrix

Now, by integrating Eqs. (3.10) with the reduced constitutive law given by Eq. (3.21), the stiffness matrix for the one-dimensional model can be obtained. This derivation is done component by component in the following,

$$
\begin{aligned}
P = \int_{-\frac{b}{2}}^{\frac{b}{2}} N_x dy &= \int_{-\frac{b}{2}}^{\frac{b}{2}} (\overline{D}_{11}\varepsilon_1^0 + \overline{D}_{12}\varepsilon_6^0 + \overline{D}_{13}\varepsilon_1^1 + \overline{D}_{14}\varepsilon_6^1 + \overline{D}_{15}\varepsilon_1^2)\, dy \\
&\qquad - \int_{y_1}^{y_2} N_\Lambda(1)\, dy - \int_{y_3}^{y_4} N_\Lambda(1)\, dy \\
&= b\overline{D}_{11}(\bar{u}_0{}') + b\overline{D}_{12}(\beta + \bar{v}_0{}') + b\overline{D}_{13}(-w_{b0}{}'') + 2b\overline{D}_{14}(-\tau') + b\overline{D}_{15}(-w_{s0}{}'') \\
&\qquad - (y_2 - y_1)\,((\tilde{D}_{11}N_y^\Lambda + \tilde{D}_{12}M_y^\Lambda + \tilde{D}_{13}P_y^\Lambda) - N_x^\Lambda) \\
&\qquad - (y_4 - y_3)\,(\tilde{D}_{11}N_y^\Lambda + \tilde{D}_{12}M_y^\Lambda + \tilde{D}_{13}P_y^\Lambda) - N_x^\Lambda
\end{aligned}
\tag{3.23}
$$

In Eq. (3.23), y_1, y_2, y_3 and y_4 are the y-coordinates of PZT patches as shown in Fig. 3.1, and in this equation and in the sequel, $N_\Lambda(i)$ is the i th component of the vector $\{N_\Lambda\}$. (See Eq. (3.22))

$$
\begin{aligned}
V_y = \int_{-\frac{b}{2}}^{\frac{b}{2}} N_{xy} dy &= \int_{-\frac{b}{2}}^{\frac{b}{2}} (\overline{D}_{12}\varepsilon_1^0 + \overline{D}_{22}\varepsilon_6^0 + \overline{D}_{23}\varepsilon_1^1 + \overline{D}_{24}\varepsilon_6^1 + \overline{D}_{25}\varepsilon_1^2)\, dy \\
&\qquad - \int_{y_1}^{y_2} N_\Lambda(2)\, dy - \int_{y_3}^{y_4} N_\Lambda(2)\, dy \\
&= b\overline{D}_{12}(\bar{u}_0{}') + b\overline{D}_{22}(\beta + \bar{v}_0{}') + b\overline{D}_{23}(-w_{b0}{}'') + 2b\overline{D}_{24}(-\tau') \\
&\qquad + b\overline{D}_{25}(-w_{s0}{}'') - (y_2 - y_1)\,((\tilde{D}_{21}N_y^\Lambda + \tilde{D}_{22}M_y^\Lambda + \tilde{D}_{23}P_y^\Lambda) - N_{xy}^\Lambda) \\
&\qquad - \int_{y_3}^{y_4} ((\tilde{D}_{21}N_y^\Lambda + \tilde{D}_{22}M_y^\Lambda + \tilde{D}_{23}P_y^\Lambda) - N_{xy}^\Lambda)\, dy
\end{aligned}
\tag{3.24}
$$

$$V_z = \int_0^b Q_x dy = \int_0^b \overset{\circ}{D}_{55}\varepsilon_5^0 dy \cong \int_0^b \overset{\circ}{D}_{55} w_{s0}' dy = b\overset{\circ}{D}_{55} w_{s0}' \tag{3.25}$$

$$M_{yb} = \int_{-\frac{b}{2}}^{\frac{b}{2}} M_x dy = \int_{-\frac{b}{2}}^{\frac{b}{2}} (\overline{D}_{13}\varepsilon_1^0 + \overline{D}_{23}\varepsilon_6^0 + \overline{D}_{33}\varepsilon_1^1 + \overline{D}_{34}\varepsilon_6^1 + \overline{D}_{35}\varepsilon_1^2)\, dy$$

$$-\int_{y_1}^{y_2} N_\Lambda(3)\, dy - \int_{y_3}^{y_4} N_\Lambda(3)\, dy$$

$$= b\overline{D}_{13}(\bar{u}_0') + b\overline{D}_{23}(\beta + \bar{v}_0') + b\overline{D}_{33}(-w_{b0}'') + 2b\overline{D}_{34}(-\tau')$$

$$+ b\overline{D}_{35}(-w_{s0}'') - (y_2 - y_1)\,((\tilde{D}_{31}N_y^\Lambda + \tilde{D}_{32}M_y^\Lambda + \tilde{D}_{33}P_y^\Lambda) - M_x^\Lambda)$$

$$-(y_4 - y_3)\,((\tilde{D}_{31}N_y^\Lambda + \tilde{D}_{32}M_y^\Lambda + \tilde{D}_{33}P_y^\Lambda) - M_x^\Lambda) \tag{3.26}$$

$$M_{ys} = \int_{-\frac{b}{2}}^{\frac{b}{2}} P_x dy = \int_{-\frac{b}{2}}^{\frac{b}{2}} (\overline{D}_{15}\varepsilon_1^0 + \overline{D}_{25}\varepsilon_6^0 + \overline{D}_{35}\varepsilon_1^1 + \overline{D}_{45}\varepsilon_6^1 + \overline{D}_{55}\varepsilon_1^2)\, dy$$

$$-\int_{y_1}^{y_2} N_\Lambda(5)\, dy - \int_{y_3}^{y_4} N_\Lambda(5)\, dy$$

$$= b\overline{D}_{15}(\bar{u}_0') + b\overline{D}_{25}(\beta + \bar{v}_0') + b\overline{D}_{35}(-w_{b0}'') + 2b\overline{D}_{45}(-\tau')$$

$$+ b\overline{D}_{55}(-w_{s0}'') - (y_2 - y_1)\,((\tilde{D}_{51}N_y^\Lambda + \tilde{D}_{52}M_y^\Lambda + \tilde{D}_{53}P_y^\Lambda) - P_x^\Lambda)$$

$$-(y_4 - y_3)\,((\tilde{D}_{51}N_y^\Lambda + \tilde{D}_{52}M_y^\Lambda + \tilde{D}_{53}P_y^\Lambda) - P_x^\Lambda) \tag{3.27}$$

$$M_z = \int_{-\frac{b}{2}}^{\frac{b}{2}} yN_x dy = \int_{-\frac{b}{2}}^{\frac{b}{2}} y\,(\overline{D}_{11}\varepsilon_1^0 + \overline{D}_{12}\varepsilon_6^0 + \overline{D}_{13}\varepsilon_1^1 + \overline{D}_{14}\varepsilon_6^1 + \overline{D}_{15}\varepsilon_1^2)\,dy$$

$$-\int_{y_1}^{y_2} yN_\Lambda(1)\,dy - \int_{y_3}^{y_4} yN_\Lambda(1)\,dy$$

$$= \frac{1}{12}b^3\overline{D}_{11}(\beta') + \frac{1}{12}b^3\overline{D}_{13}(-\tau'')$$

$$-\frac{1}{2}(y_2^2 - y_1^2)\,((\tilde{D}_{11}N_y^\Lambda + \tilde{D}_{12}M_y^\Lambda + \tilde{D}_{13}P_y^\Lambda) - N_x^\Lambda)$$

$$-\frac{1}{2}(y_4^2 - y_3^2)\,((\tilde{D}_{11}N_y^\Lambda + \tilde{D}_{12}M_y^\Lambda + \tilde{D}_{13}P_y^\Lambda) - N_x^\Lambda) \tag{3.28}$$

$$B = \int_{-\frac{b}{2}}^{\frac{b}{2}} yM_x dy = \int_{-\frac{b}{2}}^{\frac{b}{2}} y\,(\overline{D}_{13}\varepsilon_1^0 + \overline{D}_{23}\varepsilon_6^0 + \overline{D}_{33}\varepsilon_1^1 + \overline{D}_{34}\varepsilon_6^1 + \overline{D}_{35}\varepsilon_1^2)\,dy$$

$$-\int_{y_1}^{y_2} yN_\Lambda(3)\,dy - \int_{y_3}^{y_4} yN_\Lambda(3)\,dy$$

$$= \frac{1}{12}b^3\overline{D}_{13}(\beta') + \frac{1}{12}b^3\overline{D}_{33}(-\tau'')$$

$$-\frac{1}{2}(y_2^2 - y_1^2)\,((\tilde{D}_{31}N_y^\Lambda + \tilde{D}_{32}M_y^\Lambda + \tilde{D}_{33}P_y^\Lambda) - M_x^\Lambda)$$

$$-\frac{1}{2}(y_4^2 - y_3^2)\,((\tilde{D}_{31}N_y^\Lambda + \tilde{D}_{32}M_y^\Lambda + \tilde{D}_{33}P_y^\Lambda) - M_x^\Lambda) \tag{3.29}$$

$$T_s = 2\int_{-\frac{b}{2}}^{\frac{b}{2}} M_{xy} dy = 2\int_{-\frac{b}{2}}^{\frac{b}{2}} (\overline{D}_{14}\varepsilon_1^0 + \overline{D}_{24}\varepsilon_6^0 + \overline{D}_{34}\varepsilon_1^1 + \overline{D}_{44}\varepsilon_6^1 + \overline{D}_{45}\varepsilon_1^2)\,dy$$

$$-2\int_{y_1}^{y_2} N_\Lambda(4)\,dy - 2\int_{y_3}^{y_4} N_\Lambda(4)\,dy$$

$$= 2b\overline{D}_{14}(\bar{u}_0') + 2b\overline{D}_{24}(\beta + \bar{v}_0') + (2b\overline{D}_{34}(-w_{b0}''))) + 4b\overline{D}_{44}(-\tau')$$

$$+ 2b\overline{D}_{45}(-w_{s0}'') - 2(y_2 - y_1)\,((\tilde{D}_{41}N_y^\Lambda + \tilde{D}_{42}M_y^\Lambda + \tilde{D}_{43}P_y^\Lambda) - M_{xy}^\Lambda)$$

$$-2(y_4 - y_3)\,((\tilde{D}_{41}N_y^\Lambda + \tilde{D}_{42}M_y^\Lambda + \tilde{D}_{43}P_y^\Lambda) - M_{xy}^\Lambda) \tag{3.30}$$

Now, the stiffness matrix for the beam theory can be assembled by combining Eqs. (3.23) to (3.30) in the matrix form.

$$
\begin{bmatrix} P \\ V_y \\ V_z \\ M_{yb} \\ M_{ys} \\ M_z \\ B \\ T_s \end{bmatrix}
=
\begin{bmatrix}
\hat{D}_{11} & \hat{D}_{12} & 0 & \hat{D}_{14} & \hat{D}_{15} & 0 & 0 & \hat{D}_{18} \\
\hat{D}_{12} & \hat{D}_{22} & 0 & \hat{D}_{24} & \hat{D}_{25} & 0 & 0 & \hat{D}_{28} \\
0 & 0 & \hat{D}_{33} & 0 & 0 & 0 & 0 & 0 \\
\hat{D}_{14} & \hat{D}_{24} & 0 & \hat{D}_{44} & \hat{D}_{45} & 0 & 0 & \hat{D}_{48} \\
\hat{D}_{15} & \hat{D}_{25} & 0 & \hat{D}_{45} & \hat{D}_{55} & 0 & 0 & \hat{D}_{58} \\
0 & 0 & 0 & \hat{D}_{46} & 0 & \hat{D}_{66} & \hat{D}_{67} & 0 \\
0 & 0 & 0 & \hat{D}_{47} & 0 & \hat{D}_{67} & \hat{D}_{77} & 0 \\
\hat{D}_{18} & \hat{D}_{28} & 0 & \hat{D}_{48} & \hat{D}_{58} & 0 & 0 & \hat{D}_{88}
\end{bmatrix}
\begin{bmatrix} \bar{u}_0{}' \\ \beta + \bar{v}_0{}' \\ w_{s0}{}' \\ -w_{b0}{}'' \\ -w_{s0}{}'' \\ \beta' \\ -\tau'' \\ -\tau' \end{bmatrix}
-
\begin{bmatrix} P^{\Lambda} \\ V_y^{\Lambda} \\ V_z^{\Lambda} \\ M_{yb}^{\Lambda} \\ M_{ys}^{\Lambda} \\ M_z^{\Lambda} \\ B^{\Lambda} \\ T_s^{\Lambda} \end{bmatrix}
\tag{3.31}
$$

where

$$
\begin{aligned}
&\hat{D}_{11} = b\bar{D}_{11} && \hat{D}_{22} = b\bar{D}_{22} && \hat{D}_{44} = b\bar{D}_{33} && \hat{D}_{55} = b\bar{D}_{55} \\
&\hat{D}_{12} = b\bar{D}_{12} && \hat{D}_{24} = b\bar{D}_{23} && \hat{D}_{45} = b\bar{D}_{35} && \hat{D}_{58} = 2b\bar{D}_{45} \\
&\hat{D}_{14} = b\bar{D}_{13} && \hat{D}_{25} = b\bar{D}_{25} && \hat{D}_{48} = 2b\bar{D}_{34} && \hat{D}_{66} = \frac{1}{12}b^3\bar{D}_{11} \\
&\hat{D}_{15} = b\bar{D}_{15} && \hat{D}_{28} = 2b\bar{D}_{24} && \hat{D}_{77} = \frac{1}{12}b^3\bar{D}_{33} && \hat{D}_{67} = \frac{1}{12}b^3\bar{D}_{13} \\
&\hat{D}_{18} = 2b\bar{D}_{14} && \hat{D}_{33} = b\overset{\circ}{D}_{55} && \hat{D}_{88} = 4b\bar{D}_{44}
\end{aligned}
\tag{3.32}
$$

and

$$P^{\Lambda} = (y_2 - y_1)\,((\tilde{D}_{11}N_y^{\Lambda} + \tilde{D}_{12}M_y^{\Lambda} + \tilde{D}_{13}P_y^{\Lambda}) - N_x^{\Lambda})$$
$$+ (y_4 - y_3)\,((\tilde{D}_{11}N_y^{\Lambda} + \tilde{D}_{12}M_y^{\Lambda} + \tilde{D}_{13}P_y^{\Lambda}) - N_x^{\Lambda})$$

$$V_y^{\Lambda} = (y_2 - y_1)\,((\tilde{D}_{21}N_y^{\Lambda} + \tilde{D}_{22}M_y^{\Lambda} + \tilde{D}_{23}P_y^{\Lambda}) - N_{xy}^{\Lambda})$$
$$+ (y_4 - y_3)\,((\tilde{D}_{21}N_y^{\Lambda} + \tilde{D}_{22}M_y^{\Lambda} + \tilde{D}_{23}P_y^{\Lambda}) - N_{xy}^{\Lambda})$$

$$V_z^{\Lambda} = 0$$

$$M_{yb}^{\Lambda} = (y_2 - y_1)\,((\tilde{D}_{31}N_y^{\Lambda} + \tilde{D}_{32}M_y^{\Lambda} + \tilde{D}_{33}P_y^{\Lambda}) - M_x^{\Lambda})$$
$$+ (y_4 - y_3)\,((\tilde{D}_{31}N_y^{\Lambda} + \tilde{D}_{32}M_y^{\Lambda} + \tilde{D}_{33}P_y^{\Lambda}) - M_x^{\Lambda})$$

$$M_{ys}^{\Lambda} = (y_2 - y_1)\,((\tilde{D}_{51}N_y^{\Lambda} + \tilde{D}_{52}M_y^{\Lambda} + \tilde{D}_{53}P_y^{\Lambda}) - P_x^{\Lambda})$$
$$+ (y_4 - y_3)\,((\tilde{D}_{51}N_y^{\Lambda} + \tilde{D}_{52}M_y^{\Lambda} + \tilde{D}_{53}P_y^{\Lambda}) - P_x^{\Lambda})$$

$$M_z^{\Lambda} = \frac{1}{2}(y_2^2 - y_1^2)\,((\tilde{D}_{11}N_y^{\Lambda} + \tilde{D}_{12}M_y^{\Lambda} + \tilde{D}_{13}P_y^{\Lambda}) - N_x^{\Lambda})$$
$$+ \frac{1}{2}(y_4^2 - y_3^2)\,((\tilde{D}_{11}N_y^{\Lambda} + \tilde{D}_{12}M_y^{\Lambda} + \tilde{D}_{13}P_y^{\Lambda}) - N_x^{\Lambda})$$

$$B^{\Lambda} = \frac{1}{2}(y_2^2 - y_1^2)\,((\tilde{D}_{31}N_y^{\Lambda} + \tilde{D}_{32}M_y^{\Lambda} + \tilde{D}_{33}P_y^{\Lambda}) - M_x^{\Lambda})$$
$$+ \frac{1}{2}(y_4^2 - y_3^2)\,((\tilde{D}_{31}N_y^{\Lambda} + \tilde{D}_{32}M_y^{\Lambda} + \tilde{D}_{33}P_y^{\Lambda}) - M_x^{\Lambda})$$

$$T_s^{\Lambda} = 2\,(y_2 - y_1)\,((\tilde{D}_{41}N_y^{\Lambda} + \tilde{D}_{42}M_y^{\Lambda} + \tilde{D}_{43}P_y^{\Lambda}) - P_{xy}^{\Lambda})$$
$$+ 2\,(y_4 - y_3)\,((\tilde{D}_{41}N_y^{\Lambda} + \tilde{D}_{42}M_y^{\Lambda} + \tilde{D}_{43}P_y^{\Lambda}) - P_{xy}^{\Lambda}) \qquad (3.33)$$

3.4 Induced force by PZT

In the previous section, the beam resultants which can be induced by PZT patches are determined. These induced resultants can not be activated by any configuration of PZT patches. A rectangular PZT patch, with a material coordinate system that coincides with the beam coordinate system, as explained in Section 2.4., is the interest of this study. Since resultants N_{xy} and M_{xy} can not be induced with this configuration, then for substrates without shear-extension couplings, $\overline{Q}16$ and $\overline{Q}26$ are equal to zero.

$$V_y^{\Lambda} = 0 \qquad\qquad T_s^{\Lambda} = 0 \tag{3.34}$$

Eq. (3.34) is applicable to the isotropic substrate and to the specially orthotropic substrate. For an anisotropic substrate, which has off-axis fibers, all the elements in D are nonzero thus Eq. (3.34) does not apply.

The cross-section of a beam of isotropic material or specially orthotropic material with rectangular PZT patches bonded on the top and bottom is shown in Fig. 3.3. A given magnitude of voltage with polarities shown in Fig. 3.3, will induce only axial resultant P^{Λ}

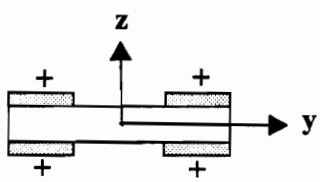

Fig. 3.3 The cross-section of a beam which induce the axial force only.

on this beam. For a given voltage, the maximum axial force will be induced when the top and bottom surfaces of the beam are completely covered by PZT material, the patch width or total of two patch widths is equal to the beam width.

Patch the configurations which induce the bending moments about the y-axis, $M^{\Lambda}{}_{yb}$ and $M^{\Lambda}{}_{ys}$, without other inducing resultants are shown in Fig. 3.4. The magnitudes of

given voltages have to be same and the polarities need to be opposite between the top and

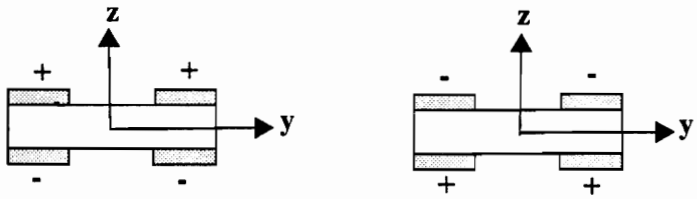

Fig. 3.4 The cross-section of a beam which induces the bending only.

the bottom patches. The maximum bending moments are induced with the patches of the half width of the beam width. Since the polarities are the same for the each surface, total of two patches of the same width as the beam, one on the top and the other on the bottom, produces the maximum bending.

The bimoment is induced by the configurations shown in Fig. 3.5 with given voltages of the same magnitude and the polarities shown. The maximum bimoment can be induced with the width of the patches equal to the half width of the beam.

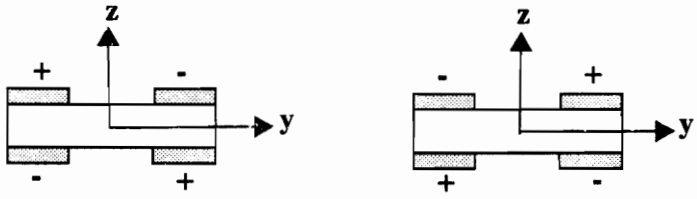

Fig. 3.5 The cross-section of a beam which induces the bimoment only.

3.5 Governing equations and boundary conditions

Consider prescribed tractions of p_x, p_y, and p_z acting on the upper surface of the beam in the positive x-, y-, and z-direction, respectively, as shown in Fig. 3.6.

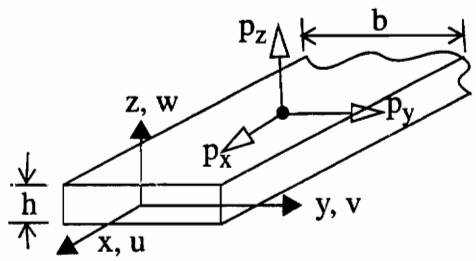

Fig. 3.6 The prescribed tractions, p_x, p_y, and p_z on a beam.

The external virtual work by the tractions is

$$\delta W_{ext} = \int_0^L \int_{-\frac{b}{2}}^{\frac{b}{2}} (p_x \delta u + p_y \delta v + p_z \delta w)\Big|_{z=\frac{h}{2}} dy dx \tag{3.35}$$

Using the displacement field given by Eqs. (3.5), the virtual displacement at z = h/2 can be found as

$$\begin{aligned}
\delta u &= \delta \bar{u}_0(x) + (\delta\beta(x))y - \frac{h}{2}((\delta\tau(x)')y + \delta w_{b0}(x)') - \frac{h}{6}(\delta w_{s0}(x)') \\
\delta v &= \delta \bar{v}_0(x) - \frac{h}{2}\delta(\tau(x)) \\
\delta w &= (\delta\tau(x))y + \delta(w_{b0}(x) + w_{s0}(x))
\end{aligned} \tag{3.36}$$

Substituting Eq. (3.36) into Eq. (3.35), and integrating with respect to y, results in

$$\begin{aligned}
\delta W_{ext} = \int_0^L (q_x \delta \bar{u}_0 + q_y \delta \bar{v}_0 - q_z(-\delta(w_{b0} + w_{s0})) - t(-\delta\tau) - b(-\delta\tau') \\
+ m_{yb}(-\delta w_{b0}') + m_{ys}(-\delta w_{s0}') + m_z \delta\beta)\, dx
\end{aligned} \tag{3.37}$$

where

$$q_x = \int_{-\frac{b}{2}}^{\frac{b}{2}} p_x dy \qquad q_y = \int_{-\frac{b}{2}}^{\frac{b}{2}} p_y dy \qquad q_z = \int_{-\frac{b}{2}}^{\frac{b}{2}} p_z dy$$

$$t = \int_{-\frac{b}{2}}^{\frac{b}{2}} (p_z y - \frac{h}{2} p_y)\, dy \qquad b = -\frac{h}{2}\int_{-\frac{b}{2}}^{\frac{b}{2}} p_x y dy = -\frac{h}{2} m_z \qquad m_z = \int_{-\frac{b}{2}}^{\frac{b}{2}} p_x y dy$$

$$m_{yb} = \frac{h}{2}\int_{-\frac{b}{2}}^{\frac{b}{2}} p_x dy = \frac{h}{2} q_x \qquad m_{ys} = \frac{h}{6}\int_{-\frac{b}{2}}^{\frac{b}{2}} p_x dy = \frac{h}{6} q_x \tag{3.38}$$

Equilibrium is imposed by the principal of virtual work, which is

$$\delta W_{int} = \delta W_{ext} \tag{3.39}$$

for every kinematically admissible virtual field. The internal virtual work for the beam is given by Eq. (3.9) and the external virtual work is given by Eq. (3.37). Equating these expressions according to Eq. (3.39) and integrating by parts gives

$$\begin{aligned}
&\int_0^L (-P'\delta\bar{u}_0 - V_y'\delta\bar{v}_0 + (-V_z' + M_{ys}'')\,(\delta w_{s0}) + M_{yb}''(\delta w_{b0}) + (B'' - T_s')\,(\delta\tau) \\
&\qquad - (M_z' + V_y)\,\delta\beta\,)\,dx + [P\delta\bar{u}_0 + V_y\delta\bar{v}_0 + (V_z - M_{ys}')\,(\delta w_{s0}) + M_{ys}(-\delta w_{s0}') \\
&\qquad\qquad + M_{yb}'(\delta w_{b0}) - M_{yb}(-\delta w_{b0}') + (B' + T_s)\,(\delta\tau) - B(-\delta\tau') + M_z\delta\beta\,]\,|_0^L \\
&= \int_0^L (q_x\delta\bar{u}_0 + q_y\delta\bar{v}_0 + q_z\delta\,(w_{b0} + w_{s0}) + (t + b')\,(\delta\tau) + m_{yb}'(\delta w_{b0}) \\
&\qquad + m_{ys}'(\delta w_{s0}) + m_z\delta\beta\,)\,dx + [-m_{yb}(\delta w_{b0}) - m_{ys}(\delta w_{s0}) - b\,(\delta\tau)\,]\,|_0^L
\end{aligned} \tag{3.40}$$

Using the fundamental lemma of the calculus of variations, the equilibrium equations are

$$
\begin{aligned}
-P' &= q_x & -V_y' &= q_y & V_z'-M_{ys}'' &= -q_z - m_{ys}' \\
M_{yb}'' &= q_z + m_{yb}' & -B'' + T_s' &= -t-b' & M_z' + V_y &= -m_z
\end{aligned}
\tag{3.41}
$$

for 0 < x < L. Then, boundary conditions at x = 0 and x = L are to prescribe either the natural or essential boundary condition from following pairs.

$$
\begin{aligned}
&\textit{Natural or Essential} \\
&P \ \ or \ \ (\bar{u}_0) \\
&V_y \ \ or \ \ (\bar{v}_0) \\
&V_z + M_{ys}' - m_{ys} \ \ or \ \ w_{s0} \\
&M_{yb}' - m_{yb} \ \ or \ \ w_{b0} \\
&M_{yb} \ \ or \ \ (-w_{bo}') \\
&M_{ys} \ \ or \ \ (-w_{s0}') \\
&M_z \ \ or \ \ \beta \\
&B' - T_s - b \ \ or \ \ \tau \\
&B \ \ or \ \ (-\tau')
\end{aligned}
\tag{3.42}
$$

Thus, these are nine boundary conditions at each end point. For a finite element solution to be a Ritz analysis, the quantities in the nine essential boundary conditions must be continuous within and between elements. For a two-noded beam element this implies eighteen degrees of freedom are necessary.

4. *Finite element formulation*

The derivation of finite element equations are presented in this chapter. The coordinate system of an element is shown in Fig. 4.1. The length of an element, l_e, can be varied for each element. Let x be the global coordinate and $\bar{x}$ be a local coordinate. The node numbers indicated in Fig. 4.1 are the numbering convention in the local coordinate system.

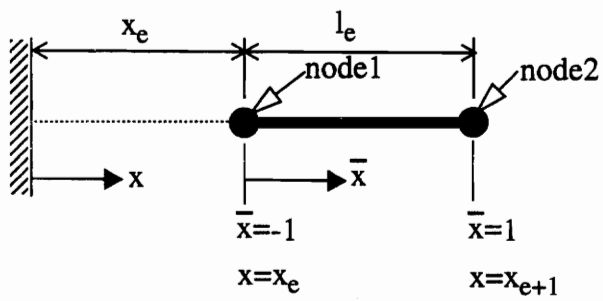

Fig. 4.1 The coordinate system of a beam element.

The relationship of x to $\bar{x}$ is

$$x = \frac{l_e}{2}\bar{x} + \frac{x_e + x_{e+1}}{2} \qquad , -1 \le \bar{x} \le 1 \tag{4.1}$$

In the global coordinate system, the nodes are numbered sequentially from one on left of the first element to N + 1 on the right of last element, where N is the number of elements.

4.1 Finite element equilibrium equations

Equilibrium is imposed by the principle of virtual work which states that the body is in equilibrium if

$$\delta W = \delta W_{int} - \delta W_{ext} = 0 \tag{4.2}$$

for all kinematically admissible displacements. For a beam subdivided into N elements, the internal and external virtual work terms are

$$\begin{aligned} \delta W_{int} &= \sum_{e=1}^{N} \left(\int_{-1}^{1} \{\delta\hat{\varepsilon}\}^T (\{P_{int}\} - \{P_\Lambda\}) \frac{1}{2} l_e dx \right) \\ \delta W_{ext} &= \sum_{e=1}^{N} \left(\int_{-1}^{1} \{\delta q\}^T \{P_e\} \frac{1}{2} l_e dx \right) \end{aligned} \tag{4.3}$$

in which $\{\varepsilon\}$ is a 9x1 vector of generalized strains, $\{P_{int}\}$ is a 9x1 vector of internal generalized forces, $\{P_\Lambda\}$ is a 9x1 vector of equivalent force vector due to actuator strains, $\{q\}$ is a 9x1 vector of generalized displacements, and $\{P_e\}$ is a 9x1 vector of external forces

due to distributed loads. These vectors are

$$
\begin{aligned}
\{\hat{\varepsilon}\} &= \{\overline{u_0}', (\beta + \overline{v_0}'), w_{s0}', -w_{b0}'', \beta', -\tau'', -\tau'\}^T \\
\{P_{int}\} &= \{P, V_y, V_z, M_{yb}, M_{ys}, M_z, B, T_s\}^T \\
\{P^\Lambda\} &= \{P^\Lambda, V_y^\Lambda, V_z^\Lambda, M_{yb}^\Lambda, M_{ys}^\Lambda, M_z^\Lambda, B^\Lambda, T_s^\Lambda\}^T \\
\{q\} &= \{\overline{u_0}, \overline{v_0}, w_{b0}, w_{b0}', w_{s0}, w_{s0}', \beta, \tau, \tau'\}^T \\
\{P_e\} &= \{q_x, q_y, q_z, -m_{yb}, q_z, -m_{ys}, m_z, b, t\}^T
\end{aligned}
\tag{4.4}
$$

The 6x1 vector $\{u\}$ of displacements is defined by

$$\{u\} = \{\overline{u_0}, \overline{v_0}, w_{b0}, w_{s0}, \beta, \tau\} \tag{4.5}$$

Consequently, the generalized displacement vector is given by

$$\{q\} = [L_1]\,\{u\} \tag{4.6}$$

where $[L_1]$ is a 9x6 operator matrix. The strains in terms of the generalized displacements are

$$\{\hat{\varepsilon}\} = [L_2]\,\{q\} \tag{4.7}$$

where $[L_2]$ is a 9x9 operator matrix. The strain-displacement equations are

$$\{\hat{\varepsilon}\} = [L]\,\{u\} \tag{4.8}$$

where

$$[L] = [L_2]\,[L_1] \tag{4.9}$$

which when written in full is

$$
[L] = \begin{bmatrix}
\frac{\partial}{\partial x} & 0 & 0 & 0 & 0 & 0 \\
0 & \frac{\partial}{\partial x} & 0 & 0 & 0 & 0 \\
0 & 0 & 0 & \frac{\partial}{\partial x} & 0 & 0 \\
0 & 0 & -\frac{\partial^2}{\partial x^2} & 0 & 0 & 0 \\
0 & 0 & 0 & -\frac{\partial^2}{\partial x^2} & 0 & 0 \\
0 & 0 & 0 & 0 & \frac{\partial}{\partial x} & 0 \\
0 & 0 & 0 & 0 & 0 & -\frac{\partial^2}{\partial x^2} \\
0 & 0 & 0 & 0 & 0 & -\frac{\partial^2}{\partial x^2}
\end{bmatrix} \tag{4.10}
$$

For a compatible element, the displacement functions for an element need to satisfy continuity conditions. Based on the derivatives of the displacements appearing in the strain vector, components $\bar{u}_0$, $\bar{v}_0$, and β should have C^0- continuity, while components w_{b0}, w_{s0}, and τ should have c^1- continuity. This continuity requirement translates into the fact that the generalized displacement vector should be continues within and between elements. Hence, the nodal degrees of freedom are the generalized displacement vector evaluated at nodes 1 and 2. Let $\{q_1\}$ be the generalized displacement at node 1, and $\{q_2\}$ be the generalized displacement at node 2. Define an 18x1 nodal displacement vector $\{a\}$ by

$$
\{a\} = \begin{Bmatrix} q_1 \\ q_2 \end{Bmatrix} \tag{4.11}
$$

The displacement field within the element is written as

$$\{u(\bar{x})\} = [N(\bar{x})]\{a\} \tag{4.12}$$

in which $[N(\bar{x})]$ is the 6x18 shape function matrix. The strains are

$$\{\hat{\varepsilon}\} = [L]\{u\} = [B(\bar{x})]\{a\} \tag{4.13}$$

in which the 9x18 strain-displacement matrix is

$$[B(\bar{x})] = [L][N] \tag{4.14}$$

From Chapter 3, the constitutive law is

$$\{P_{int}\} = [\hat{D}]\{\hat{\varepsilon}\} \tag{4.15}$$

where [D] denotes the 9x9 beam stiffness matrix. Substituting Eq. (4.7)-(4.15) into the principle of virtual work for generic element we get

$$0 = \sum_{element}\left(\int_{-1}^{1}\{\delta a\}^T[B]^T[\hat{D}][B]\frac{l_e}{2}d\bar{x}\{a\} - \int_{-1}^{1}\{\delta a\}^T[B]^T\{P_\Lambda\}\frac{l_e}{2}d\bar{x} - \int_{-1}^{1}\{\delta a\}^T[L,N]^T\{P_e\}\frac{l_e}{2}d\bar{x}\right) \tag{4.16}$$

or

$$\sum_{elements}\{\delta a\}\,[\,[K^e]\{a^e\} - \{F^e\} - \{F^e_\Lambda\}\,] = 0 \tag{4.17}$$

where

$$[K^e] = \int_{-1}^{1} [B]^T [\hat{D}] [B] \frac{l_e}{2} d\bar{x} \qquad \{F^e\} = \int_{-1}^{1} [L, N]^T \{P_e\} \frac{l_e}{2} d\bar{x}$$

$$\{F^e_\Lambda\} = c \int_{-1}^{1} [B]^T \{P_\Lambda\} \frac{l_e}{2} d\bar{x}$$

$$c = \begin{cases} 0 & \textit{if the element has no PZT actuator} \\ 1 & \textit{if the element has a PZT actoator} \end{cases} \tag{4.18}$$

For C^0-continuity, Lagrange interpolation polynomials, L_1 and L_2, are used for $(\bar{u}_0)$, $(\bar{v}_0)$, and β. These polynomials are

$$L_1 = -\frac{1}{2}\bar{x} + \frac{1}{2} \qquad L_2 = \frac{1}{2}\bar{x} + \frac{1}{2} \tag{4.19}$$

where $\bar{x}$ is a local coordinate. The remaining degrees of freedom, (w_b), (w_b'), (w_s), (w_s'), τ, and τ', are interpolated by the following Hermitian interpolation polynomials to achieve C^1-continuity. These polynomials are

$$H_1^{(e)} = 1 - 3\left(\frac{\bar{x}}{l_e}\right)^2 + 2\left(\frac{\bar{x}}{l_e}\right)^3 \qquad H_3^{(e)} = 3\left(\frac{\bar{x}}{l_e}\right)^2 - 2\left(\frac{\bar{x}}{l_e}\right)^3$$

$$H_2^{(e)} = \bar{x}\left(1 - \frac{\bar{x}}{l_e}\right)^2 \qquad H_4^{(e)} = \bar{x}\left[\left(\frac{\bar{x}}{l_e}\right)^2 - \frac{\bar{x}}{l_e}\right] \tag{4.20}$$

where l_e is a length of an element.

Using Eqs. (4.19) and (4.20), the shape function matrix in Eq. (4.13) can be written as

$$[N] = \begin{bmatrix} L_1 & 0 & 0 & 0 & 0 & 0 & 0 & 0 & 0 & L_2 & 0 & 0 & 0 & 0 & 0 & 0 & 0 & 0 \\ 0 & L_1 & 0 & 0 & 0 & 0 & 0 & 0 & 0 & 0 & L_2 & 0 & 0 & 0 & 0 & 0 & 0 & 0 \\ 0 & 0 & H_1 & H_2 & 0 & 0 & 0 & 0 & 0 & 0 & 0 & H_3 & H_4 & 0 & 0 & 0 & 0 & 0 \\ 0 & 0 & 0 & 0 & H_1 & H_2 & 0 & 0 & 0 & 0 & 0 & 0 & 0 & H_3 & H_4 & 0 & 0 & 0 \\ 0 & 0 & 0 & 0 & 0 & 0 & L_1 & 0 & 0 & 0 & 0 & 0 & 0 & 0 & 0 & L_2 & 0 & 0 \\ 0 & 0 & 0 & 0 & 0 & 0 & 0 & H_1 & H_2 & 0 & 0 & 0 & 0 & 0 & 0 & 0 & H_3 & H_4 \end{bmatrix} \tag{4.21}$$

4.2 Modeling of bonded PZT

In the analytical modeling, the assumption of perfect bonding of the PZT patches to the substrate, was taken. A perfectly bonded PZT is the limiting case of an infinitely stiff and very thin adhesive layer. This limiting case was quantified in Ref. 24 by the shear lag parameter approaching infinity. The shear lag parameter, Γ, indicates the effectiveness of the shear transfer and is defined[24] as

$$\Gamma^2 = \frac{\overline{G}\theta_s}{\bar{t}_s^2}\left(\frac{\psi + \alpha}{\psi}\right) \tag{4.22}$$

where $\overline{G}$ is the modulus ratio of adhesive layer to piezoelectric, θ_s is the thickness ratio of adhesive layer to piezoelectric, and $\bar{t}_s$ is the nondimensional adhesive thickness. Parameter α is the substructure equilibrium parameter, which is equal to 2 for extension case and 6 for bending case. The effective stiffness ratio in Eq. (4.22) is

$$\psi = \frac{E_B t_B}{E_C t_C} \tag{4.23}$$

where E_B is Young's modulus of the substructure, t_B is the thickness of the substructure, E_c is Young's modulus of the PZT actuator, and t_c is the thickness of the PZT actuator.

The strains in piezoelectric and substructure for ψ=14.5 and α=6 are shown in Fig. 4.2, which is an aluminum bar 10 times thickness as thick as the PZT subject to bending. The curves above y = 0.3 in Fig. 4.2 correspond to strains in PZT actuator layer and the curves below correspond to strains in the substrate. Lambda is strain actuated by PZT

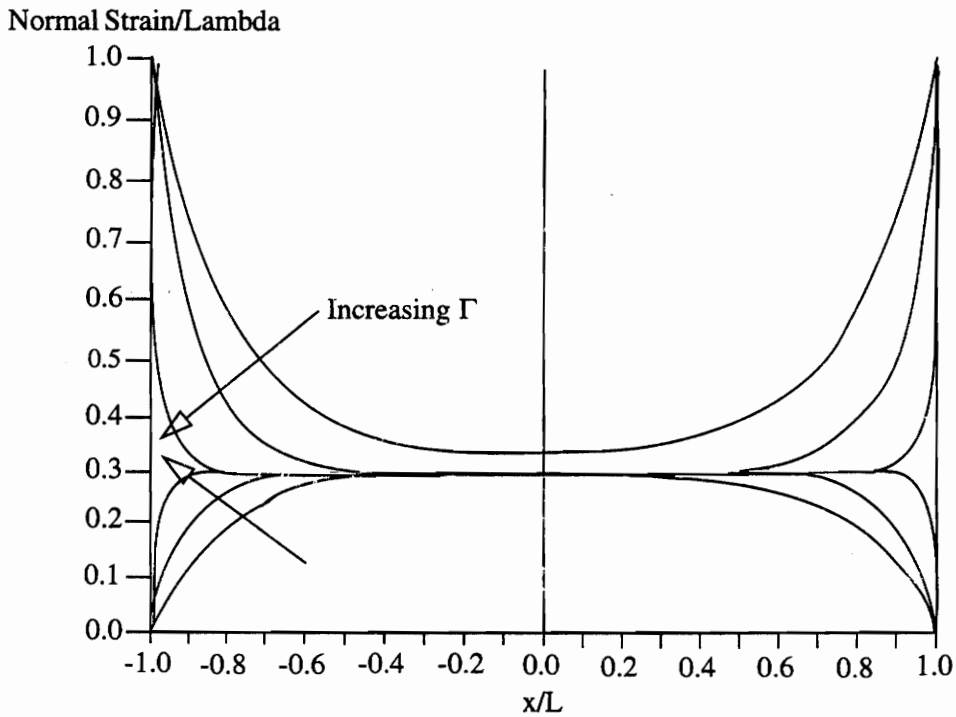

Fig. 4.2 Piezoelectric and substructure strains for various value of G.[24]

actuators. As the shear lag parameter increases, either large $\overline{G}$ or small $\bar{t}_s$, the shear transfer becomes localized to the ends of the PZT. For large Γ there is a sharp rise in the normal strain at the end of actuator indicating that the induced strain is transferred in an infinitesimal distance at the ends of actuators.

The induced force from the actuator is represented by the consistent load vector in the finite element implementation. However, we found that this representation does not cap-

ture the mechanics of the load transfer from the actuator to the substrate. An example of a cantilever beam with PZT on the top and bottom surfaces is used to illustrate that using the consistent load vector is not very good. Equal and opposite polarities are applied to the PZT's on top and bottom of the beam to cause bending. Thirty-nine finite elements are used to span the length L = 3.05 m of the beam. Equally spaced elements are used in one model, denoted as Mesh 1. An exponentially spaced mesh is used in the second model, denoted as Mesh 2. In Mesh 2 the elements are very short near the tip of the beam and increase progressively in length in a exponential manner from tip to root. The transverse deflections are compared in Fig. 4.3. The exponentially spaced mesh results in a larger tip deflection than the equally spaced mesh. The correct tip deflection in this case is -0.1038E-5 meters. Clearly both FE models using a consistent load vector are very much in error. However, Mesh 2 gives better results than Mesh 1. Apparently it will take many more short length elements at the end of the actuator to capture the load transfer properly if a consistent load vector is used.

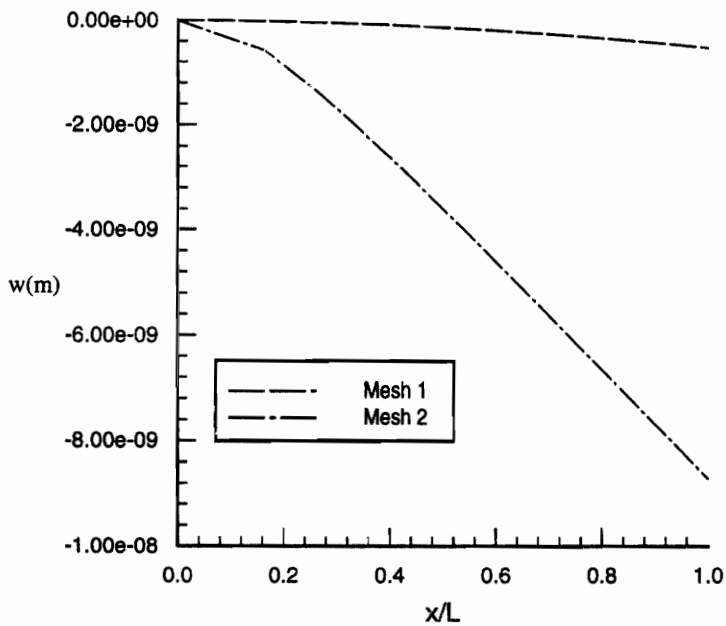

Fig. 4.3 Comparison of the transverse displacements.

In this study, a consistent load vector for the induced strains in the PZT actuator was not used in the finite element implementation, because the element strain distributions do not accurately capture the exponential behavior exhibited by adhesively bonded actuators unless a large number of small length elements are used. For very stiff and thin bonded adhesive layer, the transfer of axial strain from the actuator to the substrate by shearing of the adhesive occurs in a narrow boundary layer near the ends of actuator. In the limit of the perfectly bonded actuator as assumed here, we can model this effect by simply calculating the induced beam resultants given by and applying them to the element nodes coinciding with the ends of the actuator.

4.3 Minimum length of the PZT patch

The discussion in the last section showed that the transfer of axial strain from the actuator to the substrate occurs near the ends of the actuator. Under the perfectly bonded actuator assumption in the mathematical model, the induced strains or induced beam resultants are applied at the end points of the actuator. Hence, this mathematical modeling assumes the transfer of induced strain occurs over negligible length. In reality the actuator is bonded to the substrate with an adhesive of finite shear modulus and finite thickness. Thus, a minimum length for the actuator should be used to make the mathematical model physically realistic.

The problem of minimum length may be addressed by using the results from Rose[41], who discusses in detail the load transfer of a reinforcement material bonded to a strip, or substrate. This bonded reinforcement problem is shown in Fig. 4.4, along with a typical distribution of the shear stress in the adhesive. The half length of the reinforcement is

denoted by B, and the quantity $1/\beta$ is an estimate of the length over which the load is transferred from the strip to the reinforcement.

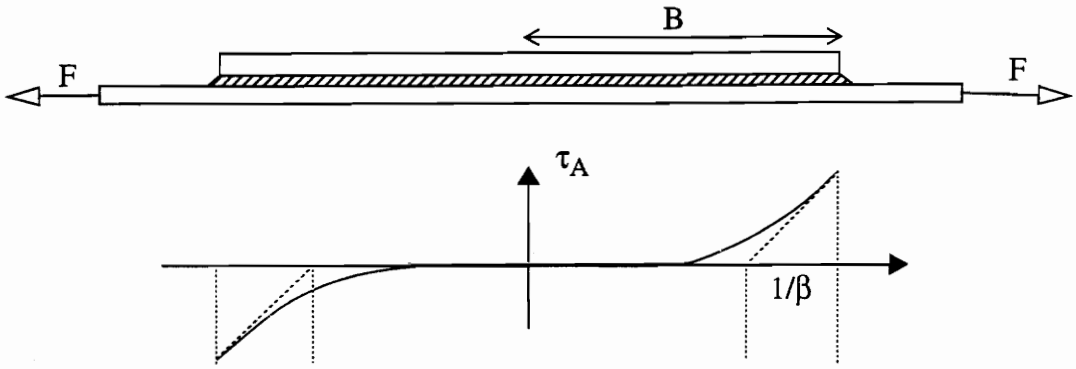

Fig. 4.4 A reinforcement configuration and shear transfer in the adhesive

The parameter β is given by

$$\beta^2 = \frac{G_A}{t_A}\{\frac{1}{E_p t_p} + \frac{1}{E_R t_r}\} \tag{4.24}$$

where subscripts "A", "P", and "R" denote adhesive layer, strip, and reinforcement, respectively. Table 4.1 shows the typical values for the variables in Eq. (4.24) for a bonded reinforcement problem.

Table 4.1 Typical material values.[41]

E_P	70 G Pa	t_P	3 mm
E_R	200 G Pa	t_R	1 mm
G_A	0.7 G Pa	t_A	0.2 mm

The length of the reinforcement (patch) needs to be

$$L = 2B > 2\,(\frac{1}{\beta}) \tag{4.25}$$

to satisfy the shear stress distribution assumed. For the data given in Table 4.1, this minimum length is 10.82 mm. The patch length of cases studied in Chapter 5 are checked by Eq. (4.25) using the adhesive material properties in Table 4.1, to ensure the PZT patches exceed this minimum length.

4.4 Computer code - SANDB

A FORTRAN program titled SANDB was written to implement the finite element formulation presented in this chapter. The stiffness matrix of a given beam and PZT actuators were calculated according to the method in the Chapter 2 and 3 depending on the material and dimensional data which is treated as input. Each component of the finite element stiffness matrix was analytically calculated by *Mathematica*, using the shape functions and the linear operators given in Section 4.3, and then integrated over the limit of -1 to 1 in the local coordinate. Equation (4.16) is solved by a linear equation solver given by Reddy[42]. The flow chart of the program is shown in Fig. 4.5.

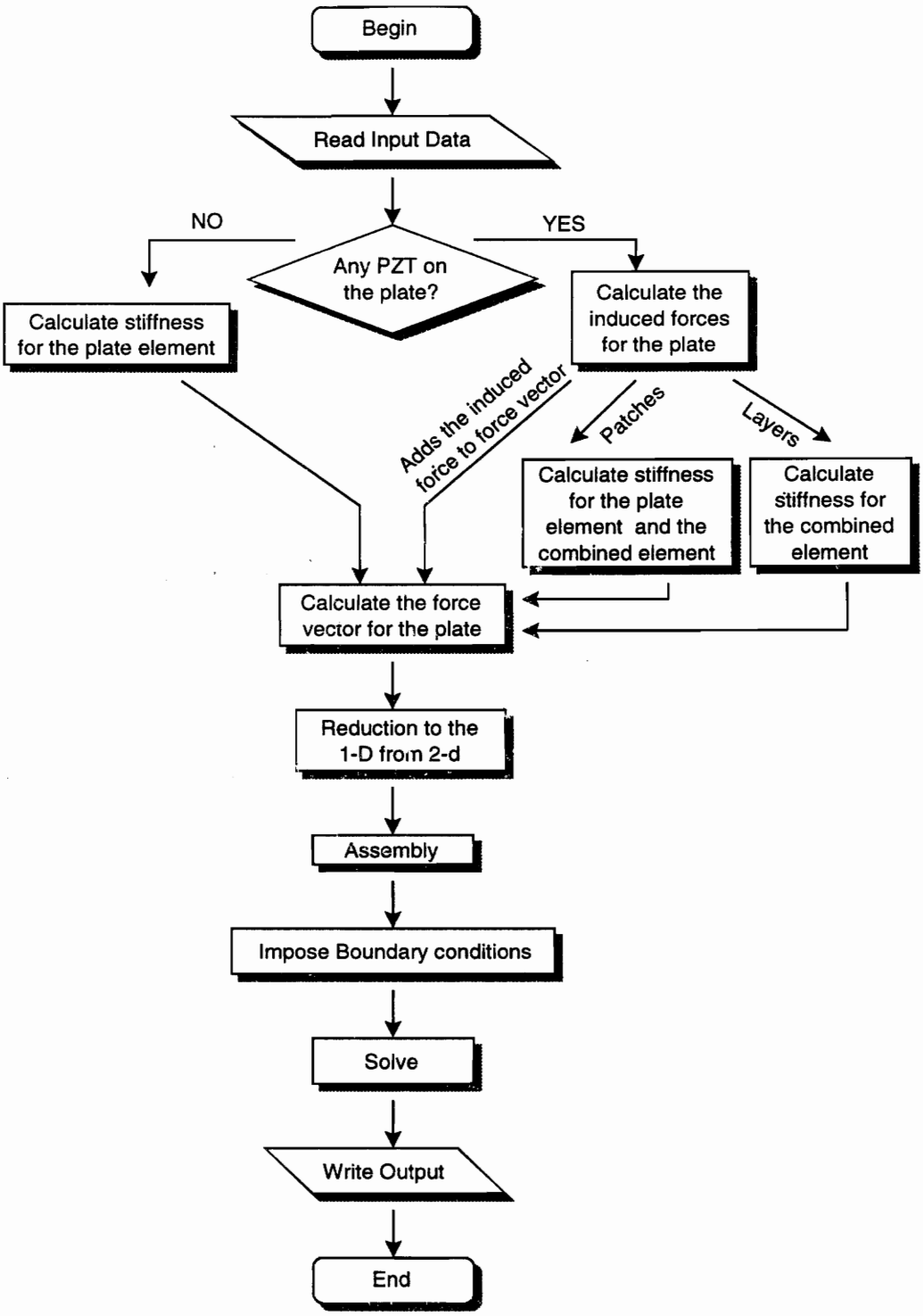

Fig. 4.5 The flow chart of SANDB.

5. Results and discussions

5.1 Verifications of structural model

5.1.1 Comparison with exact solution

As the first step in verifying the model very simple problems for which the exact solutions are easily calculated were solved by SANDB. An isotropic homogeneous cantilever

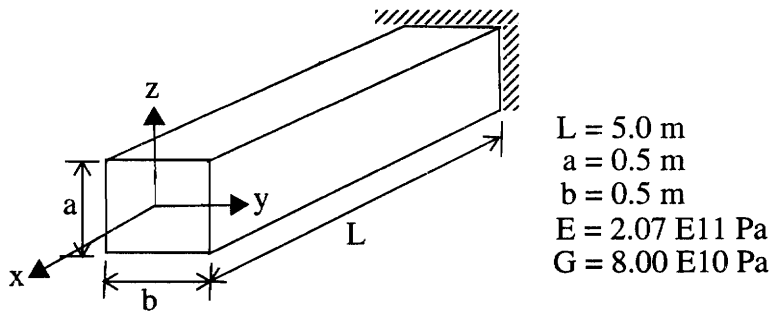

Fig. 5.1 The dimension and material properties of an isotropic cantilever beam.

beam shown in Fig. 5.1 was chosen as a test case. The dimensions and material properties of the beam are also shown in Fig. 5.1.

5.1.1.1 Axial displacement

An axial force of P = 1000 N was applied to the end of the beam and the axial displacement at the point of application of the load was calculated. The exact solution is a basic equation of the mechanics of materials, which is Eq. (5.1).

$$\bar{u}_0(L) = \frac{PL}{AE} \tag{5.1}$$

Excellent correlation between this exact solution and the results from SANDB are shown in Table 5.1.

Table 5.1 Axial displacement verification.

Exact solution	SANDB
9.6618 E-7 (m)	9.6618 E-7 (m)

5.1.1.2 Transverse deflection

An end load of P = 1000 N was applied in negative z-direction to the beam and the transverse deflection was computed. The exact solution, neglecting transverse shear deformation, obtained from mechanics of materials is

$$w_0(L) = \frac{PL^3}{3EI} \tag{5.2}$$

where I is a moment of inertia with respect to y-axis shown in Fig. 5.1. Results are shown in Table 5.2 and the percentage discrepancy is only 0.68 %.

Table 5.2 Transverse deflection verification.

Exact Solution	SANDB
1.9324 E-5 (m)	1.9457 E-5 (m)

5.1.1.3 Angle of twist due to a torque

The cross-sectional dimensions *a* and *b* of the beam shown in Fig. 5.1 were varied to show the effect of the thin wall beam assumption, which was assumed in the development of the model. A torque of T = 1000 N-m was applied at the end of the beam and the angle of twist was calculated. The exact solution obtained from elasticity for the case of free warping (St. Venant Torsion) is

$$\phi(L) = \frac{TL}{cab^3G} \tag{5.3}$$

The exact result is in which parameter *c* depends on the ratio of *b/a*. In the thin wall beam theory the ratio of *b/a* is assumed to be large and the asymptotic value of parameter c is used; i.e. $c \cong 1/3$ for $b/a \Rightarrow$infinity. So the angle of twist calculated by SANDB will not be close to the exact solution unless the ration of *b/a* is large. This trend of convergence to the exact solution as the ratio of *b/a* increases is shown in Table 5.3.

Table 5.3 Angle of twist comparison.

b/a	Exact solution	SANDB	b(m)	a (m)	c	% error
1.00	7.1124E-6	3.0000E-6	0.5	0.50	0.1406	57.82
2.00	2.1834E-6	1.5000E-6	1.0	0.50	0.2290	31.30
4.00	8.8968E-7	7.5000E-7	2.0	0.50	0.2810	15.70
10.0	2.0032E-4	1.8750E-4	1.0	0.10	0.3120	6.40
20.0	1.5015E-3	1.5000E-3	1.0	0.05	0.3333	0.10

5.1.2 *Angle of twist by bending & torsional coupling configuration*

Symmetric laminates with off-axis lamina exhibit coupling between shear, extension, bending, and twisting as reflected in

$$\overline{Q}_{16} = \overline{Q}_{26} \neq 0 \tag{5.4}$$

Thus, classical lamination theory stiffness A_{16}, A_{26}, D_{16}, and D_{26} are nonzero for the laminate. Utilizing this characteristic, the angle of twist of a symmetrically laminated beam was calculated by SANDB and I-DEAS. The beam consists of 24 layers of Graphite/ Epoxy unidirectional tape with fibers oriented 45° off the beam axis. The beam is clamped at the one end and a transverse load of 5 N is applied at the tip. The material properties and the dimensions of the beam are shown in Table 5.4.

Table 5.4 The material properties and the dimensions of the beam.

E_1 (Pa)	141.9E9	Length (m)	0.762
E_2 (Pa)	9.79E9	Width (m)	0.0254
G_{12} (Pa)	6.0E9	Thickness (m)	0.0027912
G_{23} (Pa)	4.8E9	Ply Thickness (mm)	0.01163
ν_{12}	0.42	Fiber Angle (°)	45

5.1.2.1 *I-DEAS*

The finite element modeling used for I-DEAS is shown in Fig. 5.2. The beam was divided into 15 thin shell elements. All the shell elements were treated under the "Laminate Modeling" task in I-DEAS. Node 1 and 2 are restrained for all the displacements and rotations. A nodal force of 0.5 P, where P is 5 N, is applied at the node 31 and 32.

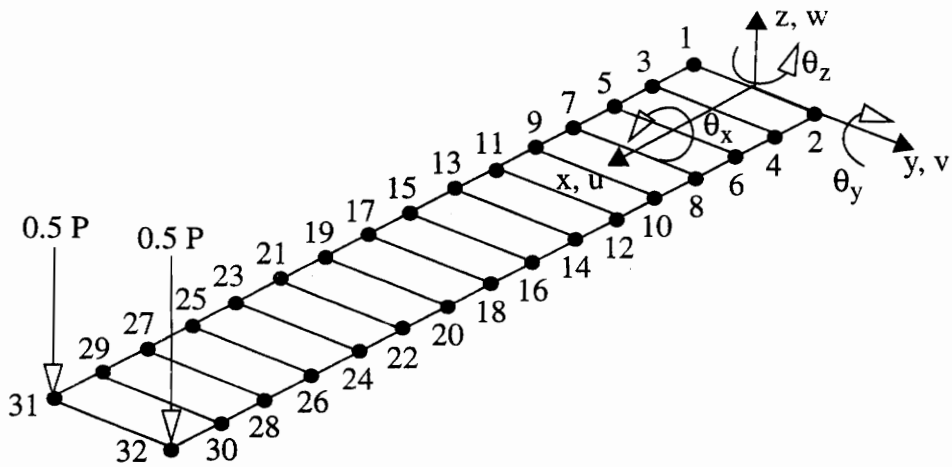

Fig. 5.2 I-DEAS model of the beam.

5.1.2.2 Comparison

The comparison of transverse deflection and the angle of twist between the two methods, SANDB and I-DEAS, is shown in Table 5.5. Similar to the I-DEAS model the beam was divided into 15 elements, but these are one-dimensional beam elements for SANDB solution. The I-DEAS shell model has 12 degrees of freedom and the SANDB beam model has 18 degrees of freedom. The agreement of SANDB to I-DEAS is very good for both transverse deflection and the twist

Table 5.5 Comparison of transverse deflection and the angle of twist.

	SANDB	I-DEAS
w (m)	1.07051	1.03245
θx (rad)	0.73286	0.73622

angle. The percentage errors are 3.69 % and 0.456 % for the transverse deflection and the angle of twist respectively. The one-dimensional beam model(SANDB) is much simpler than the two-dimensional shell model(I-DEAS) but this comparison shows the prediction of the response by the beam model to be nearly the same as the shell model.

5.2 Static analysis of a sandwich beam

5.2.1 Simply supported beam

The deflection of a simply supported sandwich beam was calculated by SANDB and it was compared to three other solutions, *NASTRAN* finite element code, Sharma and Rao[9], and Holt and Webber[10]. The coordinate system and geometry of the beam are shown in Fig. 5.3. The width of the beam (along y-axis) is denoted by b.

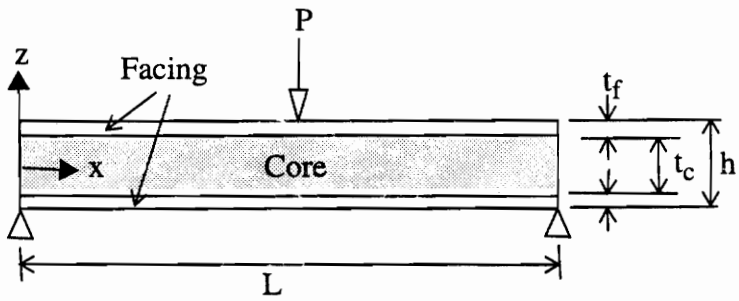

Fig. 5.3 The coordinate system and geometry of a simply supported sandwich beam.

The material properties and dimension of the beam are shown in Table 5.6. The thickness of the facings, t_f, and of the core, t_c, were varied to study the effects of the thickness ratio. Also, two different stiffness were used

Table 5.6 The material properties and dimension of the beam.

	Facing	Core	Beam dimension	
E (Pa)	2.07 E11	Varied	L (m)	3.05
G (pa)	8.0 E10	2.26 E10	h (m)	0.3556
ν_{12}	0.29375	0.31489	b (m)	1.0

for the core to demonstrate the difference between the weak core and the stiff core. The stiffness of the weak core is 2.07 E 09 (Pa) which is equal to 0.01 of the facing stiffness in case 1. The value of 6.89 E10 (Pa) is used for E in the stiff core case (case 2) and it is about 0.33 of the facing stiffness.

5.2.1.1 NASTRAN Model

Half of the beam shown in Fig. 5.3 is modeled due to symmetry. The *NASTRAN* discretization is shown in Fig. 5.4. The coordinate system, corresponding deflections, and the nodes are also shown in Fig. 5.4. The plate consists of three layers, which represent two face sheets and a core. It is assumed that the plate is perfectly bonded with infinitesimally thin bonding layers and there is no shear deformation across these layers. Thus, the continuity of displacements across the laminae is satisfied. The transverse shear deformation is assumed to occur only to the core layer, and shear correction factor k=5/6 is assumed.

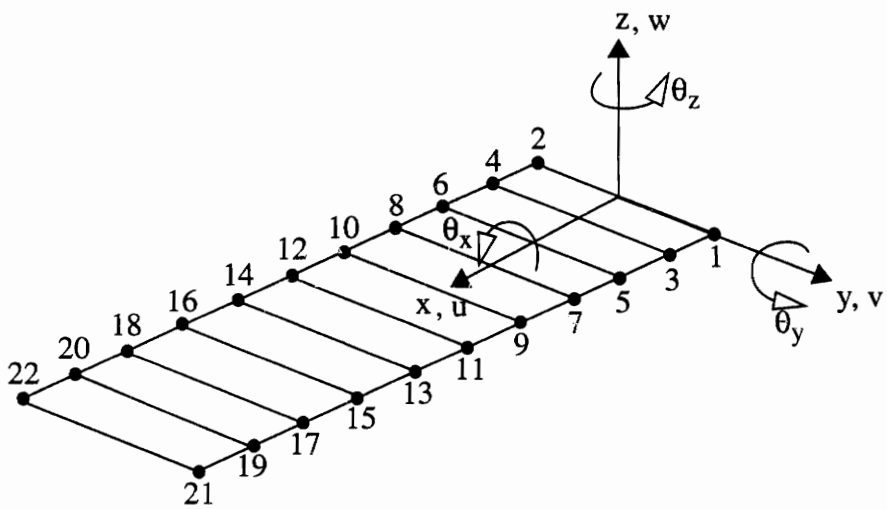

Fig. 5.4 The NASTRAN model of the beam.

The beam is divided into ten shell elements, which are identified as Quad4. The *NASTRAN* Manual[43] defines the Quad4 elements as "isoparametric quadrilateral elements with optional coupling of bending and membrane stiffness."

Each node has 6 degrees of freedom, and the boundary conditions are followings:

$u = 0$ at node 1 & 2	$\theta_x = 0$ at node 21 & 22
$v = 0$ at node 21 & 22	$\theta_y = 0$ at node 1 & 2
$w = 0$ at node 21 & 22	$\theta_z = 0$ at all the nodes

Since only one half of the beam is modeled, equal loads of P/4 were applied at nodes 1 and 2, giving a total load of P/2.

5.2.1.2 Sharma and Rao solution

Sharma and Rao[9] derived equations for static deflections of sandwich beams for various boundary conditions. The weak core assumption was taken in their model so the effects of the extensional and bending stiffness of the core is neglected. Facings were treated using the Euler hypothesis.

5.2.1.3 Holt and Webber solution

Holt and Webber[10] derived analytical solutions that can be used to verify finite element models. In their analysis, the facings were treated as membranes and the core was considered to be thick. The extensional and bending stiffnesses of the core were neglected, but not its transverse shear flexibility.

5.2.1.4 Comparison between the solutions

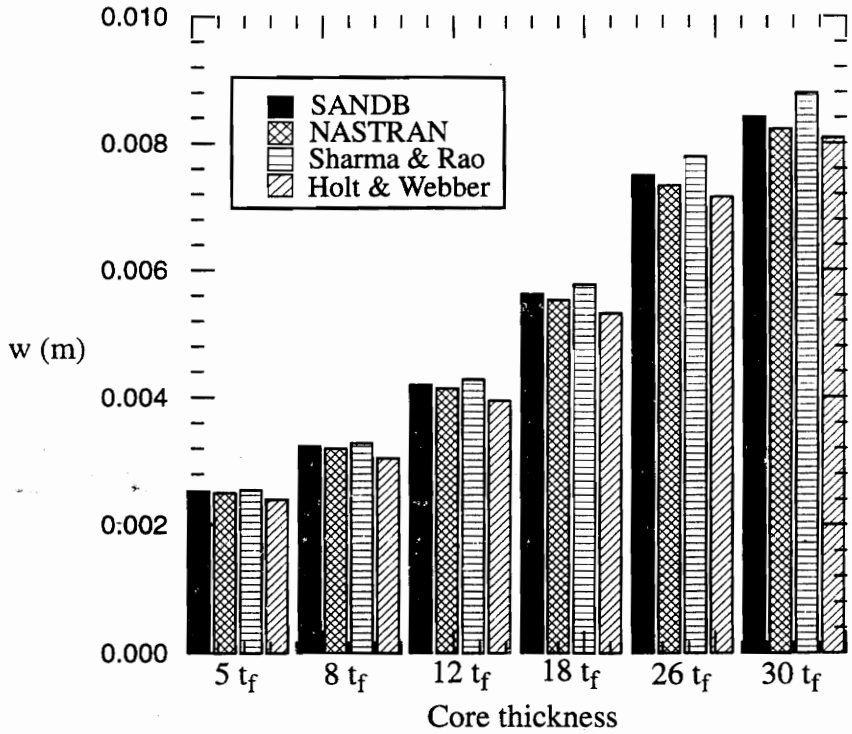

Fig. 5.5 Comparison of the transverse deflection of the beam for case 1: soft core.

The comparison of the transverse deflection from the soft core case, E_c=0.01E_f, calculated by three different methods, previously mentioned, and the new model, SANDB, is shown in Fig. 5.5. The good agreement exhibited by SANDB with other solutions can be seen for a range of core thickness.

The comparison for the stiff core case, E_c=0.33E_f, is shown in Fig. 5.6. The values of SANDB are in good agreement with the results of NASTRAN while two other solutions substantially over predicts the deflection, especially for the thick core sandwich beams. Since this is a stiff core case, the effects of bending stiffness of the core can not be ignored and this fact is obvious in the comparison of the results obtained by different methods.

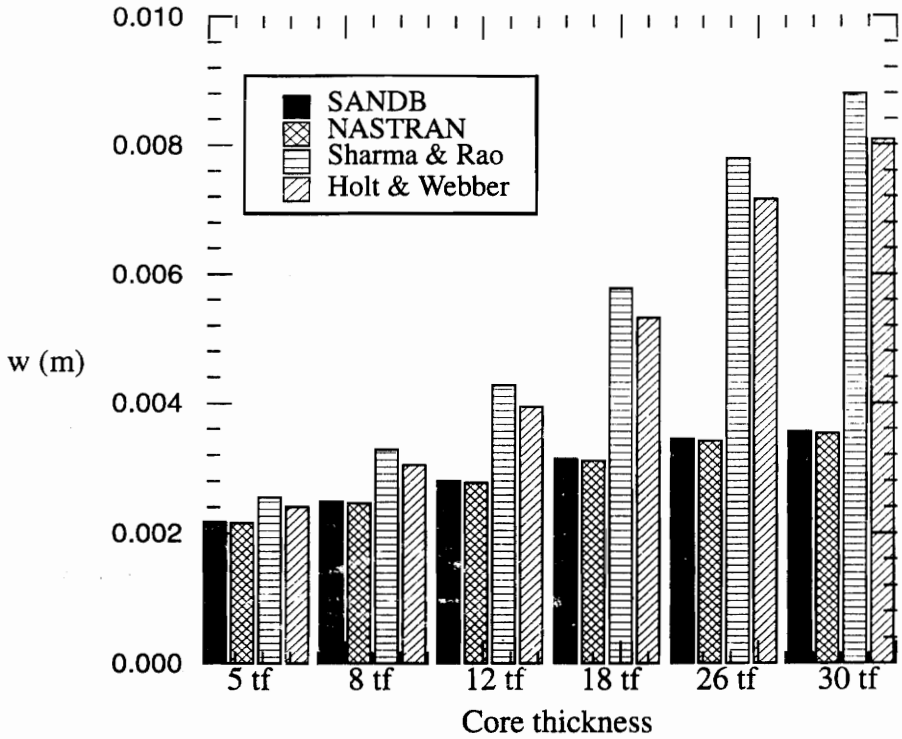

Fig. 5.6 Comparison of the transverse deflectin of the beam for case 2: stiff core.

From these comparisons, for the soft core and the stiff core cases, the predictions of SANDB are shown to be accurate in both cases, and thus can be confidently applied to analyze sandwich beams of varying core thickness and stiffness. Even though SANDB is simpler model, a one-dimensional beam model, agreement with the *NASTRAN* shell model is very good.

5.2.2 A cantilever sandwich beam

A cantilever beam shown in Fig. 5.7, which is suggested for robotics applications in Ko[20], was used as a test case. The y-axis is into the beam and subscript "f" and "c" denote facings and the core respectively. The dimensions are shown in Table 5.7. The material properties of the beam are identical to the previous case, the simply supported beam in Table 5.6, except the stiffness of the core was held fixed at Ec = 6.89 E10 (Pa). The dis-

tributed load, w, is the self weight of the beam calculated from the given densities and dimensions.

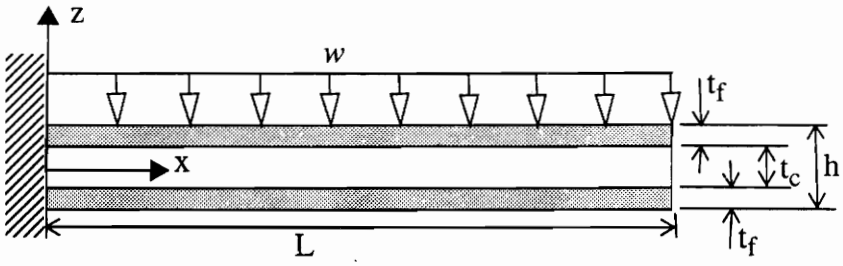

Fig. 5.7 The coordinate system of a cantilever beam.

Table 5.7 The dimension of the cantilever beam.

L (m)	h (m)	t_f (m)	t_c (m)	ρ_f (kg/m^3)	ρ_c (kg/m^3)
3.05	0.254	0.0508	0.1524	7850	2710

The comparison between the results from different solution methods is shown in Table 5.8. The value given by Ko[20] is an from an exact solution. The SANDB result is within 2.02 % of Ko's result. The other two methods over-predict the deflection. This is expected since Holt & Webber and Sharma & Rao are assuming either soft core or thick

Table 5.8 The tip deflection of the cantilever beam(m) subjected to self weight.

SANDB	Ko	Holt & Webber	Sharma & Rao
0.0005413	0.0005304	0.0005505	0.0005791

core whereas the core of this beam is thin, it has a thickness that is only three times the thickness of the facing, and its core is rather strong. This example illustrates one advantage of SANDB; it calculates accurate displacements for any core stiffness and any thickness ratio of the core to the facing sheets.

5.2.3 *A sandwich beam with transversely flexible core*

Frostig and Baruch[14] investigated the bending behavior of sandwich beams with transversely flexible core. One of their examples was used to check the performance of SANDB. The coordinate system of the beam is shown in Fig. 5.8 where the subscripts

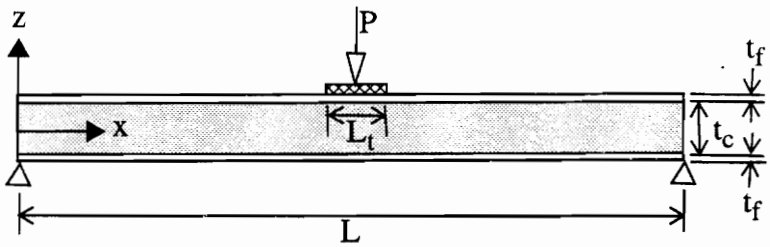

Fig. 5.8 The coordinate system of the beam with transversely flexible core.

"f", "c", and "t" denote facings, the core, and the tab respectively. The dimensions of this beam are shown in Table 5.9, and b denotes the width of the beam.

Table 5.9 Material properties and beam dimensions form Ref. 14.

	Facings	Core	Beam dimension	
E (kg/mm2)	2742	5.25	L (mm)	300
G (kg/mm2)	160	2.10	b (mm)	60
t (mm)	0.5	19.09	P (kg)	50

Frostig and Baruch[14] focused on the localized effects and their model was based on the superposition of two beam substructures, one with a core which resists shear and transverse normal stresses and the other with vertically flexible core. Thickness stretching of the core was allowed to be changed and the plane section did not remain plane. Thus the higher order deformation effects in the core were considered.

Table 5.10 Comparison of mid-span beam displacement from SANDB and Ref. 14.

SANDB	Frostig & Baruch
3.02 (mm)	3.16~3.36 (mm)

The comparison of the displacement at the middle of the beam, x = L/2, is shown in Table 5.10. SANDB predicts a displacement 4.43 % smaller than the lower value given by Frostig and Baruch. This is in a reasonable range since SANDB does not take account of the transverse normal extension of the core.

5.3 Verifications of theory with PZT

5.3.1 Transverse Deflection

To verify the results from SANDB program for beams actuated in bending by PZT actuators, two simple models were used as test cases. One beam model has PZT actuators on the top and bottom of the whole beam, case 1, and the other has PZT patches partially bonded on the top and the bottom of the beam case 2 as shown in Fig. 5.9. The material

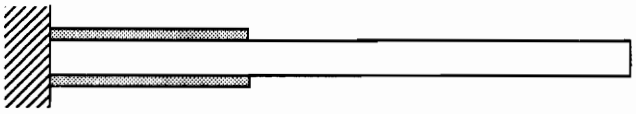

Fig. 5.9 The beam with PZT actuators.

properties and the dimensions of the beam are shown in Table 5.11. Results computed from DAISA(Dynamic Analysis of Induced Strain Actuators)[44] software were used to compare to SANDB predictions.

Table 5.11 Material properties and dimensions of PZT beam examples.

	Beam	PZT	PZT electrical properties	
$E_1=E_2$ (Pa)	6.89E10	6.30E10	d31 (m/V)	254E-12
$G_{12}=G_{13}=G_{23}$ (Pa)	2.62E10	2.42E10	$E3^{top}$ (Volt)	100
ν_{12}	0.3139	0.3	$E3^{bottom}$ (Volt)	-100
Thickness (m)	0.3556	0.03		
Length (m)	3.05	$3.05^1/1.22^2$		
Width (m)	1.0	1.0		

5.3.1.1 DAISA

DAISA is a software program developed at the Center of Intelligent Material Systems and Structures.[44] The program implements the models of Crawley and De Luis[24], Liang, Sun, and Rogers[45,46], and was the dynamic finite element approach. It can only model isotropic beams with perfectly bonded actuators on the top and bottom, which induce the bending by out of phase voltage of the same magnitude. The thermal expansion model in DAISA was used in this study as the comparison. Details of this model can be found in the user manual[44] and its references.

5.3.1.2 Comparison

The comparison between SANDB and DAISA for the case 1, an aluminum beam with PZT bonded on the top and bottom over the whole surface, is shown in Table 5.12. The agreement of the tip deflection is very good with a percentage difference of only 0.472 %.

Table 5.12 Tip deflection comparison for case 1.

Program	Tip deflection (cm)
DAISA	7.193E-4
SANDB	7.159E-4

The results for the case 2, an aluminum beam with PZT patches partially bonded on the top and bottom surface along a limited length, is shown in Table 5.13.

Table 5.13 Tip deflection comparison for case 2.

Program	Tip deflection (cm)
DAISA	4.604E-4
SANDB	4.585E-4

The results are in good agreement for this case, too. The difference between results from DAISA and SANDB is only 0.4048 %.

5.3.2 Axial displacement

The example problem in Robbin and Reddy[28] was chosen for the verification of the axial displacements calculated by SANDB for beams with PZT actuators acting in extensions. The induced strain is prescribe as 100 $\mu\varepsilon$. The configuration, dimension, and the

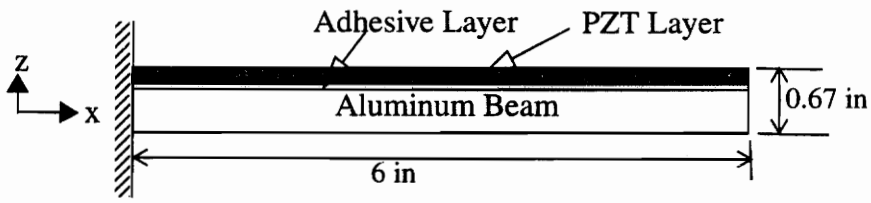

Fig. 5.10 The dimensions & the coordinate system of the beam from Robbin and Reddy.[28]

coordinate of the beam are shown in Fig. 5.10. As can be seen in the figure, there is an actuator layer only on the top of the beam. Because of this antisymmetry with respect to the x axis, the beam also bends while the PZT is in the extensional mode. The material properties of this beam is shown in Table 5.14.

Table 5.14 Material properties and dimensions for the beam from Ref. 28.

	Aluminum	Adhesive	PZT
E_1 (lb/in^2)	1.0E7	1.0E6	1.0E7
E_3 (lb/in^2)	1.0E7	1.0E6	7.0E6
ν_{13}	0.25	0.4	0.25
ν_{31}	0.25	0.4	0.175
G_{13} (lb/in^2)	4.0E6	0.357E6	3.0E6
Thickness (in)	0.60	0.01	0.06
Length (in)	6.0	6.0	6.0

5.3.2.1 Robbin and Reddy's model

Robbin and Reddy[28] developed and compared four different finite element models of actuated beams shown in Fig. 5.10. All the models were 2-dimesional in the x-z plane. Four models are CBT, "The first equivalent single-layer theory", SDBT, "The second equivalent single-layer theory", MLBT1, "The first multi-layer beam theory", and MLBT2, "The second multi-layer beam theory." The detail description of each model can be found in Robbin and Reddy.[28] In their study, MLBT2 was found to satisfy all the traction boundary conditions of the problems. The importance of including transverse shear deformation to the analysis was emphasized in their work.

5.3.2.2 Comparison

The comparison of the axial and the transverse displacements calculated by Robbin and Reddy's models and SANDB are shown in Table 5.15. The axial displacement of SANDB is in good comparison with other models. The percentage difference in the axial displacements of MLBT2, the best model of Robbin and Reddy, and SANDB is 2.57 %.

Table 5.15 Comparison of nondimensionalized displacements from Ref. 28 and SANDB.

Model	u(10000)/h	w(100)/h
Robbin&Reddy-CBT	8.3787	-2.0393
Robbin&Reddy-SDBT	8.3787	-2.0393
Robbin&Reddy-MLBT1	8.0239	-2.0393
Robbin&Reddy-MLBT2	7.8699	-2.0358
SANDB	8.0723	-2.1707

The transverse deflection calculated by SANDB is slightly larger than other models. The percentage difference of SANDB with MLBT2 is 6.63 % and it is 6.44 % for other three models. This is still a good comparison considering that the SANDB is a one-dimensional model and the others are all two-dimensional.

5.3.3 Angle of twist induced by bimoment

An aluminum beam with four PZT actuators bonded on as shown in Fig. 5.11 was used to verify the angle of twist induced by bimoment actuation. The angle of twist was calculated by the SANDB and NASTRAN and they were compared to verify the SANDB.

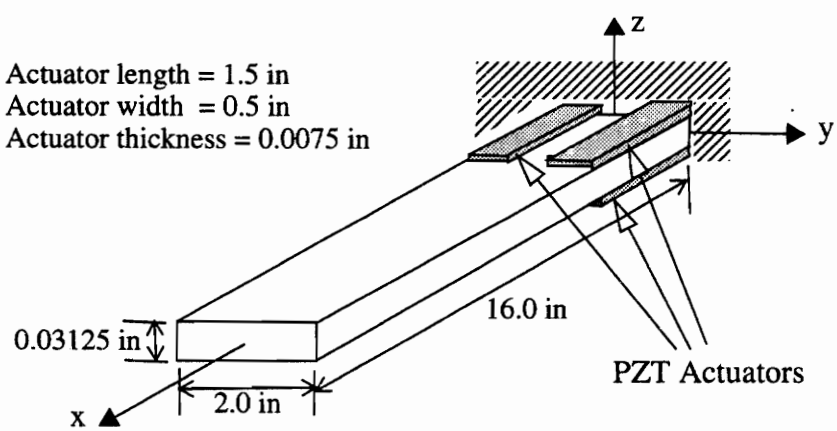

Fig. 5.11 An aluminum beam with four PZT actuators.

5.3.3.1 NASTRAN model

A solid model (three-dimensional) of the beam shown in Fig. 5.11 was created for *NASTRAN* analysis. Hexagonal elements were used for the entire model. 512 elements were used for the beam and 12 elements were used for the PZT actuators with three elements for each actuator, were used. Induced forces for each actuator were calculated analytically and applied as nodal forces at the end of actuators to simulate the bimoment activated by PZT. The twist of angle was derived from the displacements calculated by *NASTRAN*.

5.3.3.2 Comparison

The comparison of the twist of angle calculated by SANB and NASTRAN is shown in Table 5.16. The difference between the two methods is 5.92 %. This is in a reasonable range considering that the NASTRAN model is three-dimensional and the SANDB model is one-dimensional.

Table 5.16 Angle of twist from SANDB and *NASTRAN* for bimoment actuation.

SANDB	*NASTRAN*
0.20159 °	0.21427°

5.4 Convergence study

An isotropic beam with a simple configuration of PZT patches, as shown in Fig. 5.12, was used to study for convergence of the finite element solution. There are two PZT

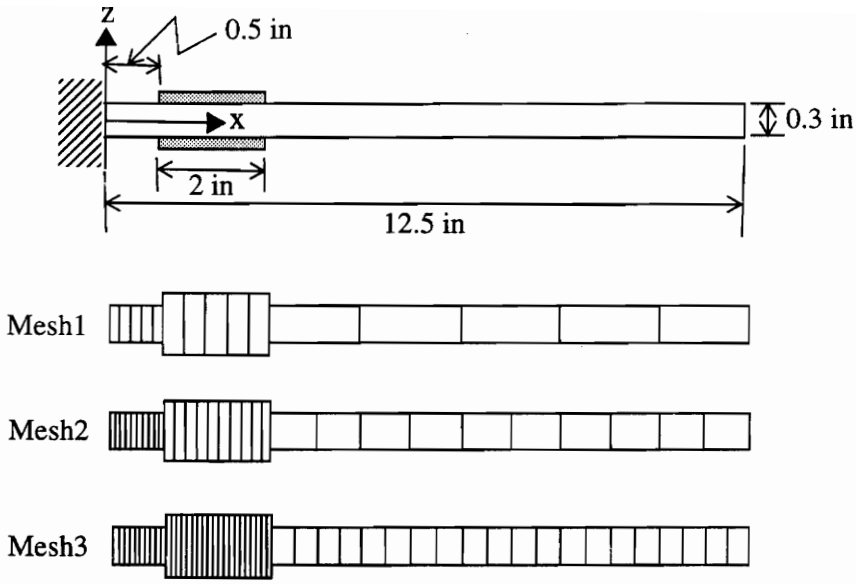

Fig. 5.12 The beam dimensions and different meshing.

patches of the same width as the beam, one bonded on the top and the other on the bottom of the beam. The width of the beam and the PZT patches is 3.0 inches and the thickness of the each patches is 0.03 inches. The material properties are the same as whose used the previous section, Robbin and Reddy (Table 5.14) but the adhesive layer was not included.

There are three different meshes used for comparison, and these meshes are also shown in Fig. 5.12. In each mesh, the beam is divided into three sections. The range in x for section one is $0 \leq x \leq 0.5$ inches, section s is $0.5 \leq x \leq 2.5$ inches, and the rage for section three is $2.5 \leq x \leq 12.5$ inches. In Mesh 1 each section was divided into five equal length elements, for a total of fifteen elements. In Mesh 2 each section is divided into ten equal length elements, for a total of thirty elements. In Mesh 3 sections one and three were divided into ten equally spaced element, while section two was divided into twenty equal length elements. Mesh 3 has forty elements total. Also, a fourth mesh was considered in some cases. Mesh 4 has forty total elements, ten in section one, twenty in section

two, and ten in section three. However, the elements in Mesh 4 are not the same length. Shorter elements were used in the region around the edge of actuators and longer elements were used in the rest of the beam.

5.4.1 Induced bending deformation

A bending moment was induced in the beam shown in Fig. 5.12 by applying induced strain of 200 $\mu\varepsilon$ to the top PZT actuator and -200 $\mu\varepsilon$ to the bottom actuator. The transverse deflections over the length of beam calculated by 3 different meshes, are shown in Fig. 5.13. As it can be noticed from the figure, good convergence was achieved for each mesh. The element size does not have significant effect on the value of the transverse displacements for induced bending of the isotropic.

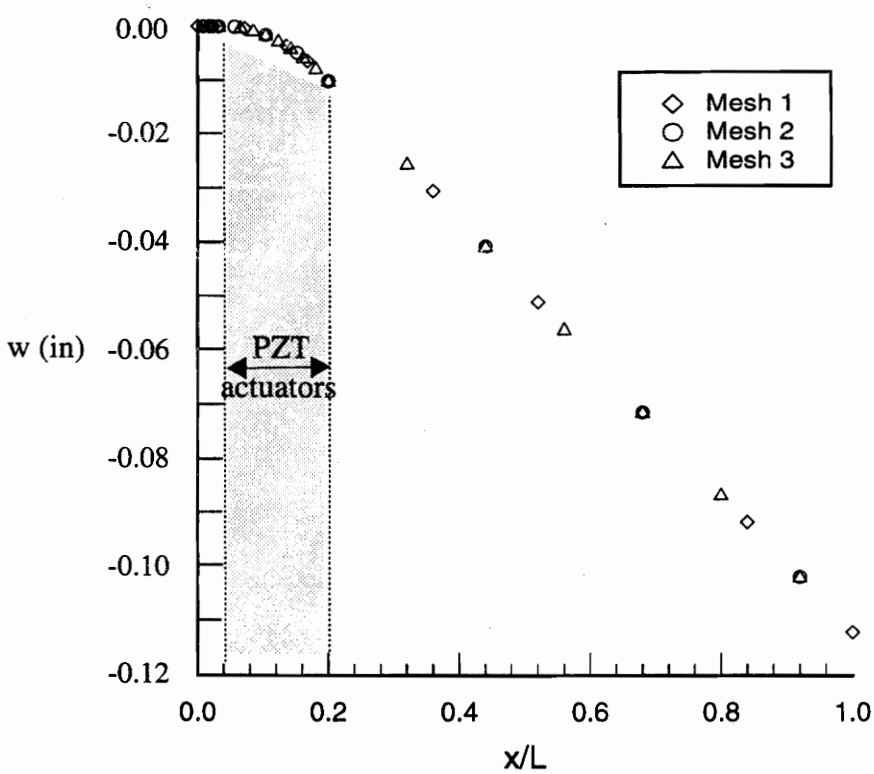

Fig. 5.13 Distribution of the transverse deflection of the beam subject to induced bending.

5.4.2 *Induced bimoment deformation*

The top and the bottom patches of the beam shown in Fig. 5.12 were divided into two patches along y-axis, resulting in a total of four patches on the beam. Strains with opposite signs and a magnitude of 200 $\mu\varepsilon$ were applied to the PZT actuators to induce a bimoment. (The actuator configurations for inducing a bimoment are explained in Section 3.4.) The comparison between the three meshes for the angle of twist are shown in Fig. 5.14. It can be observed from the figure that the length of the element is critical for these elements near the edges of PZT actuators. Differences in the twist angle on the right side of the actuator between Mesh 1 and Mesh 3 are significant.

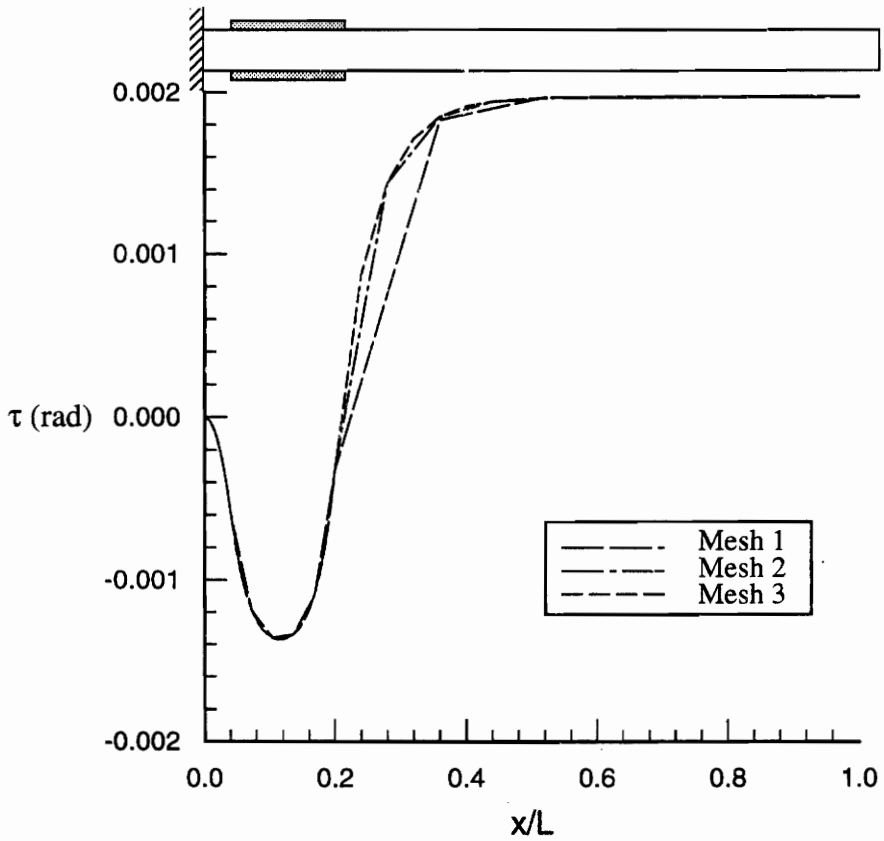

Fig. 5.14 Distribution of the angle of twist for the beam subject to induced bimoment.

The comparison for the first derivative of the angle of twist is shown in Fig. 5.15. Like the case for the angle of twist, the need for mesh refinement around the edges of actuators can be observed from this figure also.

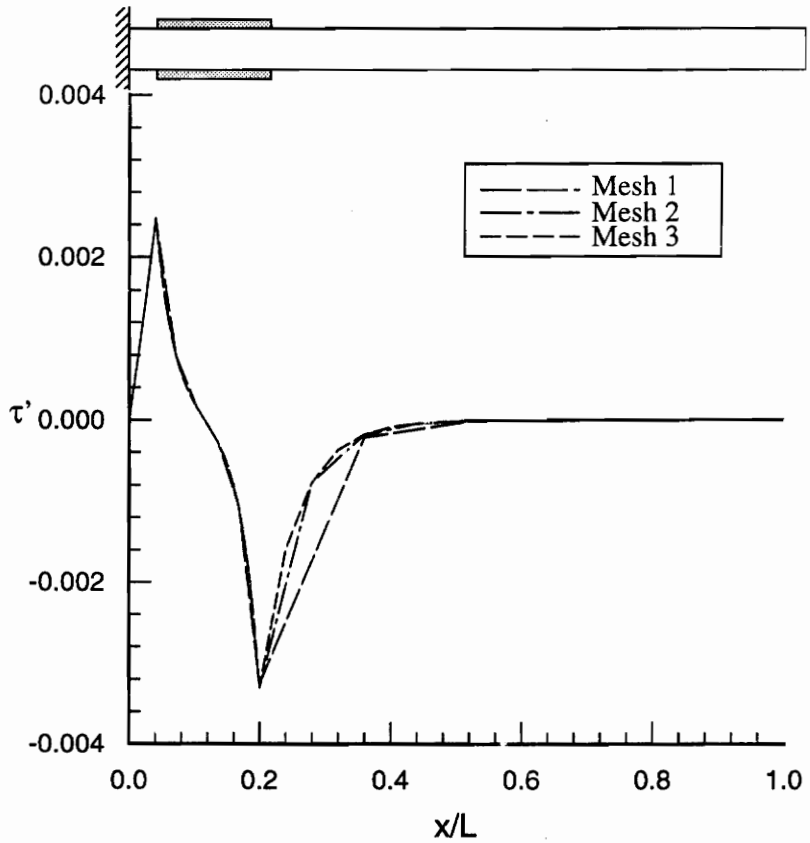

Fig. 5.15 Distribution of the derivative of the twist angle for the beam subject to induced bimoment.

The comparison of the predicted twist of angle between Mesh 3 and 4 is shown in Fig. 5.16. These two cases converged almost identically. There are slight differences in the prediction of the angle of twist in the region of the right hand edge of the PZT actuator.

For Mesh 4, the element lengths in the region near the edges of actuator were highly refined and this resulted in a smoother curve. Since the elements with longer lengths are used in the right side section of the actuator in Mesh 3, the difference with Mesh 4 is more obvious for this region.

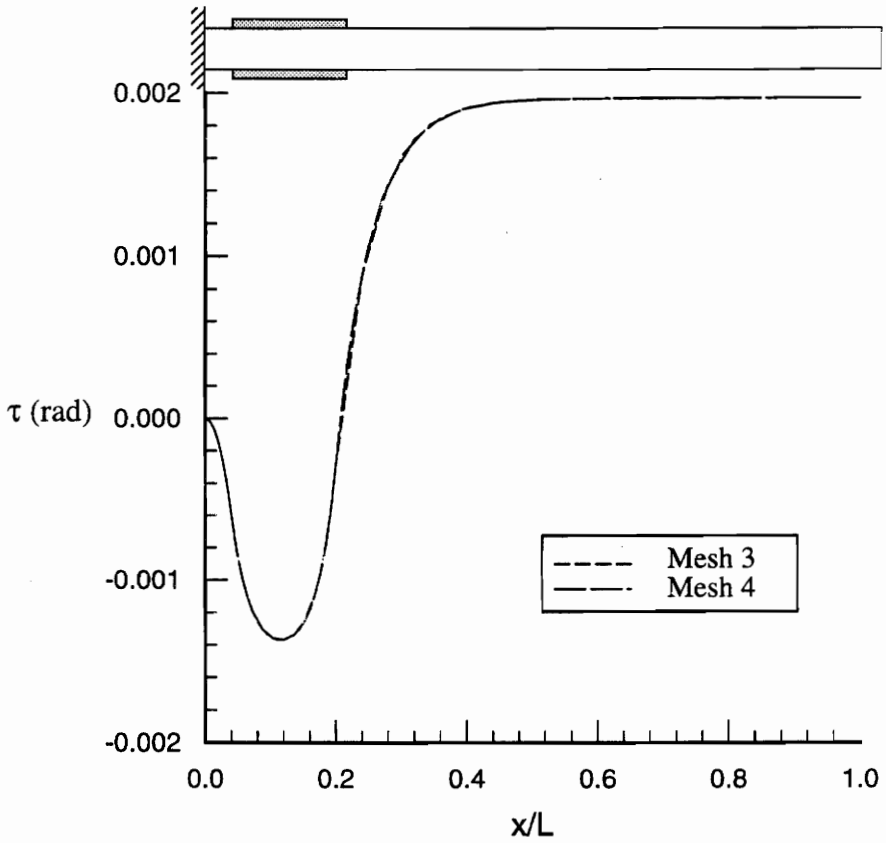

Fig. 5.16 Distribution of the angle of twist for the beam subject to induced bimoment.

The distributions of the first derivative of the angle of twist for Mesh 3 and 4 is shown in Fig. 5.17, and a similar behavior as Fig. 5.16 is observed.

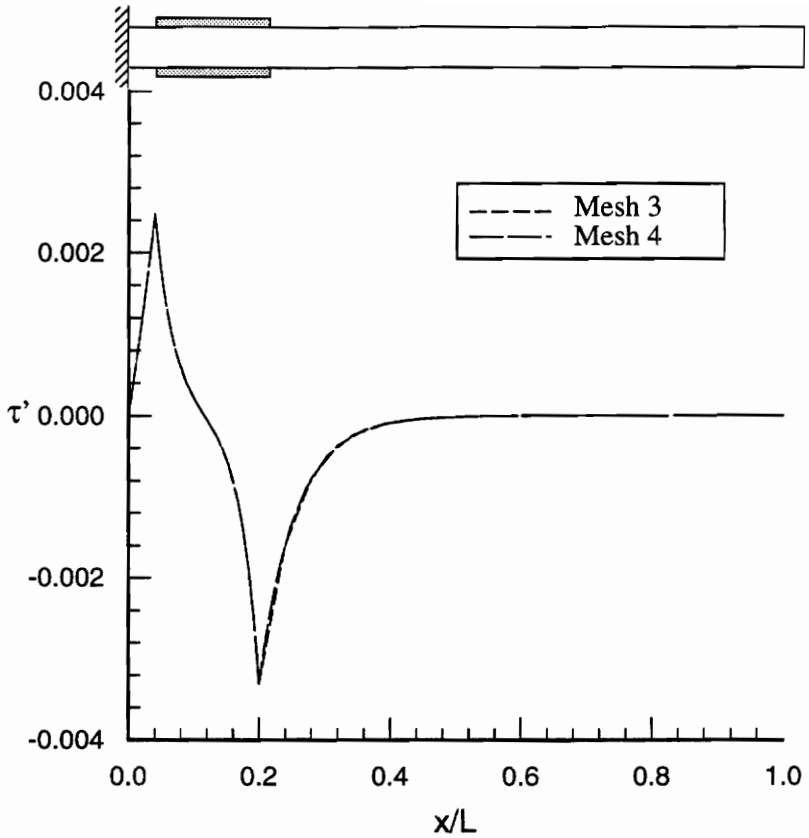

Fig. 5.17 Distribution of the derivative of the twist angle for the beam subject to induced bimoment.

From this study of mesh refinement, it was found that a refined mesh near the edges of actuator results in a better prediction of the angle of twist and its derivative.

5.4.3 Distance between distributed PZT Patches

Induced forces from PZT patches are transferred to substrates at the edges of patches. When the PZT actuators are activated for a bimoment, there are counter bimoments induced at the two edges of the patch. This can be observed in Fig. 5.14 in the previous

section by the drop and rise of angle of twist near the edges of actuators. If an edge of the PZT actuator is restrained, the counter effects will be suppressed. If actuators are spatially distributed on a beam, counter bimoments could result in either a drop and rise in the angle of twists between actuator or the drop and rise could be suppressed. To study the effect of the separation distance between distributed patches, a cantilever beam with distributed PZT actuators was analyzed. The dimension and the material properties of the beam are the same as the beam used for study of mesh refinement in Sections 5.4.1 and 5.4.2.

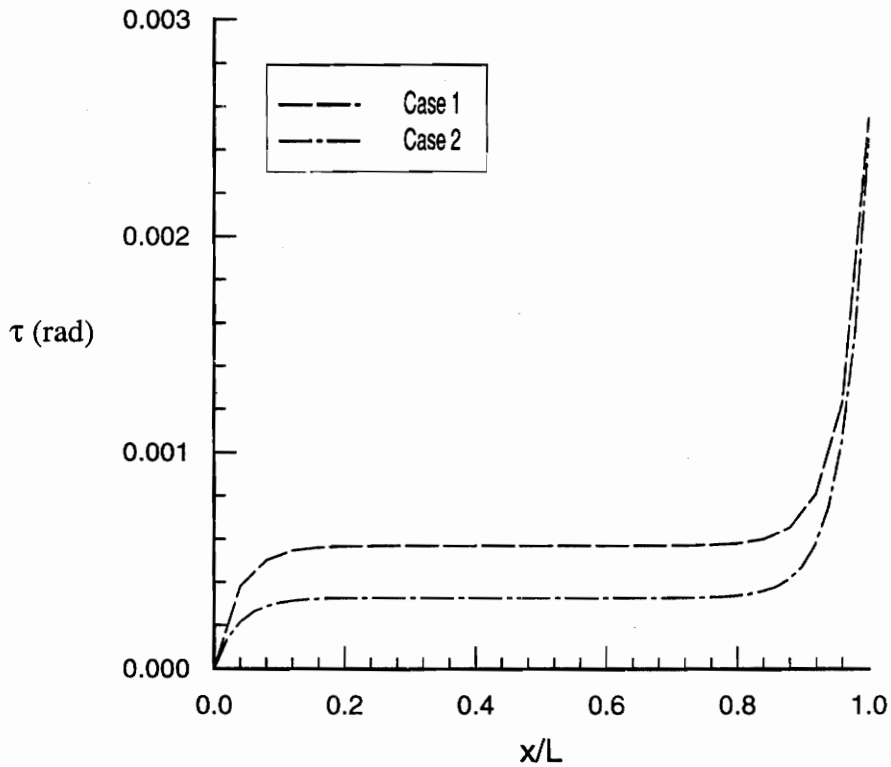

Fig. 5.18 Comparison of the angle of twist for a beam with distributed actuators.

The angle of twist over the beam length for a cantilever beam with distributively bonded PZT actuators is shown in Fig. 5.18. The beam was divided into 49 equal length elements for Case 1 and PZT patches were bonded onto every other element starting from

the wall, resulting a total of 25 PZT actuators distributed over the whole beam. In Case 2, the beam was divided into 25 equal length elements with PZT patches on every other elements, for a total of 13 PZT actuators distributed on the whole span of the beam. In both cases, the separation distance between actuators was the same as the element length which the same as the PZT patch length.It is observed from Fig. 5.18 that the influence of counter bimoments between adjacent actuators is suppressed in both cases. Only the first and the last PZT actuators have effected the angle of twist.

The first derivative of the twist angle over the span of the beam for Case 1 and 2 is shown in Fig. 5.19. The counter effects of bimoments from each actuators are shown as a drop and rise in the derivative of twist, and the locations of actuators are obvious from these curves. The actuators at the wall and at the tip have the most influence on the derivative of the twist as was the case for the angle of twist.

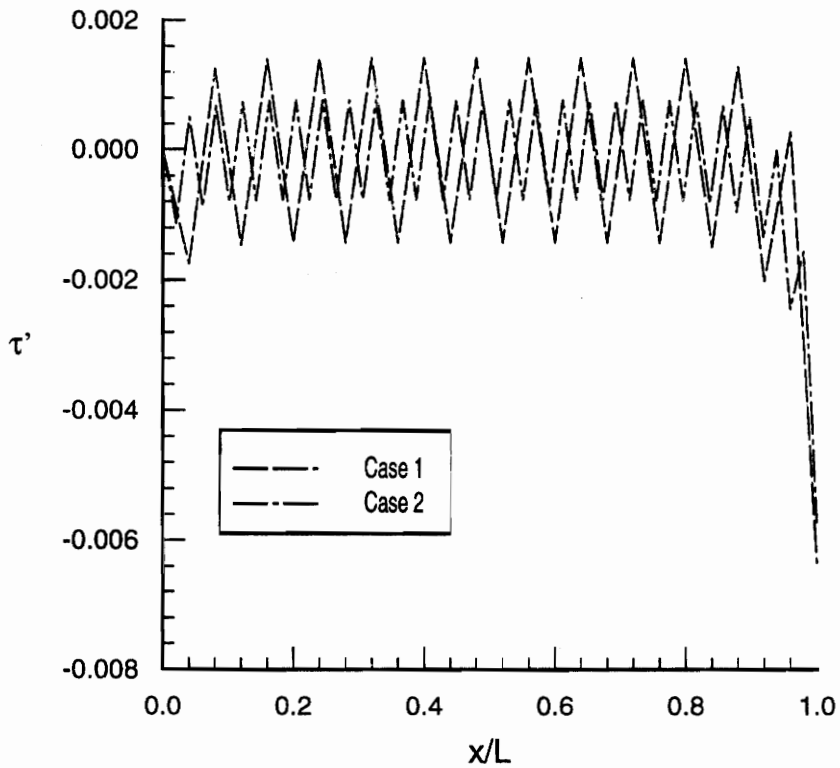

Fig. 5.19 Comparison of τ' for a beam with distributed actuators.

The distance between the distributed PZT actuators is the same as the actuator length for Case 1 and 2. For Case 3, this distance was doubled. Case 3 has distributed actuators which are the same size as in Case 2 but the total number of actuators on the beam is 7 since they are distributed over a wider range. The comparison of angle of twists for Case 2 and 3 is shown in Fig. 5.20. Case 3 shows a drop and rise in the angle of twist between actuators indicating

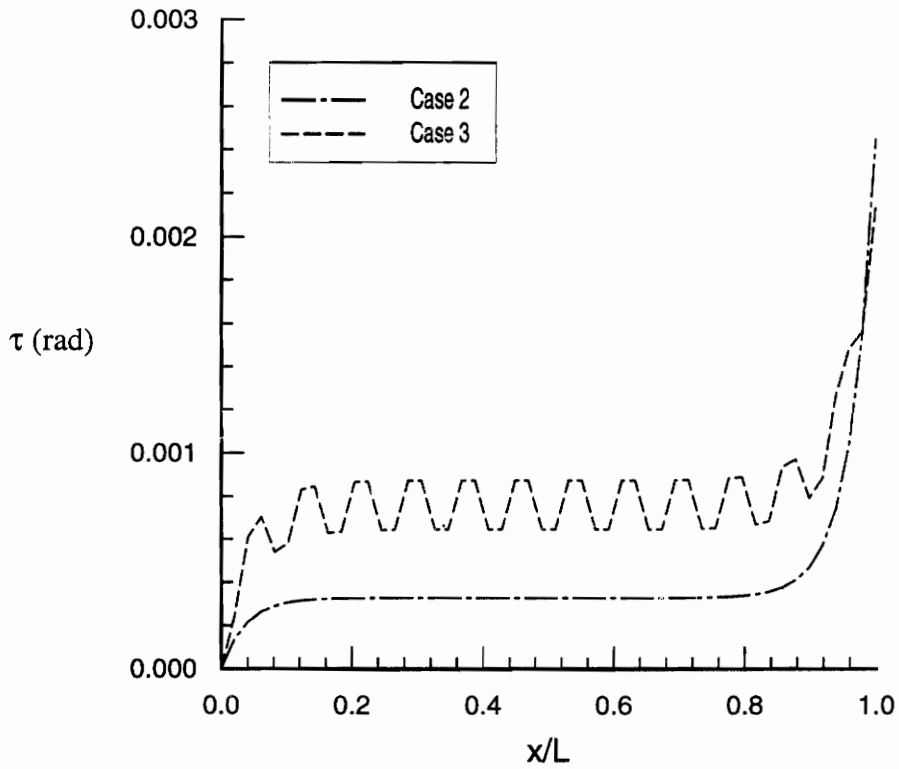

Fig. 5.20 Comparison of angle of twists for a beam with distributed actuators.

the effects of the distance between the distributed actuators. The first and last actuators play still the important role to the induced twists for Case 3 as in the other cases.

The comparison of the first derivative of angle of twist for Case 2 and 3 is shown in

Fig. 5.21. The trend in this curves are similar to the other cases; e.g., compare to Fig. 5.19. The location of PZT actuators can be observed as a drop and rise in the curve. The influence of the actuators at the wall and the tip are seen to have the largest effect on the derivative of the twist angle.

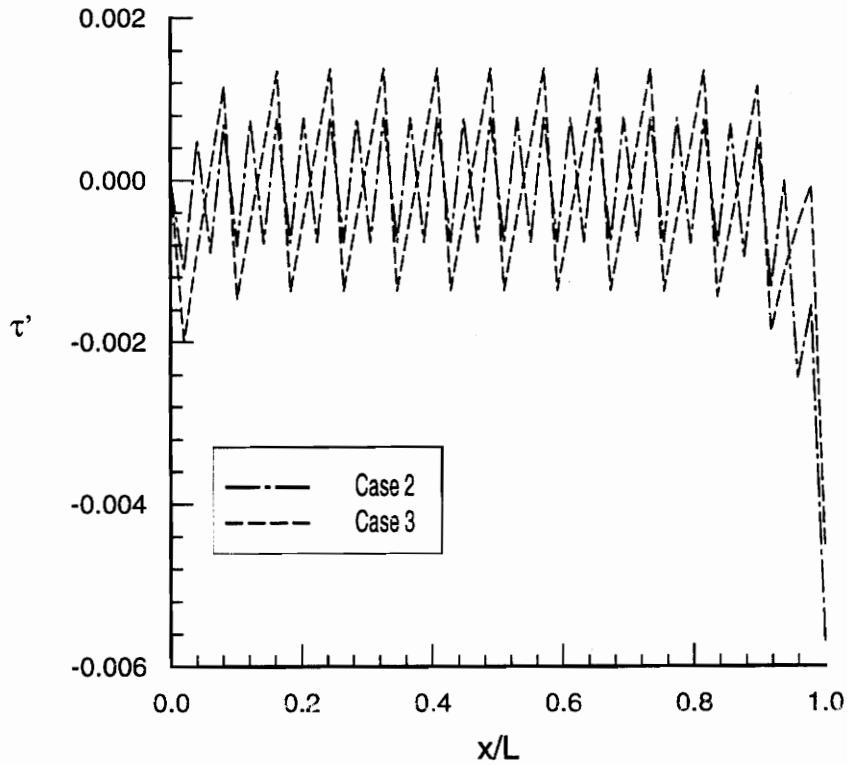

Fig. 5.21 Comparison of τ' a beam with distributed actuators.

5.5 Torsional problems

Torsion can be caused by either St. Venant torque, bimoment, or a combination of the two. According to Gjelsvik,[47] torsion can be expressed as;

$$EI_{\Omega\Omega}\phi'''' - GJ\phi'' = -(M_{\Omega}' - T) \tag{5.5}$$

where ϕ is angle of twist, $I_{\Omega\Omega}$ is warping constant, J is torsion constant, M_Ω is bimoment, and T is St. Venant torque. Depending on the magnitude of the resistance, bimoment resistance, $EI_{\Omega\Omega}$, and torsion resistance, GJ, the torsion problem can be approximated by one method, of bimoment or St. Venant torque. A detailed discussion about the torsional problem can be found in Gjelsvik.[47]

5.5.1 Bimoment resistance

In this study, control of a beam by bimoment is of major interest. To effectively control a beam, it is critical to reduce the bimoment resistance. In this section, configurations which will reduce the bimoment resistance are examined.

5.5.1.1 Different facing materials and thickness

The sandwich beam used for the study of bimoment resistance, $EI_{\Omega\Omega}$, is shown in Fig. 5.22. Rohacell foam was used for the core. The material and the thickness of the fac-

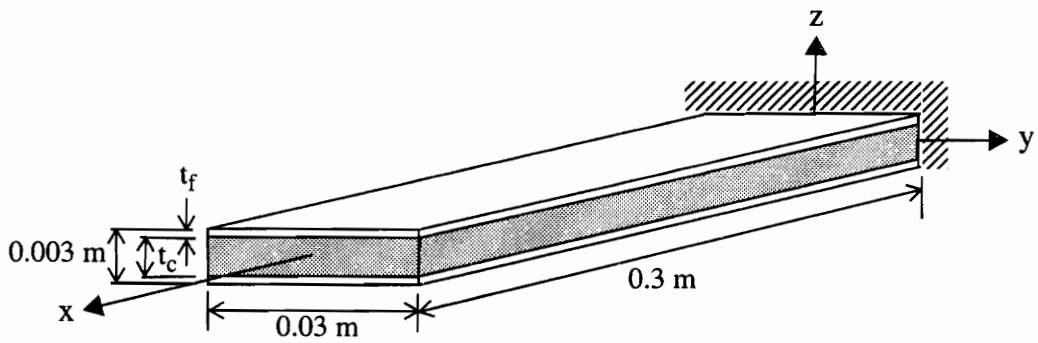

Fig. 5.22 The dimension of a sandwich beam.

ings were varied to study the effects. The material properties of the beam are shown in Table 5.17. For Graphite/Epoxy facings, fibers were orientated at the 0°, on the beam axis.

Table 5.17 The material properties of a sandwich beam.

	Rohacell Foam Core	Aluminum Facings	Graphite/Epoxy Facings
E1 (Pa)	128.41E6	68.9E9	138.0E9
E2 (pa)	128.41E6	68.9E9	10.0E9
G12 (Pa)	71.31E6	26.2E9	6.90E9
G31 (Pa)	71.31E6	26.2E9	3.86E9
n12	0.3	0.315	0.3

Bimoment resistance of sandwich beam with different facing materials and facing thickness, t_f, is shown in Table 5.18. From Table 5.18, it can be concluded that the thinner the facings, the smaller the bimoment resistance. The bimoment resistance for a solid aluminum beam of the same dimension is 0.34881E-03 (Pa in^6). Thus the sandwich configuration with thin facings has advantage over the solid beam in reducing the bimoment

Table 5.18 Bimoment resistance of sandwich composite beams with foam core.

t_f (m)	tc/tf	Aluminum Facings (Pa in^6)	Graphite/Epoxy Facings (Pa in^6)
0.001	1.0	0.33589E-03	0.67277E-03
0.0005	4.0	0.24565E-03	0.49182E-03
0.00015	18.0	0.94574E-04	0.18980E-03

resistance. Also, it was found that with the fiber orientation of 0°, the advanced fiber-reinforced composite facing is inferior to the traditional material facings in reducing the bimoment resistance.

5.5.1.2 Orientation of the fibers

In the previous subsection, it was found that the thin advanced-fiber reinforced facing composite sandwich beam with the 0° fiber orientation have the small bimoment resistance but not as small as the aluminum facings. Using the configuration, t_f=0.00015(m) of Graphite/Epoxy facings, further study of the bimoment resistance was done about fiber

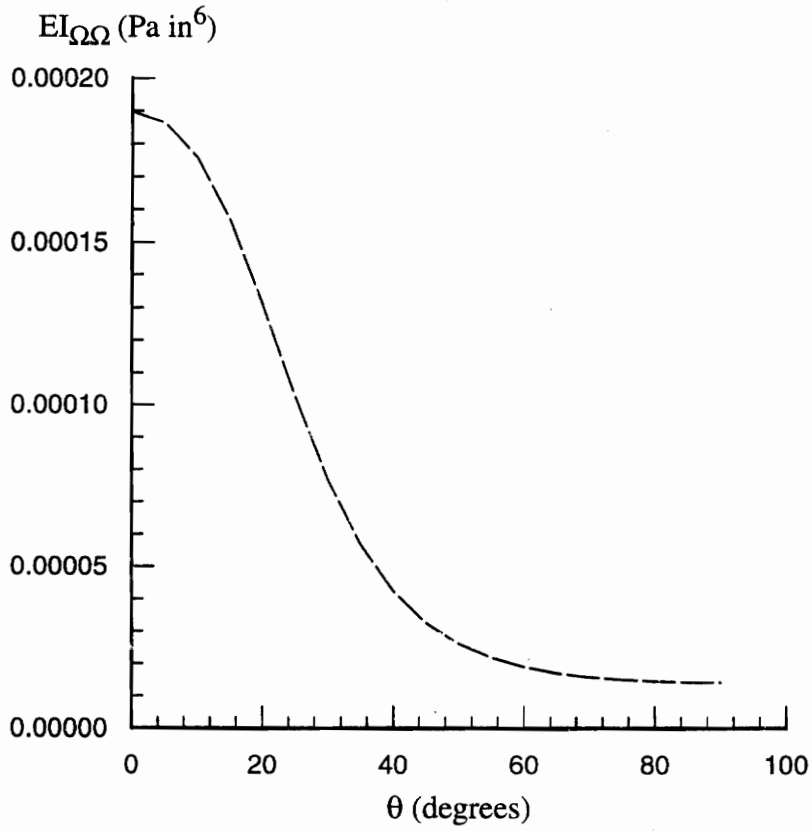

Fig. 5.23 Bimoment resistance vs. fiber orientation in facings.

orientations. Fig. 5.23 shows the bimoment resistance for various fiber orientations. The least bimoment resistance occur at the fiber orientated 90° off axis from the beam axis.

5.5.2 *Decay length*

A cantilever beam shown in Fig. 5.22 with Graphite/Epoxy facings was used to study the decay length of bimoment induced by PZT patches bonded on the beam. The cross-sectional property for this beam was chosen according to the results in Section 5.5.1.1 and the thin facings, $t_f = 0.00015$ (m), was selected for its low bimoment resistance. Four PZT patches were perfectly bonded on the whole surfaces of the beam, two patches on the top and other two on the bottom. Material properties of PZT patches were the same as the example in Section 5.3. (refer Table 5.11) The voltage of 100 V was applied to the PZT patches to induce bimoment in the different directions, as in the configurations explained in Section 3.4. (Positive and negative on the top two patches and negative and positive to the bottom ones.)

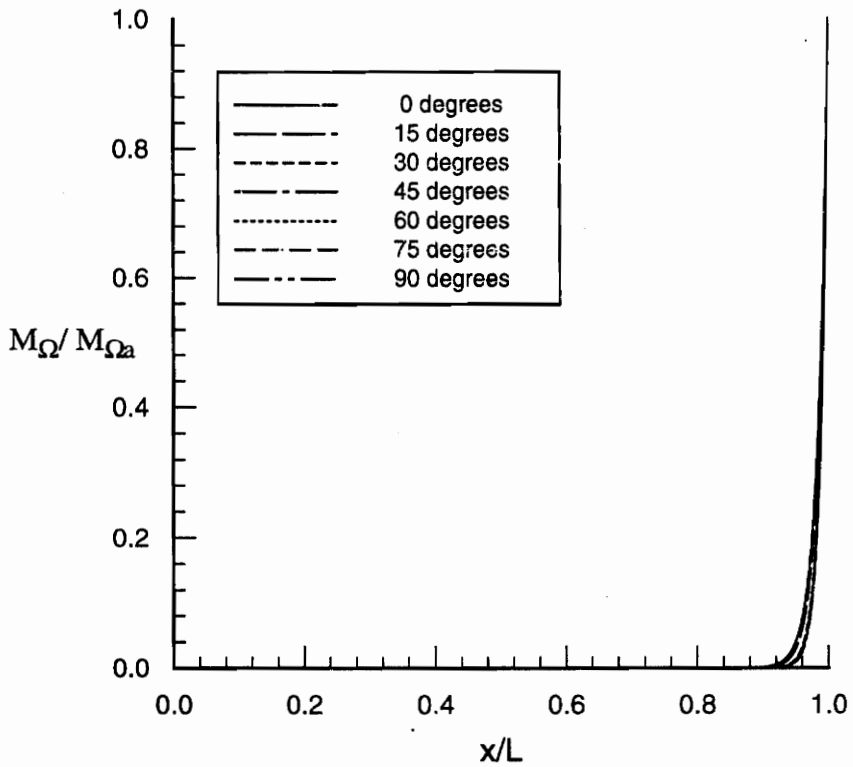

Fig. 5.24 Decay of bimoment.

The decay of bimoment for various fiber orientations over the nondimentionalized length of the beam is shown in Fig. 5.24. Here, x is the coordinate according to Fig. 5.22 and L is the length of the beam. M_Ω is the bimoment in the beam at the given location and $M_{\Omega a}$ is an applied/induced bimoment resulting at the tip of the beam. For all the fiber orientations, bimoment decays quickly around x/L=0.9. The close up of Fig. 5.24 for

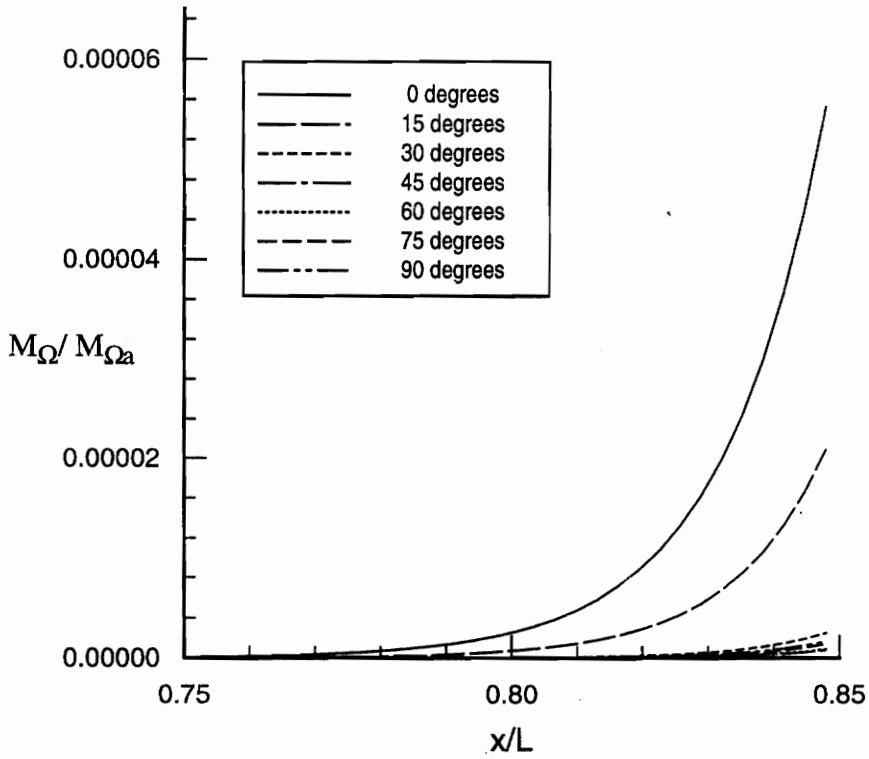

Fig. 5.25 Close up of Fig. 5.24.

0.75 =<x/L<=0.85 is shown in Fig. 5.25. From this figure, it can be said that the decay of bimoment is slower for the smaller angle of the fiber orientation. For the 30° to 90° fiber orientations, the difference is insignificant compared to 0° and 15° fiber angles.

5.5.3 *Effectiveness of control by bimoment*

Experimental results from Park et al.[32] were used for comparison to display the effectiveness of torsional control by bimoment. Park et al. conducted experiments to study the

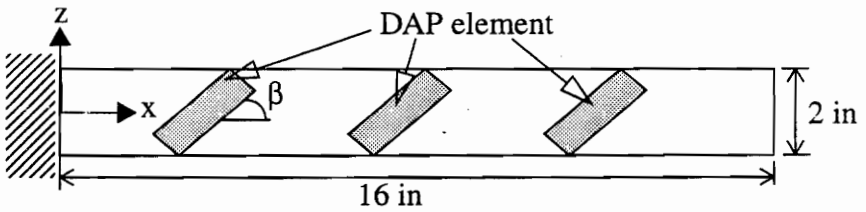

Fig. 5.26 A cantilever beam of Park et al.

effectiveness of torsional control by DAP (Directionally Attached Piezoelectric) elements. The cantilever aluminum beam with 3 DAP elements shown in Fig. 5.26 was used for the experiments. The angle of β was varied to study the effects of DAP elements. The thickness of the beam is 0.03125 in. The dimension of the DAP elements are shown inTable 5.19. 175 με of induced strains was applied to DAP elements to activate the beam.

Table 5.19 The dimension of DAP elements.

Length (in)	Width (in)	Thickness (in)
2.0	0.25	0.0075

Two configurations analyzed for the effectiveness of bimoment actuation are shown in Fig. 5.27. The beam has the same dimension as the Park et al. There are a total of four PZT actuators on the beam, two on the top as shown in Fig. 5.27, and the other two on the bottom and with exactly the same configuration as that of the top ones. The total area and

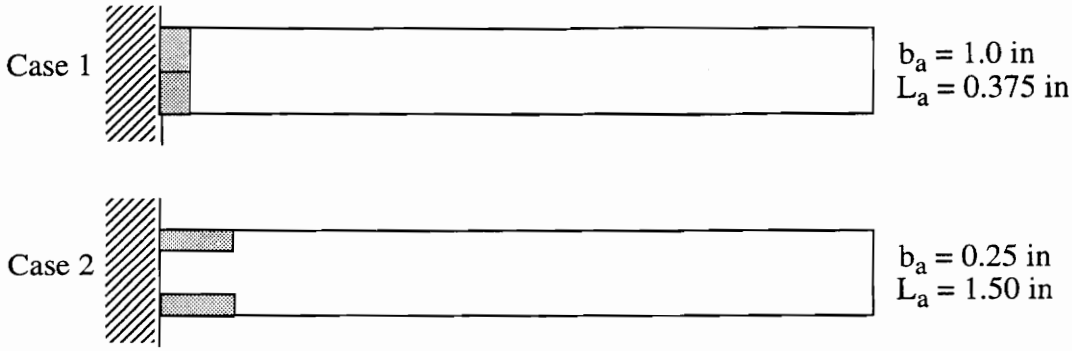

Fig. 5.27 The configurations of PZT patches for SANDB.

the thickness of the PZT are the same as the experiments' case. An induced strain of 175 $\mu\varepsilon$ was applied to these PZT patches to induce bimoment.

The comparison of angle of twists at the tip of the beam between the bimoment torsional control calculated by SANDB and the experimental results from DAP element torsional control is

Table 5.20 Comparison between bimoment control and DAP element control.

Case 1	Case 2	$\beta = 15°$	$\beta = 30°$	$\beta = 45°$
0.216°	0.168°	0.035°	0.055°	0.063°

shown in Table 5.20. Case 1 and 2 are calculated by SANDB and others were experimental data. Case 1 induced more twist than Case 2 in bimoment torsional controlling. In the experiments, $\beta = 45°$ induced the largest amount of angle of twist. It is clear that the bimoment is much more effective torsional control with the same amount induced strain. Case 2 induced a 2.7 times the largest induced twist in DAP elements.

6. Concluding remarks

6.1 Summary

The objective of this study was to develop a model to predict the static response of sandwich composite beams in extension, bending, and torsion subjected to piezoelectric induced forces from bonded PZT actuators. A finite element code is developed to determine the response of the beam subjected to induced strains from the PZT actuators.

The analytical model is developed from the displacement field suggested by Reddy.[15] Integrating virtual work with respect to the thickness coordinate, a plate theory was derived using Reddy's displacement field. Then a plate model with bonded PZT is formulated using a constitutive law. This plate model is reduced to one-dimensional beam model by assuming the plate displacements as explicit functions of the width coordinate. Including effects of shear-stretch, bend-twist, and warping, this beam model is capable of modeling torsional problems. The new model is capable of inducing a torsional effects without using a DAP element since a higher order moment, bimoment, is integrated in the model.

The finite element model is developed with one-dimensional, two noded elements with nine degrees of freedom at each node. Lagrangian and Hermitian interpolation functions are used. An element with PZT and one without PZT are constructed and assembled in various orders to model different configurations. In both analytical and numerical models, the PZT is assumed to be perfectly bonded to the substructure beam, thus treated as a part of the substructure. To implement this assumption in the finite element model, induced forces are treated as nodal forces at the edge of actuators following the findings of Crawley and De Luis[24]; i.e., the consistent load vector from the finite element method is not used. A complete code called "SANDB" was written to implement the finite element solution.

6.2 Discussions and conclusions

6.2.1 Numerical study

6.2.1.1 Verification without piezoelectric effects

To verify the analytical method, various numerical studies were done. As the first step, comparison with exact solutions were conducted on simple problems, an isotropic beam without PZT actuators under general loadings. Axial and transverse displacements were found to be in excellent agreement with exact solutions. Angle of twist under torsional loads was found to be accurate for beams with high the width to thickness ratio. This limitation was a result of the thin wall beam theory assumption taken in the course of development of the model.

Angle of twist resulting from the material coupling was verified with a two-dimensional model constructed using I-DEAS. A cantilever laminated beam, fibers oriented at 45° in each ply without PZT actuators, under a tip load was analyzed. Both transverse

deflection and angle of twist calculated by SANDB were verified to be in good agreement with results obtained with the finite element code I-DEAS. The one-dimensional model of SANDB did not show any discrepancy with the two-dimensional model of I-DEAS.

6.2.1.2 Effectiveness of using the higher-order theory for sandwich beam

A simply supported sandwich beam under a point load was analyzed by different methods. Predictions from SANDB were compared to NASTRAN, Sharma and Rao[9], and Holt and Webber.[10] A parameter study was done by varying the thickness and the stiffness of the core. For all cases, SANDB correlated very well with NASTRAN model and showed its flexibility to overcome the limitations other models had.

Ko's[20] cantilever beam of thin and stiff core under a distributed force was also studied. SANDB calculated transverse deflection that were quite comparable (2.02 % difference) to Ko's exact solution.

Finally, a sandwich beam with transversely flexible core studied by Frostig and Baruch[14] was analyzed for evaluation of the present program. Even though SANDB is not capable of modeling local effect under a point loading and including peeling stresses, prediction for the transverse displacement using SANDB was within 4.43 % of Frostig and Baruch resuslts.[14]

6.2.1.3 Verification with piezoelectric effects

An isotropic beam with PZT actuators were used to verify the piezoelectric modeling part of SANDB. A computer code DAISA[44] was used to calculate transverse deflections under induced bending for 2 cases. Predictions of SANDB were excellent, less than 0.5 % difference with DAISA's results.

To verify the prediction of axial displacement under extension and bending by PZT

actuators, models from Robbin and Reddy[28] were used as comparisons. The axial displacement predicted by SANDB was within 2.57 % of Robbin and Reddy"s results.[28] The transverse deflections from SANDB were slightly higher.

6.2.1.4 Convergence study

A simple isotropic cantilever beam with a pair of PZT actuators was used to perform a convergence study. Four different meshing schemes were compared for transverse deflection under bending activated by PZT, and also the angle of twist and its derivative under induced bimoment were compared. Different meshes did not have much effect on the convergence of the transverse deflection. Angle of twist and its derivative were more sensitive to the mesh size. PZT induced forces are a local phenomena thus refinement of mesh at the edge regions of actuators proved critical.

Effect of the distance between distributed PZT actuators on local interference was studied using the same beam as the one used for the convergence study under an induced bimoment. It was found that the distance between the actuators affects the local interference. Also, the important role of the actuators at the ends of the beam was observed.

6.2.1.5 Torsional problem

In this study, torsional control was accomplished with bimoments from PZT actuators. This can be done without having DAP elements. Different aspects of torsional problem were studied.

Bimoment resistance was calculated for different cross-sectional configurations. The sandwich construction has a reduced bimoment resistance and thus was found to be more suitable for twist control using an induced bimoment. The thinner the facings were, the lower the bimoment resistance. Using a higher fiber orientaion angle for advanced com-

posite facings results in lower resistance.

The decay length of the bimoment was calculated for a sandwich beam with different fiber angles in the face sheets, and it was observed that fiber angles close to the longitudinal direction of the beam results in a slower decay. For most fiber orientations, the effect of the bimoment was found to decay in a distance around 10 % of the beam length.

6.2.1.6 Bimoment torsional control

Experimental data from Park and Chopra[34] on torsional control by DAP elements were compared to the predictions from SANDB by bimoment torsional control. It was found that for this type of control the bimoment control is superior to the control prescribed by DAP elements. Bimoment induced much more angle of twist with the same induced strain and the same amount of PZT actuators. The improvement was 270 %.

6.2.2 Conclusions

From the different numerical analysis stated above, following conclusions were drown.

1. Use of the higher-order transverse shear deformation plate theory for modeling sandwich beam with or without PZT actuators can predict static response accurately with any configuration of the core thickness and core stiffness.
2. Refinement of mesh in the edge regions of actuators is crucial, especially for activated bimoment case.
3. The distance between distributed actuators has a significant effect on the local interference for bimoment actuations.
4. Bimoment resistance can be reduced by sandwich configuration, particularly by thin advanced fiber reinforced composite facings with 90° fiber orientation.

5. Decay of induced bimoment is slower for smaller angle of fiber orientations.
6. Bimoment torsional control is more effective than the torsional control by DAP elements.

6.3 Future work

The present model does not include shear lag effects of the adhesive layers between the beam and PZT patches. The perfect bonding assumption was taken and the modification was done to the finite element model, treating the induced forces as nodal forces, to over come this shortcoming. Modeling an adhesive layer between the bonded PZT patches and the substrate will result in a more realistic and accurate model.

For unsymmetrical sandwich beams, the effect of bending and extensional stiffness of the core can not be neglected. In present model, these core stiffnesses were included but analysis was done only on symmetric sandwich beams. Studying response of unsymmetrical sandwich beams will bring more credibility to the model developed.

The optimization on the location of actuators for various control will be a great interest. The effectiveness of bimoment torsional control could be improved by finding the optimum location of the actuators.

In this study, PZT patches were used as actuators. Including the electrical degree of freedom to the model will let the PZT to be used as sensors. This will result in a closed loop form of the control with feedback from the sensors. Since bimoment torsional control was more effective than the control by DAP elements, it can be said that with this model PZT can be better torsional sensor, being more sensitive to induced charge density from strains.

Finally, experimental verification will add credibility to this model and the possibility of bimoment torsional control, which has not been studied by others.

References

[1]Jones, R., M., *Mechanics of Composite Materials*, Scripta Book Company, Washigton, D.C., 1975.

[2]Schwartz, M., M., editor in chief, *Composite Materials Handbook*, McGraw-Hill, Inc., New York, 1992.

[3]Allen, H. G., *Analysis and Design of Structural Sandwich Panels*, Pergamon press, London, England, 1969.

[4]Peery, D., J., *Aircraft Structures*, McGraw-Hill Book Company, New York, 1950

[5]Johnson, A., F., and Sims, G., D., "*Mechanical Properties and Design of Sandwich Materials*," Composites, Vol. 17, No. 4, 1986, pp. 321-328.

[6]Cheng, S., "On the Theory of Bending of Sandwich Plates," *Proceedings of 4th U. S. National Congress on Applied mechanics*, 1962, pp. 511-518.

[7]Di Taranto, R. A., "Static Analysis of a Laminated Beam," *Journal of Engineering for Industry*, Vol. 95, 1973, pp. 755-761.

[8]Rao, D. K., "Static Response of Stiff-cored Unsymmetric Sandwich Beams," *Journal of Engineering for Industry*, 1976, Vol. 98, pp. 341-346.

[9]Sharma, S. R., and Rao, D. K., "Static Deflections and Stresses in Sandwich Beams under Various Boundary Conditions," *Journal of Mechanical Engineering Science*, Vol. 24, No. 1, 1982, pp.11-20.

[10]Holt, P. J., and Webber, J. P. H., " Exact Solution of Some Honeycomb Sandwich Beam, Plate and Shell Problems,' *Journal of Strain Analysis*, Vol. 17, No. 1, 1982, pp.1-8.

[11]Sanders, J., L., "An Improved First Approximation Theory for Thin Shells," NASA Report R-24, 1959.

[12]Koiter, W., T., "A Consistent First Approximation in the General Theory of Thin Elastic Shells," *Theory of Thin Elastic Shells* (First IUTAM Symposium), Edited by W. T. Koiter, 1960, North Holand.

[13]Webber, J., P., H., "Governing Equations for Thick Sandwich Shells with Honeycomb Cores and Laminated Faces," *Aero. Quart.*, Vol. 25, 1974, pp.271-286.

[14]Frostig, Y., and Baruch, M., "Bending of Sandwich Beams with Transversely Flexible Core," *AIAA Journal*, Vol. 28, No. 3, 1990, pp. 523-531.

[15]Reddy, J. N., "A Simple Higher-Order Theory for Laminated Composite Plates," *Journal of Applied Mechanics*, Vol. 51, 1984, pp. 745-752.

[16]Obst, A. W., and Kapania, R. K., "Nonlinear Static and Transient Analysis of Generally Laminated Beams," Virginia Polytechnic Institute and State University, CCMS-91-23, 1991.

[17]Lee, K. H., Xavier, P. B., and Chew, C. H., "Static Response of Unsymmetric Sandwich Beams Using an Improved Zig-Zag Model," *Composite Engineering*, Vol. 3, No. 3, 1993, pp. 235-248.

[18]Di Sciuva, M., "Bending, Vibration and Buckling of Simply Supported Thick Multilayered Orthotropic Plates: An Evaluation of New Displacement Model," *Journal of Sound and Vibration*, Vol. 105, 1986, pp.425-442.

[19]Kant, T., Varaiya, J., H., and Arora, C. P., "*Finite Element Transient Analysis of Composite and Sandwich Plates Based on a Refined Theory and Implicit Time Integration Schemes*," Computers & Structures, Vol. 36, No. 3, 1990, pp. 401-420.

[20]Ko, C. L., "Flexural Behavior of a Rotating Sandwich Tapered Beam," *AIAA Journal*, Vol. 27, No. 3, 1989, pp.359-369.

[21]Ha, K. H., "Finite Element Analysis of Sandwich Plates: An Overview," *Computers & Structures*, Vol. 37, No. 4, 1990, pp. 397-403.

[22]Ikeda, T., *Fundamentals of Piezoelectricity*, Oxford University Press, New York, 1990.

[23]Piezo Kinetics Incorporated, Application Notes-Piezoceramics.

[24]Crawley, E., F., and De Luis, J., "Use of Piezoelectric Actuators as Elements of Intelligent Structures," *AIAA Journal*, Vol.25, No. 10,1987, pp.1373-1385.

[25]Im, S., and Atluri, S., N., "Effects of a Piezo-Actuator on a Finitely Deformed Beam Subjected to General Loading," *AIAA Journal*, Vol. 27, 1989, pp.1801-1807.

[26]Crawley, E. F. , and Lazarus, K. B., "Induced Strain Actuation of Isotropic and Anisotropic Plates,", *AIAA Journal*, Vol. 29, No. 6, 1991, pp. 944-951.

[27]Wang, B., and Rogers, C., A., "Modeling of Finite-Length Spatially-Distributed Induced Strain Actuators for Laminated Beams and Plates," *Proceedings of the AIAA/ ASME/ASCE/AHS/ASC 32nd Structures, Structural Dynamics, and Material Conference* (Baltimore, MD), AIAA, Wasington, DC, 1991, (AIAA Papaer 91-1258-CP).

[28]Robbins, D. H., and Reddy, J. N., "Analysis of Piezoelectrically Actuated Beams Using a Layer-wise Displacement Theory," *Computers and Structures*, Vol. 41, No.2, 1991, pp. 265-279.

[29]Ha, S. K., Keilers, C., and Chang, F. K., "Finite Element Analysis of Composite Structures Containing Distributed Piezoelectric Sensors and Actuators," *AIAA Journal*, Vol. 30, No. 3, 1992, pp.772-780.

[30].Hwang, W., and Park, H., C., " Finite Element Modeling of Piezoelectric Sensors and Actuators," *AIAA Journal*, Vol.31, No. 5, 1993, pp.930-937.

[31]Suleman, A., and Venkayya, V., B., "Flutter Control of an Adaptive Composite Panel," *Proceedings of the AIAA/ASME/ASCE/AHS/ASC 35th Structures, Structural Dynamics, and Material Conference* (Hilton Head, NC), AIAA, Wasington, DC, 1994, (AIAA Papaer 94-1744-CP).

[32]Park, C., Walz, C., and Chopra, I., "Bending and Torsion Models of Beams with Induced Strain Actuators," *Proceedings of SPIE Smart Structures and Materials '93* (Albuquerque, NM), The International Society for Optical Engineering, Bellingham, WA, 1993, pp.192-216.

[33]Chen, C., P., and Chopra, I., "A Feasibility Study to Build a Smart Rotor: Induced-Strain Actuation of Airfoil Twisting Using Piezoceramics," *Proceedings of SPIE Smart Structures and Materials '93* (Albuquerque, NM), The International Society for Optical Engineering, Bellingham, WA, 1993, pp.225-229.

[34]Park, C., and Chopra, I., "Modeling Piezoceramic Actuation of Beams in Torsion," *Proceedings of the AIAA/ASME/ASCE/AHS/ASC 35th Structures, Structural Dynamics, and Material Conference* (Hilton Head, NC), AIAA, Wasington, DC, 1994, (AIAA Paper 94-1781-CP).

[35]Barrett, Ron, "Active Plate and Missile Wing Development using Directionally Attached Piezoelectric Elements," *AIAA Journal*, Vol. 32, No.3, 1994, pp.601-609.

[36]Kawiecki, G., and Smith, W., P., "Piezoelectric Actuator Capable of Inducing Torsional and Bending control Loads with No Structural Coupling," *Proceedings of the AIAA/ ASME/ASCE/AHS/ASC 35th Structures, Structural Dynamics, and Material Conference* (Hilton Head, NC), AIAA, Wasington, DC, 1994, (AIAA Papaer 94-1781-CP).

[37]Shieh, R., C., "Governing Equations and Finite Element Models for Multiaxial Piezoelectric Beam Sensors/Actuators," *AIAA Journal*, Vol.32, No. 6, 1994, pp.1250-1258.

[38]Senthilnathan, N., R., Lim, S., P., Lee, K., H., and Chow, S., T., " Buckling of Shear-Deformable Plates," *AIAA Journal*, Vol.25, No. 9, 1987, pp.1268-1271.

[39]Chaudhry, Z., "*Constitutive Relations Specialized to Piezoceramics*," presented as Lecture Notes in ME:5984 Smart Material Systems, 1994

[40]Dosch, J., J., Inman, D., J., and Garcia, E., "A Self-Sensing Piezoelectric Actuator for Collocated Control," *Journal of Intelligent Materials, Systems, and Structures*, Vol.3, 1992, pp. 166-185.

[41]Rose, L., R., F., "Theoretical Analysis of Crack Patching," *Bonded Repair of Aircraft Structures*, Edited by A. A. Baker, Martinus Nijhoff Publishers, 1988.

[42]Reddy, J., N., *An Introduction to Finite Element Method*, McGraw-Hill, New York, 1984.

[43]The MacNeal-Schwendler Corporation, *MSA/NASTRAN User Manual*, The MacNeal-Shwendler Corporation, Los Angels, 1991.

[44]Center for Intelligent Material Systems and Structurtes, *Dynamic Analysis of Induced Strain Actuators: Program User's Guide*, Center for Intelligent Material Systems and Structures, 1993.

[45]Liang, C., Sun, F., P., and Rogers, C., A., "An Impedance Method for the Dynamic Analtsis of Active Material Systems," *Proceedings of the AIAA/ASME/ASCE/AHS/ASC 34th Structures, Structural Dynamics, and Material Conference* (La Jolla, CA), AIAA, Wasington, DC, 1993, (AIAA Papaer 93-1713-CP).

[46]Liang, C., Sun, F., P., and Rogers, C., A., "Coupled Electric-Mechanical Analysis of Piezoelectric Ceramic Actuator Drive Systems - Determination of the Actuator Power Consumption," *Proceedings of SPIE Smart Structures and Materials '93* (Albuquerque, NM), The International Society for Optical Engineering, Bellingham, WA, 1993.

[47]Gjelsvik, A., *The Theory of Thin Walled Bar*s, John Wiley & Sons, New York, 1981.

Vitas

Ayako Koike was born on April 11, 1968 in Tokyo. While her brief childhood life in Beirut, Lebanon, she had a chance to visit many countries in Europe and exposed to different cultures in early age. After successively survived through so called "the entrance exam hell" of Japanese education, her wish to broaden the mind in different society brought her to the United States in August 1986. She spent a year in a high school in St. Louis, Missouri as an exchange student and graduated from it in May 1987. After the completion of her high school in Japan in March 1988, she came back to the United States. She started her study at University of Missouri-Rolla in August, 1988 and received a Bachelor of Science in Aerospace Engineering in May 1992. Her desire to go to eastward from St. Louis brought her to Virginia Tech in August 1992 for further education. Ayako will receive her Master of Science in Aerospace and Ocean Engineering in December 1994. She is going to start working for Ford Motor Company in January 1995.

Ayako Koike